Electrochemical Shock: Mechanical Degradation of Ion-Intercalation Materials

by

William Henry Woodford IV

B.S., Materials Science and Engineering
The Pennsylvania State University, 2008

Submitted to the Department of Materials Science and Engineering
in partial fulfillment of the requirements for the degree of

Doctor of Philosophy in Materials Science and Engineering

at the

MASSACHUSETTS INSTITUTE OF TECHNOLOGY

June 2013

Author .....
Department of Materials Science and Engineering
May 17, 2013

Certified by .....
Yet-Ming Chiang
Kyocera Professor of Ceramics
Thesis Supervisor

Certified by .....
W. Craig Carter
Professor of Materials Science and Engineering
Thesis Supervisor

Accepted by .....
Gerbrand Ceder
R.P. Simmons Professor of Materials Science and Engineering
Chair, Departmental Committee on Graduate Students

Electrochemical Shock: Mechanical Degradation of Ion-Intercalation Materials

by

William Henry Woodford IV

Submitted to the Department of Materials Science and Engineering
on May 17, 2013, in partial fulfillment of the
requirements for the degree of
Doctor of Philosophy in Materials Science and Engineering

Abstract

The ion-intercalation materials used in high-energy batteries such as lithium-ion undergo large composition changes–which correlate to high storage capacity—but which also induce structural changes and stresses that can cause performance metrics such as power, achievable storage capacity, and life to degrade. "Electrochemical shock"–the electrochemical cycling-induced fracture of materials–contributes to impedance growth and performance degradation in ion-intercalation batteries. Using a combination of micromechanical models and *in operando* acoustic emission experiments, the mechanisms of electrochemical shock are identified, classified, and modeled in targeted model systems with different composition and microstructure. Three distinct mechanisms of electrochemical shock in ion-intercalation materials are identified: 1) concentration-gradient stresses which arise during fast cycling, 2) two-phase coherency stresses which arise during first-order phase-transformations, and 3) intergranular compatibility stresses in anisotropic polycrystalline materials. While concentration-gradient stresses develop in proportion to the electrochemical cycling rate, two-phase coherency stresses and intergranular compatibility stresses develop independent of the electrochemical cycling rate and persist to arbitrarily low rates. For each mechanism, a micromechanical model with a fracture mechanics failure criterion is developed.

This fundamental understanding of electrochemical shock leads naturally to microstructure design criteria and materials selection criteria for ion-intercalation materials with improved life and energy storage efficiency. In a given material system, crystal symmetry and phase-behavior determine the active mechanisms. Layered materials, as exemplified by $LiCoO_2$, are dominated by intergranular compatibility stresses when prepared in polycrystalline form, and two-phase coherency when prepared as single crystal powders. Spinel materials such as $LiMn_2O_4$, and $LiMn_{1.5}Ni_{0.5}O_4$ undergo first-order cubic-to-cubic phase-transformations, and are subject to two-phase coherency stresses even during low-rate electrochemical cycling. This low-rate electrochemical shock is averted in iron-doped material, $LiMn_{1.5}Ni_{0.42}Fe_{0.08}O_4$, which has continuous solid solubility and is therefore not subject to two-phase coherency stresses; this enables a wider range of particle sizes and duty cycles to

be used without electrochemical shock. While lithium-storage materials are used as model systems, the physical phenomena are common to other ion-intercalation systems, including sodium-, magnesium-, and aluminum-storage compounds.

Thesis Supervisor: Yet-Ming Chiang
Title: Kyocera Professor of Ceramics

Thesis Supervisor: W. Craig Carter
Title: Professor of Materials Science and Engineering

Acknowledgements

I am foremost thankful to my co-advisers, Professor Yet-Ming Chiang and Professor Craig Carter. I am especially grateful for the fine balance they individually and collectively struck between providing mentorship and support while allowing me a tremendous degree of independence in my thesis research.

Thanks to my thesis committee, Professor Krystyn Van Vliet and Professor Michael Demkowicz for their valuable questions and comments on the thesis. Many thanks are owed to Krystyn for her direct and thoughtful advice on all aspects of life as a young scientist.

My time in the Chiang and Carter research groups has been interesting and I've benefitted from interactions with many colleagues, including Bryan Ho, Can Erdonmez, Wei Lai, Chang-Jun Bae, Yan Wang, Pimpa Limthongkul, Nir Baram, Yajie Dong, Rae Zucker, Dan Cogswell, Victor Brunini, Li Sun, Li Zheng, Red Ransil, Kai Xiang, Ruhul Amin, Dorthe Ravnsbaeck, and Wenting Xing. I also wish to thank Priya Moni and Lisa Blancha for help in the summer of 2012. Toni Centorino, Pat Kearney, and Jennifer Patten have provided all manner of assistance and support throughout my time in the Chiang and Carter groups.

I have benefited immeasurably during graduate school from an abundance of talented and kind friends; in your friendship I have an embarrassment of riches. I am especially thankful to Jean Yang who has been a fantastic roommate for the last four years; she has been the cornerstone of my support network through good times and bad. I found my social wheelhouse immediately at MIT with awesom-o; there are simply too many of you to list here, but thanks go to each of you for countless great memories. Special thanks go to Rahul Malik, David Bradwell, Sal Barriga, and Reece Daniel, who have always been happy to discuss batteries over beer and pizza. I am forever indebted to Matthew Smith and Rahul, who brought me food and friendship after the most terrifying night of my life; you picked me up when I needed it most. Margo Monroe provided constant encouragement as much of the work in this thesis was completed, as did the rest of the crew at the HMS Putnam.

Many thanks are owed to the E-Crew; even though we have mostly lived in different places since graduation from Penn State, I am still so proud to have you as friends. Thanks to Stefan Yohe and Sam Weaver, Alejandro Levander and Nicole Adelstein, Joe Swearman, and Andy and Kristin Watson, for your fierce and diligent friendship, from wherever you call home.

Many thanks go to Angelita Mireles and Elissa Haverty who provided help and advice

throughout my graduate school adventures; we are all so lucky to have you here in DMSE. Thanks also to everyone on the GMC throughout my tenure at MIT; the graduate student community in this department is special thanks to your efforts.

I am grateful for the financial supporters of this thesis, including the U.S. Department of Energy, Basic Energy Sciences, under Award number DE-SC0002633, the National Science Foundation Graduate Research Fellowship, and a MIT-Bosch MIT Energy Initiative Graduate Fellowship.

Last, but certainly not least, I am thankful to my family for all of their support and encouragement. My parents, Debbie and Bill impressed on me the value of education and endured my curiosity from a young age. I couldn't ask for a better sibling than my sister, Mandy, who I am proud to have as a friend as well as a sister. Most importantly, my whole family has provided unconditional love and support throughout my life.

Thank you all.

Contents

List of Figures

List of Tables

Chapter 1

Introduction

Batteries are electrochemical energy storage devices which have enabled—or are enabling—a wide range of technologies, including portable electronics, electrified vehicles, and large-scale grid integration of renewable energy sources such as wind and solar. In general, electrochemical energy storage devices are attractive because chemical bonds have high energy density and electrochemical devices allow energy to be stored and retrieved as electricity.

Today, lithium-ion batteries are attractive for many applications due to their high specific energy, energy density, specific power, and power density. Lithium-ion batteries, have enabled the proliferation of portable electonics, including laptop computers and cellular telephones and are today enabling the elecrification of automobiles. Today, alternative chemistries, based around the same ion-intercalation reactions are emergining as potential alternatives; chemistries of interest include sodium, magnesium, and aluminum. Potential advantages of these alternative chemistries include cost, abundance, safety, and greater energy density.

In all of these ion-intercalation materials, large composition changes are essential to high storage capacity. However, these composition changes are often accompanied by large shape changes, with most transition metal oxide materials exhibiting stress-free strains on the order

of a few percent. If constrained, these shape changes can induce large stresses, sufficient to drive fracture of the ion-intercalation material, degrading performance metrics such as power, efficiency, and life.

We call this electrochemical-cycling-induced fracture “electrochemical shock," by analogy to thermal shock of brittle materials [1]. The central objective of this thesis is to develop microstructure design criteria and materials selection criteria to mitigate electrochemical shock in ion-intercalation materials. To derive these design and selection criteria, the fundamental mechanisms of electrochemical shock are identified and classified using experiments and continuum models with selected model systems. The particular model systems used in this thesis are all lithium-storage compounds, but the mechanisms of electrochemical shock are general and will apply to all ion-intercalation materials.

The remainder of this chapter is organized as follows. First, the operating principles of ion-intercalation batteries are summarized. The observed compositional (Vegard) strains in ion-intercalation materials are reviewed in relation to phase-behavior and crystal symmetry. Anticipating the direction of the thesis, the three distinct mechanisms of electrochemical shock are summarized and related to qualitative differences among the compositional strains in different ion-intercalation materials. Previous work in the area of electro-chemo-mechanics of ion-intercalation materials is summarized, with an emphasis on the state of the literature at the outset of the thesis.

1.1 Operating Principles of Ion-Intercalation Batteries

Ion-intercalation batteries, such as lithium-ion batteries, operate by shuttling ions between two intercalation compounds with dissimilar chemical potentials. In intercalation reactions, the underlying host structure is largely unchanged, with no reconstructive phase transformations. For example in Li_XCoO_2, lithium atoms are inserted and removed (intercalated

and de-intercalated) from distinct crystallographic sites, while the CoO_2 framework remains intact, at least for the reversible cycling window of $0.5 \leq X \leq 1$.

A prototypical lithium-ion cell uses a transition metal oxide such as $LiCoO_2$ as a positive electrode material and a graphite negative electrode. As illustrated in Figure 1-1, the positive and negative electrodes (conventionally referred to as cathode and anode, though such usage is conventional, rather than formally correct. The positive electrode is the cathode during discharge, but is formally the anode during charge. Similarly, the negative electrode is an anode during discharge, but is the cathode during charge.) are composite mixtures of active material—which stores the intercalating ions—conductive additives such as carbon black, and a polymeric binder. As the battery is charged, lithium ions and electrons are removed from the positive electrode material and separated; the conventional half-reaction for this process is given in Equation 1.1. As shown in Figure 1-1, the overall reaction proceeds electrochemically because the lithium ions and electrons are separated; lithium ions travel through an electrolyte which is an ionic conductor and electronic insulator while the electrons travel through the external circuit. At the negative electrode, lithium ions and electrons meet and are intercalated into the graphitic material, as described by Equation 1.2. During discharge, the process is reversed.

$$LiCoO_2 \leftrightharpoons Li_{1-x}CoO_2 + xLi^+ + xe^- \tag{1.1}$$

$$C_6 + xLi^+ + xe^- \leftrightharpoons Li_xC_6 \tag{1.2}$$

Three classes of lithium-storage compounds are used today in commercial lithium-ion batteries: 1) layered lithium-containing materials, such as $LiCoO_2$ which adopt the α-$NaFeO_2$ ordered rocksalt structure, 2) spinel oxides, such as $LiMn_2O_4$, and 3) olivines such as $LiFePO_4$. The layered compounds typically adopt rhombohedral or monoclic space groups; the spinels are typically cubic, but at high lithium concentrations can transform to tetragonally distorted structures; the olivines adopt an orthorhombic space group.

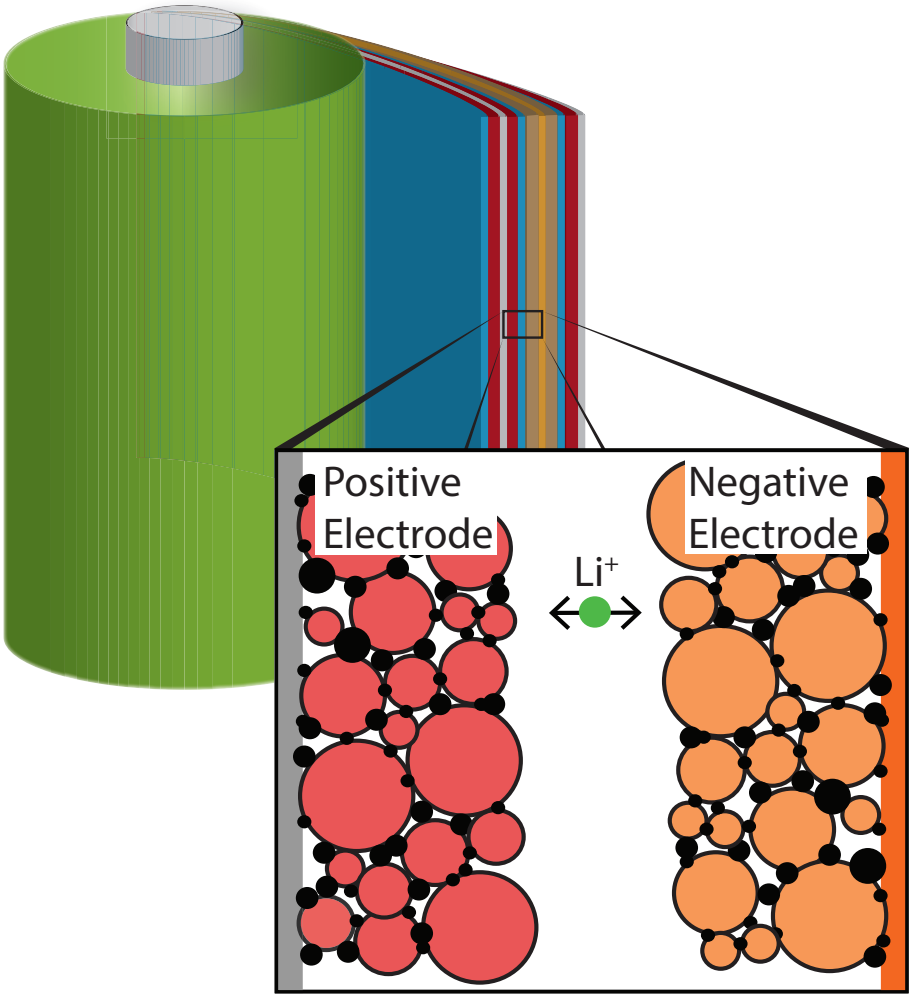

Figure 1-1: Schematic of a lithium-ion cell sandwich

1.2 Compositional (Vegard) Strains in Ion-Intercalation Materials

The ion-intercalation materials used in lithium-ion batteries, and in other kinds of ion-intercalation batteries, undergo large composition changes, which enable high storage capacity. These composition changes are often accompanied by large shape changes, with most transition metal oxide materials exhibiting stress-free strains on the order of a few percent.

As a result, electrical, chemical, and mechanical driving forces are all coupled in these electrochemical energy storage devices. Figure 1-2 illustrates the connections—thermodynamic and constitutive relationships—among electrical, chemical, and mechanical variables. Some of the relationships are familar, such as the Nernst Equation and Hooke's Law. Others are less explored, such as the coupling between electrical potential and stress in a non-piezoelectric, electrochemical system (though this effect has been measured in lithiated silicon $\mathrm{Li}_X\mathrm{Si}$ [2]). The Vegard coefficients, which relate compositional and dimensional changes in materials are of central importance to this thesis; these are defined by the relationship between the stress-free strain accompanying a compositional change and the extent of that composition change:

$$\epsilon_{ij} = \Omega_{ij}\Delta c \tag{1.3}$$

The Vegard coefficients are a proper second-rank tensor and obey all of the symmetry requirements and transformation laws so implied. For cubic materials, the Vegard coefficients are isotropic, while for lower symmetry materials, there are a larger number of independent coefficients, up to six for the most general triclinic crystal systems. In the metallurgy literature, the Vegard coefficients have also been called the solute distortion tensor [3].

The details of the compositional strains depend on both the crystal symmetry and phase-behavior of a given ion-intercalation compound. The lithium-storage compounds of commercial and research interest display a wide variety composition-dependent Vegard strains,

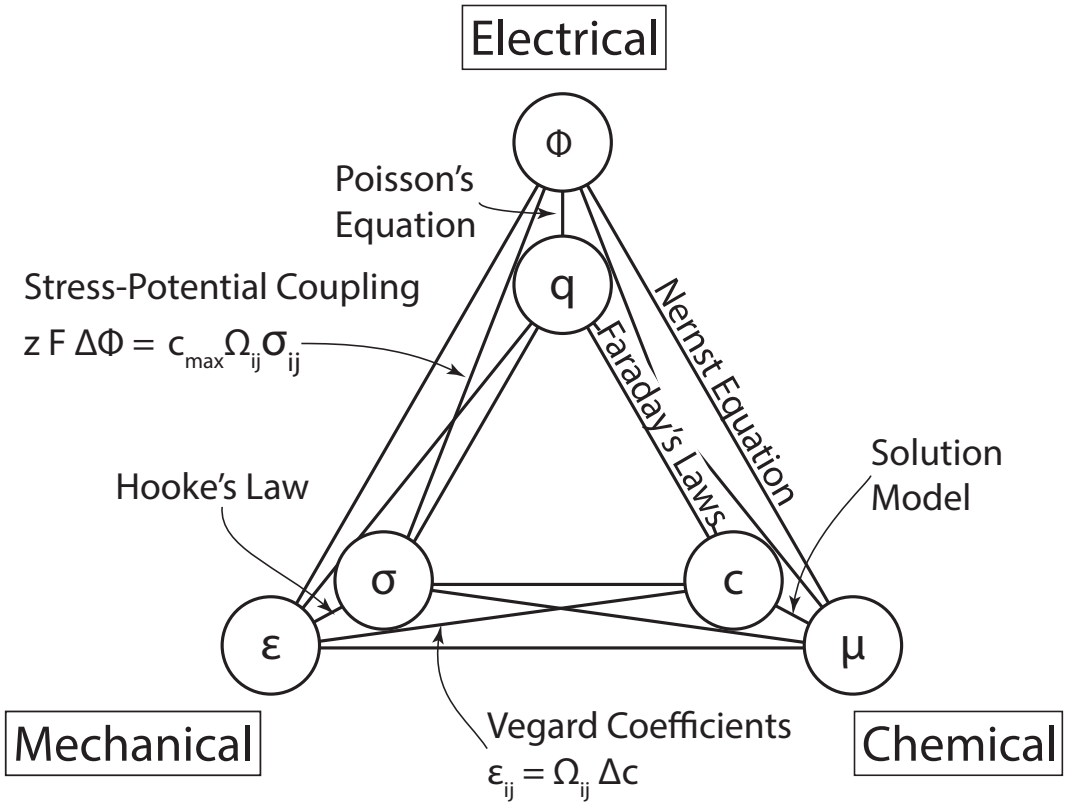

Figure 1-2: Heckmann-type diagram for electro-chemo-mechanics showing the thermodynamic connections.

which are readily characterized through the composition-dependent lattice parameters, as determined by x-ray diffraction.

Four different examples of composition-dependent lattice parameters observed in Li-storage compounds are shown in Figure 1-3. The most straightforward system is the cubic spinel polymorph of Li_XTiS_2, shown in panel (A), which has continuous solid-solubility of lithium and a linear variation of lattice parameter with changing composition [4]. This simple behavior is unusual, as the cubic spinel polymorph of Li_XTiS_2 is the only known example of this behavior. The opposite extreme is exemplified by Li_XFePO_4, shown in panel (B), which has negligible solid-solubility and an anisotropic transformation strain [5]. In this material, changes in lithium composition are accomodated almost entirely by a first-order phase transformation between $Li_\alpha FePO_4$ and $Li_{1-\beta}FePO_4$ with $\alpha, \beta \approx 0$. Both end-members are orthorhombic materials, so the anisotropic transformation strain has three independent components.

Intermediate cases are more common, such as are encountered in spinel $Li_XMn_2O_4$, shown in panel (C), and layered Li_XCoO_2, shown in panel (D). For electrochemical cycling in the composition region $0 \leq X \leq 1$, (where the electrode voltage is $\sim$ 4 V vs. Li^+/Li), $Li_XMn_2O_4$ is cubic throughout, but there is complex-phase behavior, with two regions of solid solubility for $0.5 \leq X \leq 1$ and $0.2 \leq X \leq 0.25$ separated by a first-order phase transformation for compositions $0.25 \leq X \leq 0.5$ [6]. The two coexisting cubic phases have lattice parameters which differ by $\sim$1.2%. At higher lithium-contents ($1 \leq X \leq 2$) this material undergoes a first-order phase transformation to a tetragonally distorted spinel with composition $Li_2Mn_2O_4$. In Li_XCoO_2, there is also complex phase-behavior with regions of solid-solubility separated by a miscibility gap. In this layered compound, the shape change is anisotropic, and the partial molar volume of lithium is negative [7].

Table 1.1 summarizes the experimentally measured, anisotropic, net stress-free strains for many Li-storage compounds. The initial and final compositions are specified, and the

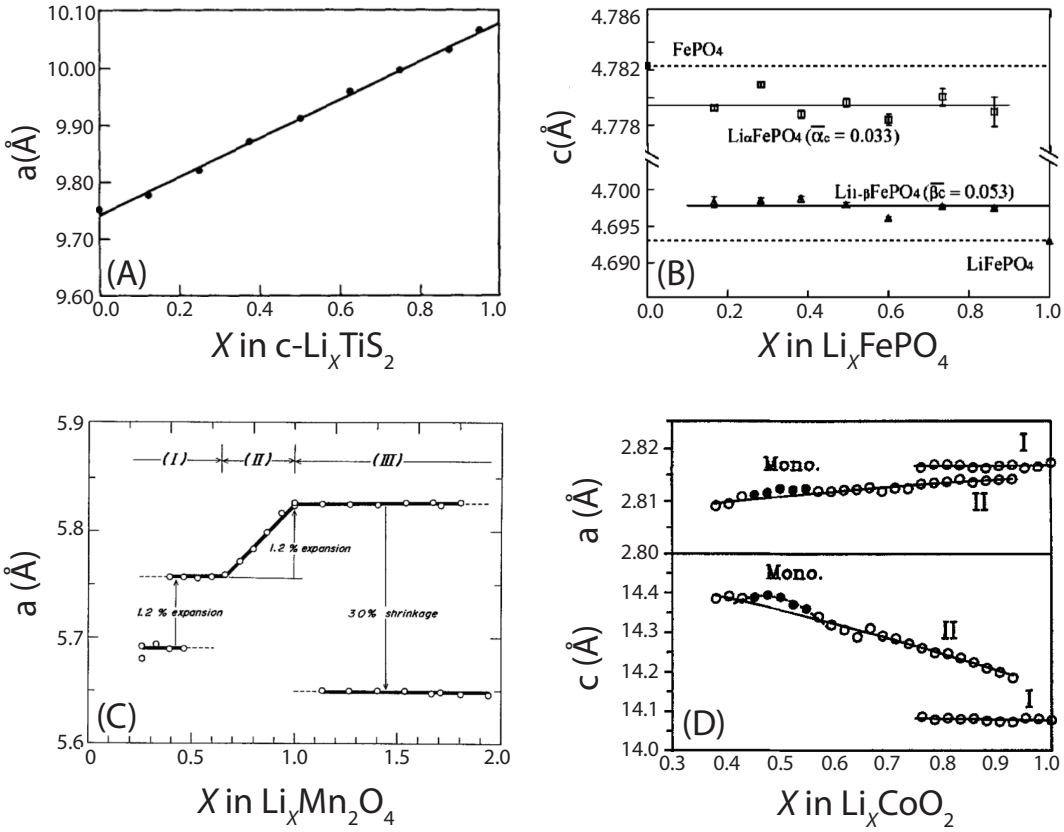

Figure 1-3: Examples of the different possible variations in lattice parameters of Li-storage compounds. Exaples shown are (A) cubic Li_XTiS_2 [4], (B) Li_XFePO_4 [5], (C) $Li_XMn_2O_4$ [6], and (D) Li_XCoO_2 [7].

tabulated strains are reported for the full composition change, irrespective of phase-behavior. For low symmetry materials with more than three independent Vegard coefficients, the second rank tensor has been diagonalized to principal axes and the principal Vegard strains are listed in descending order. The volumetric strain, and average electrode potential relative to a Li^+/Li reference is also given. Table 1.2 collects analogous data for a number of Na-storage compounds.

1.3 Electrochemical Shock

The compositional stress-free strains observed in these ion-intercalation materials exceed the failure strains of most brittle materials. As a result, there have been numerous observations of mechanical deformation and battery peformance degradation associated with these shape changes. Figure 1-4 shows examples of observed mechanical damage in Li-storage particles of varying composition and microstructure, including an individual $LiCoO_2$ crystallite [27], a coarse individual $LiFePO_4$ [28] crystallite, and a polycrystalline $LiNi_{0.8}Co_{0.15}Al_{0.05}O_2$ particle [29]. Similar particle-level fracture has been observed in post-mortem electron microscopy studies of intercalation materials [30, 31, 32], and has been observed through acoustic emission during cycling of primary Li/MnO_2 batteries [33, 34].

We have termed this electrochemical-cycling-induced fracture “electrochemical shock," by analogy to thermal shock of brittle materials [1]. Thermal shock refers to fracture due to thermo-elastic stresses caused by rapid heating or cooling, and this problem has been treated successfully by fracture mechanics analysis [35, 36, 37, 38, 39]. The analogy between thermal and electrochemical shock as driving forces for fracture can be quantified by a simple scaling argument. An equivalent thermal shock temperature drop (ΔT) for a given lithium storage compound is defined by equating the relative volume expansion (the *stress-free strain*) caused by a maximal change in lithium concentration to a linear thermal strain.

Table 1.1: Net compositional stress-free strains of selected lithium-storage compounds.

Lithium storage compound	Limiting composition	Crystal system	a strain $\Delta a/a_0$ [%]	b strain $\Delta b/b_0$ [%]	c strain $\Delta c/c_0$ [%]	Volume strain $\Delta V/V_0$ [%]	Potential vs. Li/Li^+ [V]	Ref.
Li-extraction								
$LiCoO_2$	$Li_{0.5}CoO_2$	Rhomb.	-0.35		+2.6	+1.9	3.9	[7]
$LiNi_{0.8}Co_{0.2}O_2$	$Li_{0.5}Ni_{0.8}Co_{0.2}O_2$	Rhomb.	-1.78		+1.52	-2.04	3.6	[8]
$LiNi_{0.8}Co_{0.15}Al_{0.05}O_2$	$Li_{0.5}Ni_{0.8}Co_{0.15}Al_{0.05}O_2$	Rhomb.	-1.64		+2.12	-1.16	3.7	[9]
$LiNiO_2$	$Li_{0.3}NiO_2$	Rhomb.	-2.1		+1.4	-2.8	3.8	[10]
$LiNi_{1/3}Mn_{1/3}Co_{1/3}O_2$	$Li_{0.47}Ni_{1/3}Mn_{1/3}Co_{1/3}O_2$	Rhomb.	-0.51		+3.46	+2.44	3.7	[11]
$LiFePO_4$	$FePO_4$	Ortho.	-4.9	-3.6	+1.9	-6.6	3.4	[12]
$LiMnPO_4$	$MnPO_4$	Ortho.	-8.16	-3.16	+0.48	-10.83	4.1	[13]
$LiMn_2O_4$	Mn_2O_4	Cubic	-2.5			-7.3	4.0	[14]
$LiNi_{0.5}Mn_{1.5}O_4$	$Ni_{0.5}Mn_{1.5}O_4$	Cubic	-2.1			-6.2	4.7	[15]
$LiFeSO_4F$	$FeSO_4F$	Triclinic	-15.88	+9.53	-4.04	-10.1	3.6	[16]
Li_2VPO_4F	$LiVPO_4F$	Triclinic	-14.39	+9.49	-2.18	-6.92	1.8	[17]
Li_2VPO_4F	VPO_4F	Triclinic	-16.53	+6.95	-5.87	-14.68	3.1	[17]
Li-insertion								
C_6 (graphite)	LiC_6	Hex.	+1.2		+10.4	+12.8	0.1	[18]
$Li_4Ti_5O_{12}$	$Li_7Ti_5O_{12}$	Cubic	0.0			0.0	1.5	[19]
$LiMn_2O_4$	$Li_2Mn_2O_4$	Tetrag.	-3.0		+12.3	+6.3	3.0	[6]
Si	$Li_{4.4}Si$	Amorph.	+103			+310	0.3	[20]
$\beta-$Sn	$Li_{4.4}Sn$	Amorph.	+87			+260	0.4	[20]

Note: Rhombohedral structures are indexed in the hexagonal settings.
Strains in monoclinic and triclinic structures have been diagonalized to principal axes.

Table 1.2: Net compositional stress-free strains of selected sodium-storage compounds.

Sodium storage compound	Limiting composition	Crystal system	a strain $\Delta a/a_0$ [%]	b strain $\Delta b/b_0$ [%]	c strain $\Delta c/c_0$ [%]	Volume strain $\Delta V/V_0$ [%]	Ref.
Na-extraction							
$NaFePO_4$	$FePO_4$	Ortho.	-0.80	-3.31	-5.21	-9.31	[21]
$NaMnPO_4$	$MnPO_4$	Ortho.	-8.69	-6.56	-4.48	-19.73	[21]
$Na_{0.6}MnO_2$	$Na_{0.2}MnO_2$	Ortho.	-1.30	-4.23	-0.99	-6.52	[22]
$NaFeSO_4F$	$FeSO_4F$	Triclinic	-18.66	16.41	-10.65	-14.3	[16]
Na_2FePO_4F	$NaFePO_4F$	Ortho.	-2.59	1.90	-3.56	-4.24	[23]
$NaCoO_2$	$Na_{0.5}CoO_2$	Hex.	-2.35		6.07	1.37	[24]
$Na_{1.0}Li_{0.2}Ni_{0.25}Mn_{0.75}O_\delta$	$Na_xLi_{0.2}Ni_{0.25}Mn_{0.75}O_\delta$	Rhomb.	-0.97		1.88	-0.06	[25]
$NaVO_2$	$Na_{0.5}VO_2$	Mono.	22.89	-20.84	-5.03	-3.34	[26]

Notes: Rhombohedral structures are indexed in the hexagonal settings.
Strains in monoclinic and triclinic structures have been diagonalized to principal strains.

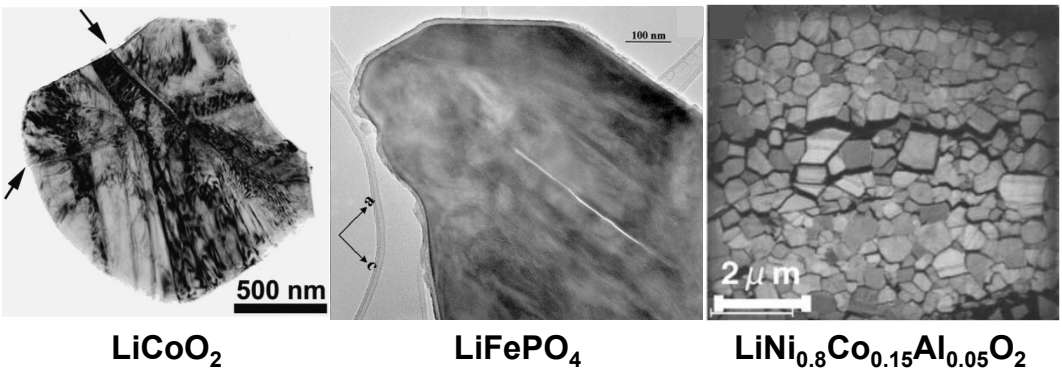

Figure 1-4: Examples of fractured lithium-storage particles with different compositions, crystal structures, and microstructures. Shown are an individual $LiCoO_2$ crystallite [27], a coarse individual $LiFePO_4$ crystallite [28], and a polycrystalline $LiNi_{0.8}Co_{0.15}Al_{0.05}O_2$ particle [29].

For the present analysis, which addresses mostly metal oxide compounds, a linear coefficient of thermal expansion $\alpha = 10^{-5}$ K^{-1} is assumed as representative of many metal oxides. The resulting equivalent thermal shock temperature drops for the Li- and Na- storage compounds summarized in Tables 1.1 & 1.2 are commonly 1000-2000 K; electrochemical shock is often a severe service condition.

There is mounting evidence that electrochemical shock contributes to impedance growth in lithium-ion batteries. [40, 9, 41, 29, 42, 43, 32, 44]. For lithium-ion batteries to succeed in long-life energy storage applications, it is essential to understand and control all sources of impedance growth and capacity fade. Models with realistic fracture criteria are needed to understand the role of fracture in electrode degradation and to design mechanically robust electrodes and, potentially, life-prolonging duty cycles.

For large-scale energy storage applications, cost is of paramount importance. The levelized cost of stored energy is a figure of merit which describes the premium paid for stored energy—in addition to the cost of generation and transmission—amortized over the life of the storage device. The levelized cost of storage is given by the nameplate cost—what is paid upfront—of storage normalized by the cycle life and efficiency of the device, as shown

in Equation 1.4.

$$\text{Levelized Cost of Storage} = \frac{\text{Nameplate Cost (\$/kWh)}}{\text{Cycle Life (\#)} \times \text{Energy Efficiency}} \tag{1.4}$$

Broadly, there are two distinct strategies to reduce the levelized cost of stored energy: reduce the nameplate cost or increase the cycle life and efficiency. Degradation mechanisms such as electrochemical shock limit the energy efficiency and achievable cycle life of ion-intercalation batteries, thereby effectively increasing the levelized cost of stored energy. Thus, strategies to mitigate electrochemical shock are needed to improve life, efficiency, and ultimately to reduce the levelized cost of ion-intercalation batteries.

1.3.1 Electrochemical Shock Mechanisms

In ion-intercalation materials, there are three distinct mechanisms for electrochemical shock: 1) concentration-gradient stresses which arise during fast cycling, 2) two-phase coherency stresses which arise during first-order phase-transformations, and 3) intergranular compatibility stresses in anisotropic polycrystalline materials.

One practical classification for these electrochemical shock mechanisms is according to electrochemical cycling (C-Rate) sensitivity [45]. A C-Rate-dependent electrochemical shock mechanism is concentration-gradient stresses which develop in proportion to the applied cycling rate and become important for fast cycling. By contrast, C-Rate-independent electrochemical shock mechanisms—two-phase coherency stresses and intergranular compatibility stresses—persist to arbitrarily low C-Rates. These C-Rate-independent electrochemical shock mechanisms are expected in phase transforming and anisotropic polycrystalline materials. Only materials which are both single phase and isotropic are subject to purely C-Rate-dependent electrochemical shock; lithium-storage materials fitting this description are not common. Table 1.3 summarizes the known electrochemical shock mechanisms, their C-Rate sensitivity, the required materials properties, and some example materials in which

electrochemical shock is dominated by that mechanism.

Table 1.3: Summary of Known Electrochemical Shock Mechanisms

Mechanism	**C-Rate Sensitive?**	**Materials Properties**	**Example Materials**
Composition Gradient	Yes	Isotropic Single-phase	spinel Li_XTiS_2
Anisotropy	No	Polycrystalline Low-symmetry	$LiCoO_2$ and derivatives
Coherency Stress	No	Miscibility Gap Misfit Strain	$LiFePO_4$ $LiMn_{2-x}Ni_xO_4$

In a given material, the potentially operative electrochemical shock mechanisms are determined by the phase-behavior with respect to composition and the crystal symmetry of the intercalation compound. Both of these materials properties are evident from the composition-dependent lattice parameters, examples of which are given in Figure 1-3. Thus, Li_XFePO_4, $Li_XMn_2O_4$, and Li_XCoO_2 are all susceptible to coherency-stress fracture due to the first-order phase transformations, and Li_XFePO_4 and Li_XCoO_2 are all susceptible to compatibility-stress fracture if they are prepared in a polycrystalline form. While all intercalation materials are sensitive to concentration-gradient stresses, only in Li_XTiS_2 is this the only operative electrochemical shock mechanism. To summarize, most lithium-storage compounds are either non-cubic or have have miscibility gaps; therefore, C-Rate-independent electrochemical shock mechanisms are ubiquitous.

1.3.2 Review of Prior Work

While large volume changes and the accompanying mechanical degradation of lithium storage materials have been recognized as problematic for some time [40, 46] and numerous models have been developed to quantify the mechanical stresses generated under different electrochemical service conditions, [47, 48, 49, 50, 51, 52, 53, 54, 55, 56, 57, 58, 59, 60] relatively

few design criteria have emerged to enable rational design of electrochemical shock resistant electrode microstructures. As described in the preceding section, there are three distinct mechanisms for electrochemical shock, with unique sensitivities to microstructure (particle and primary crystallite size), electrochemical kinetics (C-Rate), and state-of-charge (composition). Thus, the relevant design criteria depend on the compound, its microstructure, and the duty cycle.

The most widely studied electrochemical shock mechanism is the C-Rate-dependent concentration-gradient mechanism. Some prior models of mechanical degradation have calculated diffusion-induced stresses—which arise from dimensional changes due to variations in composition—for battery electrode materials subjected to common electrochemical protocols. García, *et al.* developed a 2-dimensional finite element model to calculate stress profiles in composite electrodes [61]. Cheng and Verbrugge derived analytical expressions for stress evolution in spherical particles under potentiostatic and galvanostatic operation and have included surface effects in their calculation of stresses in nanoscale electrode particles [62, 63, 49]. Golmon, *et al.* use a homogenization approach to model composite electrodes and explored the effects of externally applied loads and electrode porosity [55]. Renganathan, *et al.* used a quasi-2D porous electrode model for $LiCoO_2$/Graphite cells to evaluate stresses caused by compositional inhomogeneities and phase transformations [64].

Other models have suggested certain failure criteria to predict particle fracture caused by diffusion-induced stresses, but fracture mechanics criteria were not proposed or implemented. Christensen and Newman derived a detailed general model for diffusion-induced stresses in intercalation electrodes that includes elasto-diffusion coupling, non-ideal solution thermodynamics, and nonlinear partial molar volume [48, 47]. They suggested a "tensile yield stress" criterion (assumed to be the same everywhere within the electrode) to predict the onset of fracture. Christensen has since incorporated the diffusion-induced stress model—again using a tensile yield stress failure criterion—in a quasi-2D porous electrode (Dualfoil) model

of $LiMn_2O_4$/MCMB cells [65]. Zhang, *et al.* implemented a numerical elasto-diffusion model to calculate diffusion-induced stresses in spherical and ellipsoidal electrode particles [58, 59], but suggested the von Mises equivalent stress as a predictor of electrode failure. Cheng and Verbrugge have also proposed a single value of maximum tensile stress to predict fracture [50] due to diffusion-induced stress.

In typical ion-intercalation compounds, knowledge of the diffusion-induced stress profile is necessary but insufficient to predict fracture. Yield stress and von Mises equivalent stress failure criteria are not well defined for brittle materials—these concepts from continuum plasticity theory are most appropriate for materials that undergo dislocation-mediated plastic deformation; they are yield, not fracture criteria. Instead, linear elastic fracture mechanics can provide a unique failure criterion in terms of the stress intensity factor, which incorporates both the stress profile and the pre-existing flaw population.

There is a separate body of literature where fracture mechanics analysis has been applied to the mechanical degradation of lithium alloy electrodes. In contrast to the above cited work, diffusion-induced stresses—due to composition gradients—have not been included as the driving force for fracture. Huggins and Nix developed a one-dimensional model for fracture of thin film alloy electrodes undergoing a first order phase transformation [66]. Wolfenstine proposed a critical grain size model for micro-cracking due to lithiation of tin [67] and with collaborators, measured the fracture toughness of Li_xSn alloys [68]. Aifantis, *et al.* modeled radial cracking in composite anodes composed of active particles embedded in inert matrices [69, 70, 71]. Most recently, Hu, *et al.* modeled cracks in two-phase $LiFePO_4/FePO_4$ particles with interface coherency stresses with fully anisotropic elastic constants and stress-free strains [72].

The C-Rate-independent electrochemical shock mechanisms are much less studied. Only Hu, *et al.* (Li_XFePO_4) [72] and Grantab, *et al.* (Li_XC_6) [73] have incorporated anisotropic Vegard coefficients. Of these, only Grantab, *et al.* have considered a polycrystalline mi-

crostructure, though they did not consider the possibility of grain boundary microfracture.

For phase-transforming ion-intercalation materials (*i.e.* those with miscibility gaps), electrochemical shock may occur due to coherency-stresses which develop independent of the electrochemical C-Rate. Several analyses of phase-transformation induced stresses have been performed for alloy systems, [66, 67, 68] for spherical core-shell models of isotropic electrode particles, [74, 47, 75, 64] and for anisotropic two-phase coherency stresses in single crystal particles. [72]

Thus, there is a need for refined models of electrochemical shock, which address the underlying mechanisms and incorporate failure criteria appropriate to the materials of interest. At the same time, there is an opportunity for microstructural engineering to enable mechanically robust, long-life battery electrode materials.

1.4 Critical Sizes

One central theme of this thesis is the identification and quantification of critical sizes for each of the electrochemical shock mechanisms in ion-intercalation materials.

In the most general sense, fracture is driven by a competition between reducing strain energy as a driving force and increasing total surface energy as the resistance. For elastic stresses, the total elastic strain energy is given by a volume integral

$$U_E = \int_V \frac{1}{2}\sigma_{ij}\epsilon_{ij}dV \tag{1.5}$$

As elasticity is scale-invariant, for a characteristic system linear dimension, d, and a crack of size L, the total strain energy will scale as

$$U_E = d^3 E\epsilon^2 \hat{U}\left(\frac{L}{d}\right) \tag{1.6}$$

the dimensionless function $\hat{U}\left(\frac{L}{d}\right)$ describes the shape of the elastic strain energy at different relative crack lengths, $\frac{L}{d}$. where ϵ is a characteristic strain and E is a characteristic elastic

modulus. The surface total energy is given as

$$U_{\text{surf}} = 2\gamma L d \tag{1.7}$$

Fracture is driven by a decrease of the total energy

$$\begin{aligned} U_{\text{total}} &= U_E + U_{\text{surf}} \\ &= d^3 E\epsilon^2 \hat{U}\left(\frac{L}{d}\right) + 2\gamma L d \end{aligned} \tag{1.8}$$

Fracture is possible when the total energy decreases, *i.e.*,

$$\frac{\partial U_{\text{total}}}{\partial L} = d^3 E\epsilon^2 \hat{U}'\left(\frac{L}{d}\right)\frac{1}{d} + 2\gamma d \tag{1.9}$$

$$-dE\epsilon^2 \hat{U}'\left(\frac{L}{d}\right) \geq 2\gamma \tag{1.10}$$

Define the dimensionless strain energy release rate $Z\left(\frac{L}{d}\right) = -\hat{U}'\left(\frac{L}{d}\right)$ restores this to the formalism used by Hu, *et al.* [72]. Fracture is possible when

$$Z\left(\frac{L}{d}\right) E\epsilon^2 d \geq 2\gamma \tag{1.11}$$

Thus, if the dimensionless strain-energy release rate $Z\left(\frac{L}{d}\right)$ has a maximum value $Z_{\max}$, then there is a critical length scale d_{crit}, below which fracture does not occur,

$$d_{\text{crit}} = \frac{2\gamma}{Z_{\max} E\epsilon^2} \tag{1.12}$$

This argument is based on the Griffith (thermodynamic) theory of fracture. A similar argument can be formulated in terms of the strain-energy release rate of linear-elastic fracture mechanics. In this case, the dimensionless stress-intensity factor can be defined as

$$\hat{K}\left(\frac{L}{d}\right) = \frac{K}{E\epsilon\sqrt{d}} \tag{1.13}$$

and the crack growth criterion is that

$$K \geq K_{\text{Ic}} \tag{1.14}$$

Note that here, the characteristic modulus E and characteristic strain ϵ may differ from those used in the Griffith formulation. Thus, if the dimensionless strain-energy release rate has a maximum value $\hat{K}_{\max}$ the critical size is given by

$$d_{crit} = \left(\frac{K_{\text{Ic}}}{\hat{K}_{\max} E\epsilon}\right)^2 \tag{1.15}$$

1.5 Overview of the Thesis

First, the three electrochemical shock mechanisms are analyzed independently, in the limiting cases which isolate each mechanism. Chapter 2 analyzes C-Rate-dependent electrochemical shock due to concentration-gradient stresses in isotropic, homogeneous electrode particles. Chapter 3 considers polycrystalline ensembles of anisotropic ion-intercalation materials, and identifies electrochemical shock microfracture as a C-Rate-independent electrochemical shock mechanism. Chapter 4 analyzes coherency-stress fracture of phase-transforming ion-intercalation materials. For materials with complex phase-behavior, with both regions of solid-solubility and miscibility gaps, such as $Li_XMn_2O_4$ and $Li_XMn_{1.5}Ni_{0.5}O_4$, concentration-gradient stresses and coherency-stresses are both possible; these two mechanisms are analyzed concurrently and on an equal basis in Chapter 5. In cases where it is impractical or impossible to design for complete electrochemical shock resistance, reliability statistics are needed to achieve designs with tolerable failure levels. Chapter 6 develops a stochastic method to quantify reliability statistics during electrochemical shock, considering as a particular example the problem of simultaneous anisotropic microfracture and phase-transformation in polycrystalline Li_XCoO_2. Finally, the thesis concludes with a summary of microstructure design criteria for known ion-intercalation materials and materials selection criteria for new electrochemical-shock resistant ion-intercalation materials.

THIS PAGE INTENTIONALLY LEFT BLANK

Chapter 2

Concentration-Gradient Stresses

2.1 Introduction

The first electrochemical shock mechanism is concentration-gradient (diffusion-induced) stresses, which arise during fast electrochemical cycling. Inhomogeneous composition profiles induce elastic stresses in materials with a non-zero partial molar volume of intercalating ions. These stresses are analogous to thermal stresses arising due to rapid heating or cooling, and are identical to the compositional stresses that are used to chemically temper glasses. In the limiting case of an ion-intercalation material which is isotropic, uniform, and single-phase over the entire composition range in which electrochemical cycling is performed, this mechanism will be the only active electrochemical shock mechanism.

The main objective of this chapter is to derive a fracture mechanics failure criterion for electrochemical systems having diffusion-induced stresses due to composition gradients. To achieve this goal, a rigorous theoretical framework to model diffusion in non-ideal, elasically coupled intercalation solutions is developed and applied to model electrochemical cycling of individual electrode particles. In the most general form, both stress-assisted diffusion and thermodynamic non-idealities are consistently treated in the kinetic model.

Using the particle-level electrochemical model, composition and elastic stress distributions are computed over a range of particle sizes and C-Rates. The elastic stress distributions are used to estimate the stress-intensity factor distributions, $K_{\mathrm{I}}(a,t)$, of pre-existing cracks of varying size throughout the electrochemical cycle. The stress-intensity factor is a measure of the crack-growth driving force. The methodology used to estimate the stress-intensity factor is detailed in Section 2.2.3. The time and flaw-size dependent stress-intensity factors obtain unique maximum values for a specified combination of particle size and C-Rate. These maximal stress-intensity factors are used to predict fracture for a wide range of C-Rate and particle size combinations. The electrochemical shock map is introduced as a graphical design tool which summarizes the combinations of particle size and C-Rate which can cause fracture. The methods used here follow closely on those from a previoulsy published work [1].

To analyze the effect of solution thermodynamics and elastic coupling on electrochemical and mechanical behavior, three different cases of solution thermodynamics are compared qualitatively and quantitatively: 1) an ideal solution electrode, with a Nerstian open-circuit voltage and no chemomechanical coupling, 2) an electrode with a Nernstian open-circuit voltage and a finite chemomechanical coupling, and 3) a material with an experimentally-determined open-circuit voltage profile (that of $\mathrm{Li}_X\mathrm{Mn}_2\mathrm{O}_4$) and finite chemomechanical coupling. Each of these cases, a qualitatively different composition-dependent chemical diffusivity, which affects the time-dependence of the composition, elastic stress, and stress-intensity factor profiles, but which does not alter the scaling of failure with respect to particle size and C-Rate.

2.2 Methods

To develop and quantify a fracture mechanics failure criterion for C-Rate-dependent electrochemical shock, we use individual spherical particles of an intercalation material with

complete solid solubility as a model system. We postulate that each particle of radius $r_{\max}$ contains a finite-sized semi-elliptical surface crack of length a, as shown in Figure 2-1. A few simplifying assumptions facilitate the development of this model. First, the crack faces are assumed electrochemically inert so that only the spherical outer surface of the particle is reactive. Second, the material is assumed to be homogeneous and isotropic in all respects. Finally, the elastic and fracture properties of the host material are assumed to be composition-independent.

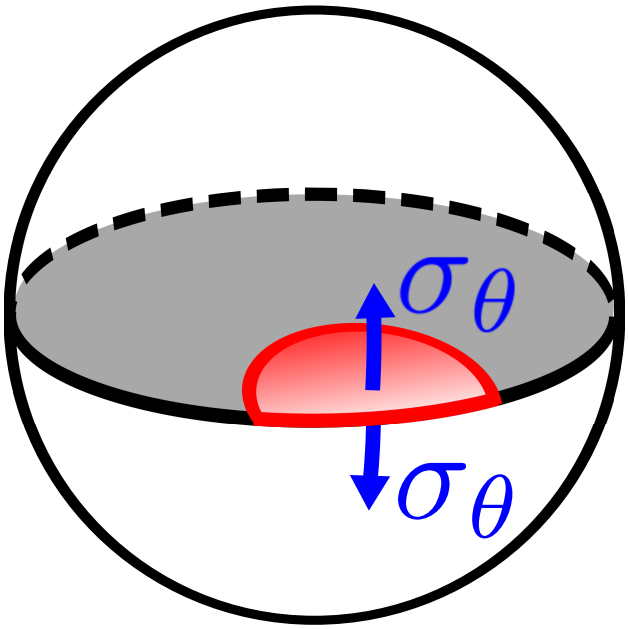

Figure 2-1: Geometry of a semi-circular crack on the surface of a spherical electrode particle. A tensile tangential stress, σ_θ acts to increase the size of the crack.

2.2.1 Diffusion in Non-ideal, Elastically Coupled Intercalation Solutions

Electrochemical cycling of the particle is modeled by the diffusion equation

$$\frac{\partial X}{\partial t} = -\nabla \cdot \mathbf{J} \tag{2.1}$$

where X is composition which is scaled to take values $0 \leq X \leq 1$, *e.g.* X in $\mathrm{Li}_X\mathrm{Mn}_2\mathrm{O}_4$ and $\mathbf{J}$ is the flux, which is proportional to the gradient in the relevant diffusion potential Φ

$$\mathbf{J} = -MX\nabla\Phi \tag{2.2}$$

The diffusion potential is the generalized thermodynamic driving force which reflects all of the energy change in a system due to motion of a species. [76] For a non-ideal, elastically coupled solution, the diffusion potential is

$$\Phi = \mu^0 + RT \ln\left(\gamma \, \frac{X}{1-X}\right) - \Omega\sigma_h \tag{2.3}$$

In addition to the composition, X, the diffusion potential Φ contains μ^0, a reference chemical potential; γ, an activity coefficient describing the thermodynamic non-ideality of the concentrated solution; Ω, the partial molar volume of the diffusing species; and σ_h, the local hydrostatic stress. R is the gas constant and T the absolute temperature. Using this formalism, the diffusion equation for traction-free spherical particles of an ion-intercalation material can be expressed as

$$\frac{\partial X}{\partial t} = \frac{1}{r^2}\frac{\partial}{\partial r}\left(r^2 \tilde{D}(X)\frac{\partial X}{\partial r}\right) \tag{2.4}$$

where $\tilde{D}(X)$ is a composition-dependent chemical diffusivity defined as

$$\tilde{D}(X) = D_0 X\,(1-X)\left(-\frac{z\mathcal{F}}{RT}\frac{\partial V(X)}{\partial X} + \hat{\theta}\right) \tag{2.5}$$

D_0 is a characteristic diffusivity, $\mathcal{F}$ is Faraday's constant, z is the formal charge of the intercalating ion, and $V(X)$ is the composition-dependent open-circuit voltage of the intercalation electrode in a half-cell, and $\hat{\theta}$ is a dimensionless chemomechanical coupling parameter. The composition-dependent open-circuit voltage $V(X)$ is a direct measure of the chemical potential of the intercalating ions in the intercalation host and it can be used to uniquely define the activity coefficient γ. The dimensionless chemomechanical coupling parameter, $\hat{\theta}$, is defined as

$$\hat{\theta} = \frac{2\Omega^2 E c_{\max}}{9RT(1-\nu)} \tag{2.6}$$

Table 2.1: Chemomechanical coupling parameter $\hat{\theta}$ for a number of important lithium-storage materials.

Property	$Li_XMn_2O_4$	Li_XCoO_2	Li_XFePO_4
E (GPa)	143 [78]	174 [79]	124 [80]
ν	0.3	0.3	0.28 [80]
Ω_{Li} (cm^3/mol)	3.26 [14]	-0.77 [7]	2.87 [12]
$c_{\max}$ (mol/m^3)	2.37×10^4 [81]	5.11×10^4 [82]	2.29×10^4 [83]
$\hat{\theta}$	4.57	0.67	2.87

where c_{max} is the maximum concentration (units of mol/m^3), E is the Young's modulus, and ν is Poisson's ratio. This chemomechanical coupling factor arises from the hydrostatic stress dependence of the diffusion potential, and conventiently for traction-free spherical particles, it can be expressed uniquely in terms of the local composition gradient [77, 58]. A detailed derivation of Equation 2.5 is given in Appendix B.2.

Table 2.1 lists values of the chemomechanical coupling parameter $\hat{\theta}$ for the common cathode materials $Li_XMn_2O_4$, Li_XCoO_2, and Li_XFePO_4. It is important to note that $\hat{\theta}$ is strictly greater than zero for any stable material. While the partial molar volume, Ω, may be positive or negative, $\hat{\theta}$ depends on Ω^2 which is always positive. As the Poisson's ratio must take values $-1 \leq \nu \leq 1/2$, the quantity $(1-\nu)$ is always positive; the remaining quantities comprising $\hat{\theta}$ are all strictly positive.

This particle-level model for electrochemical cycling is strictly valid for materials which remain in a single-phase over the entire composition range in which electrochemical cycling is performed. However, several models have been suggested which use experimentally-determined open-circuit voltage profiles as an approximate method for phase-transforming electrodes [84, 85]. The possibility of using such a method for electrochemical shock modeling is critically examined.

2.2.2 Elastic Stress Distributions

The diffusion-induced elastic stress distributions are determined by solving a linear elastic boundary value problem analogous to the calculation of thermal stresses [86]. Assuming isotropic linear elasticity and traction free boundaries, the radial and tangential stress profiles in a solid spherical particle are

$$\sigma_r(r,t) = \frac{2\Omega E c_{\max}}{9(1-\nu)} \left[X_{av}(r_{\max},t) - X_{av}(r,t)\right] \tag{2.7}$$

$$\sigma_\theta(r,t) = \frac{\Omega E c_{\max}}{9(1-\nu)} \left[2X_{av}(r_{\max},t) + X_{av}(r,t) - 3X(r,t)\right] \tag{2.8}$$

where Ω is the partial molar volume of the intercalating species ($\mathrm{cm}^3/\mathrm{mol}$), E is the Young's elastic modulus (GPa), ν is the Poisson's ratio (dimensionless), $c_{\max}$ is the maximum concentration ($\mathrm{mol}/\mathrm{m}^3$), and $X_{av}(r,t)$ is the average composition within a sphere of radius r

$$X_{av}(r,t) = \frac{3}{r^3}\int_0^r X(r,t) r^2 \mathrm{d}r \tag{2.9}$$

These expressions are valid for both single-phase and two-phase configurations, assuming that Ω and E are composition-independent. A derivation of these expressions is given in Appendix B.1.

2.2.3 Estimating Stress-Intensity Factor

Linear-elastic fracture mechanics provides a deterministic failure criterion in terms of the stress-intensity factor, which characterizes stress concentration ahead of a flaw. For the simple case of uniform tension, a material subjected to a stress σ containing a single flaw of characteristic size a experiences a stress-intensity factor $K = Y\sigma\sqrt{\pi a}$ where Y is a dimensionless geometric factor. The stress-intensity factor is conventionally expressed in SI units of $\mathrm{MPa}\cdot\mathrm{m}^{1/2}$. For a classical reference on fracture mechanics, see the text by Lawn [87].

A material's resistance to crack growth is described by a critical value of the stress-intensity factor, K_{Ic}, known as the fracture toughness. When the applied stress-intensity factor exceeds the material's fracture toughness, the pre-existing crack grows. We stress that the fracture toughness is a material property, whereas the fracture strength–that is, the stress necessary to induce crack growth–is not. Fracture strength depends on flaw geometry, loading conditions, and material properties. The crack propagation criterion in linear elastic fracture mechanics is consistent with thermodynamic free energy minimization. This criterion embodies the competition between a driving force from elastic strain energy—enhanced by the stress concentration around flaws—and a resistance due to the creation of fresh surface area. Models that assume a single threshold stress as a fracture criterion do not reflect the minimum free energy configuration for the system, and therefore do not accurately predict fracture.

We calculate stress-intensity factors using the method of weight functions and an edge-cracked plate approximating geometry, shown in Figure 2-2. The dimensions of the plate are related to those of the sphere as

$$l = r_{\max} \qquad b = \pi r_{\max} \qquad h = \pi r_{\max} \tag{2.10}$$

The stress-intensity factor of this plate under uniform tensile loading is used as the reference case for the method of weight functions, details of which are provided in Appendix A.5. This geometric approximation avoids an unrealistic assumption of a uniform stress profile, yet does not require the intricacy of a full-scale finite element model. This approximation will not affect the character of the solution (*i.e.*, the scaling with respect to flaw size and material parameters), and therefore serves to provide qualitative insight on the behavior of cracks subjected to non-uniform diffusion-induced stress profiles.

The stress-intensity factor for the electrochemical shock problem can be calculated fol-

lowing the approach of Mattheck [88], by the integral equation

$$K_{\mathrm{I}} = \frac{E}{K_{ref}(1-\nu^2)} \int_0^a \sigma(x) m(x,a) \mathrm{d}x \tag{2.11}$$

where K_{ref} is the reference stress-intensity factor and $m(x,a)$ is the weight function (a kernel or Green's function) against which the diffusion-induced stress profile is integrated. We use the time-dependent tangential stress distributions $\sigma_\theta(x,t)$ as input to this calculation to produce stress-intensity profiles which are functions of flaw size and time $K_{\mathrm{I}}(a,t)$. The stress distribution are subject to the change of variables $x = r_{\max} - r$.

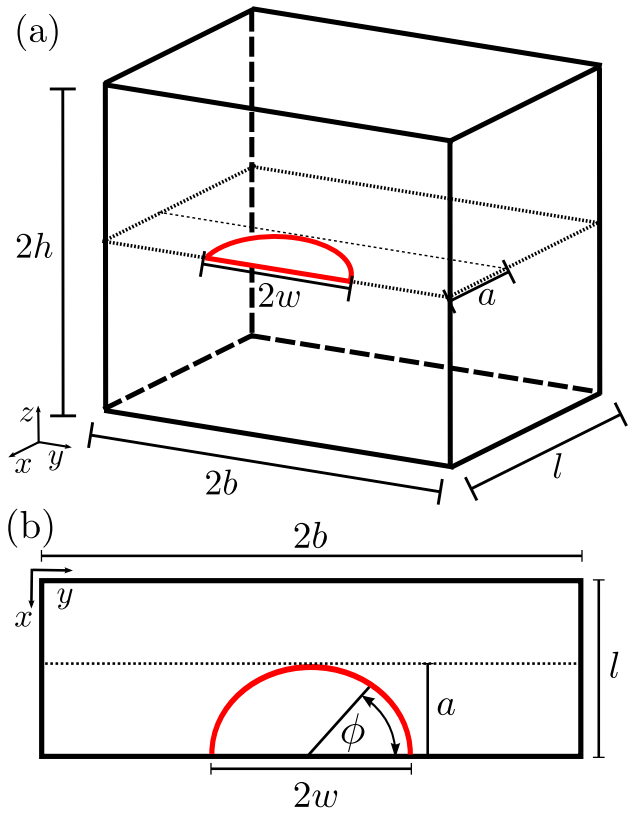

Figure 2-2: Geometry of plate model used to calculate stress-intensity factors under the non-uniform stress profiles. (a) Full view of plate. (b) Plan view of the crack plane. To match the plate and sphere models, we take $l = r_{\max}$, $b = \pi r_{\max}$, $h = \pi r_{\max}$. As a simplifying case, we consider only semi-circular cracks where $w = a$.

An essential feature of Equation 2.11 is that the stress distribution is integrated over the entire crack length; this means that the spatial variation of the stress profile matters. A

moderate, uniform stress profile can induce a stress-intensity factor greater than a sharply peaked but rapidly decreasing stress profile; this effect is important for electrochemical shock at large currents. To generate a large stress-intensity factor, the diffusion-induced stress must be large at the crack tip, not just at the particle surface. The weight function $m(x, a)$ is characteristic of the reference case; more details are given in Appendix A.5 and the original literature [88, 89].

The reference case is uniform tensile loading in the z-direction of the semi-elliptical surface cracked plate [90]. The stress-intensity factor calculated in this way is a function of crack dimensions a and w and the angle ϕ, all shown in Figure 2-2(b). As a simplifying case, we restrict our analysis to semi-circular cracks with $w = a$. Results not presented here show that $\phi = 0$ (and $\phi = \pi$, as required by the symmetry of the problem) is the direction of maximum stress-intensity factor, so we consider only this direction. We neglect Mode II and III crack face loading because the material's other toughness values, K_{IIc} and K_{IIIc}, are generally much larger than K_{Ic}.

The fracture toughnesses of most ion-intercalation materials are presently unknown, but can be determined experimentally. Measurements of fracture toughness in $LiCoO_2$ give a value $\sim 1 - 2$ MPa·m$^{1/2}$ which is similar to other oxide materials. In this chapter, when a numerical fracture toughness is needed for analysis, we present results for a range of values representative of brittle materials.

2.2.4 Dimensionless Variables

For numerical calculations, and to report values which are meaningful for a variety of materials systems, we make the problem dimensionless by normalizing all lengths to the particle radius and we define the dimensionless stress-intensity factor as

$$\hat{K}_{\mathrm{I}} = \frac{9(1-\nu)K_{\mathrm{I}}}{c_{\max}\Omega E\sqrt{r_{\max}}} \tag{2.12}$$

Note that this definition of the dimensionless stress-intensity factor differs from one that we have previously reported [1]; the present definition is more general as all materials properties are subsumed into the dimensionless variables.

Numerically, we implement the electrochemical model in dimensionless variables

$$\hat{r} = \frac{r}{r_{\max}} \qquad \hat{t} = \frac{tD_0}{r_{\max}^2} \tag{2.13}$$

And the stress-intensity factor is computed in dimensionless variables normalized to the dimension of the particle ($r_{\max}$).

$$\hat{l} = 1 \qquad \hat{b} = \pi \qquad \hat{h} = \pi \tag{2.14}$$

2.2.5 Boundary and Initial Conditions

The boundary conditions for constant current charging of a spherical particle are zero flux at the particle center and constant flux at the particle surface. In the dimensionless variables, the boundary conditions are

$$\left.\frac{\partial X}{\partial \hat{r}}\right|_{\hat{r}=0} = 0 \qquad \left.\frac{\partial X}{\partial \hat{r}}\right|_{\hat{r}=1} = -\frac{\hat{I}}{\tilde{D}(X|_{\hat{r}=1})} \tag{2.15}$$

with the surface flux specified as a dimensionless current $\hat{I}$

$$\hat{I} = \frac{(\text{C-Rate})\alpha\rho r_{\max}^2}{3D_0 c_{\max}\mathcal{F}} \tag{2.16}$$

where α is the theoretical capacity (Ah/kg) and ρ is the mass density (kg/m^3). C-Rate describes the normalized charging rate of a cell and has units of h^{-1}. A C/n charge accumulates the full theoretical capacity of a cell in n hours. For example, a cell charged at a 2C rate reaches its theoretical capacity in 30 min.

In brittle materials, surface flaws subjected to tensile stresses are the most common origin of catastrophic failure. For this reason, we simulate charging (de-intercalation) of an ion-intercalation material with a positive partial molar volume, which produces surface tensile stresses that tend to open the pre-existing crack, as illustrated in Figure 2-1. Analogous tensile stresses would develop during discharge (intercalation) of a material with a negative partial molar volume.

To compare the results for the three different cases of solution thermodynamics, consistent stoichiometric limits $0.2 \leq X \leq 0.995$ are used to model electrochemical cycling. In the final case, where the open-circuit voltage of $Li_XMn_2O_4$ is used, these compositions correspond to conventional cutoff voltages for electrochemical cycling (3.6 - 4.2 V vs. Li^+/Li).

In each case, the initial condition is uniform concentration in the fully lithiated (discharged) state

$$X(r, t = 0) = 0.995 \tag{2.17}$$

And simulations are terminated when the surface composition reaches $X(r_{\max}, t) = 0.2$.

2.2.6 Materials Properties for Dimensional Results

To illustrate the results, quantitative examples are provided. An illustrative example with $\hat{I} = 0.5$, embodied as a 5C galvanostatic charge of a 23 μm particle is used to provide dimensionalized (*i.e.*, physical units of measure) results. When quantitative values of materials properties are needed, those corresponding to the spinel $LiMn_2O_4$ are used. The complete set of material properties used as model input is given in Table 2.2. With these materials properties, the chemomechanical coupling parameter for $Li_XMn_2O_4$ is estimated at $\hat{\theta} = 4.577$.

Table 2.2: Properties of $Li_XMn_2O_4$ used in numerical calculations. References are given for information taken from or derived from the literature.

Property	**Symbol**	**Units**	**Value**
Young's modulus	E	GPa	143 [78]
Poisson's ratio	ν	-	0.3 [78]
Characteristic diffusivity	D_0	cm^2/s	6×10^{-9} [91]
Partial molar volume	Ω	cm^3/mol	3.26 [14]
Maximum concentration	c_{max}	mol/m^3	2.37×10^4 [81]
Density	ρ	g/cm^3	4.28 [81]
Theoretical capacity	α	mAh/g	148 [81]
Temperature	T	K	300

2.3 Effect of Solution Thermodynamics on Composition-Dependent Diffusivity

In this section, the three cases of solution thermodynamics are introduced, and the composition-dependent chemical diffusivities are derived and compared.

First, consider an ideal solution ion-intercalation material, where the open-circuit voltage arises only from configurational entropy, and the open-circuit potential is given as

$$V(X) = V_0 - \frac{RT}{z\mathcal{F}} \ln\left(\frac{X}{1-X}\right) \tag{2.18}$$

where V_0 is a reference potential. The shape of this Nernstian open-circuit voltage is shown in Figure 2-3, plotted as the potential relative to the reference potential, $V(X) - V_0$.

For this first case, with no chemomechanical coupling ($\hat{\theta}$=0), the diffusivity is independent of composition, and the diffusion equation reduces to Fick's Second Law, *i.e.*

$$\frac{\partial X}{\partial t} = D_0 \nabla^2 X \tag{2.19}$$

For the second case, consider a material also with a Nernstian open-circuit voltage, but with finite chemomechanial coupling. The chemical diffusivity becomes composition-dependent and is given as

$$\tilde{D}_{\text{ideal}}(X) = D_0 \left[1 + X(1-X)\hat{\theta}\right] \tag{2.20}$$

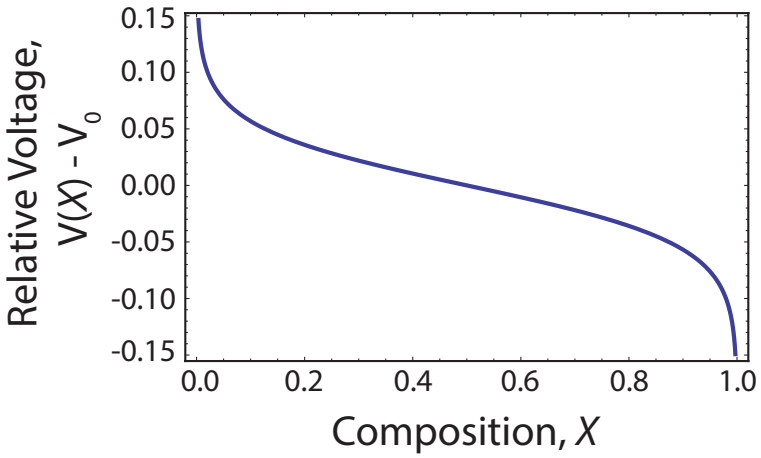

Figure 2-3: Variation of open-circuit voltage for a Nernstian electrode, relative to an unspecified reference potential V_0 and assuming a monovalent ion, $z = 1$.

Chemomechanical coupling enhances the diffusivity relative to an ideal solution, and the effect is symmetric with respect to composition about $X = 0.5$. The shape and magnitude of this enhancement is illustrated in Figure 2-4, where $\frac{\tilde{D(X)}}{D_0}$ is plotted as a function of X, showing the enhancement of the chemical diffusivity relative to the characteristic diffusivity D_0. This enhancement factor is plotted for several values of the chemomechanical coupling parameter, $0 \leq \hat{\theta} \leq 8$, encompassing the range of values of common Li-storage materials as given in Table 2.1. It is important to note that this chemomechanical coupling, which is thermodynamic in origin, will *always* enhance diffusion, as $\hat{\theta}$ is strictly greater than zero for any stable material. Other chemomechanical coupling effects are possible, for example, if there is a significant activation volume (migration volume), the diffusivity will have an exponential dependence on the stress, and will be sensitive to the sign of the stress. Such dependence is not considered in the present work. For $\mathrm{Li}_X\mathrm{Mn}_2\mathrm{O}_4$, the chemomechanical coupling parameter is $\hat{\theta} = 4.57$ and with this value of the chemomechanical coupling parameter, the composition-averaged diffusivity enhancement is 1.9.

The third case is a material with an experimental open-circuit voltage corresponding to $\mathrm{Li}_X\mathrm{Mn}_2\mathrm{O}_4$ and finite chemomechanical coupling. To quantify the composition-dependent

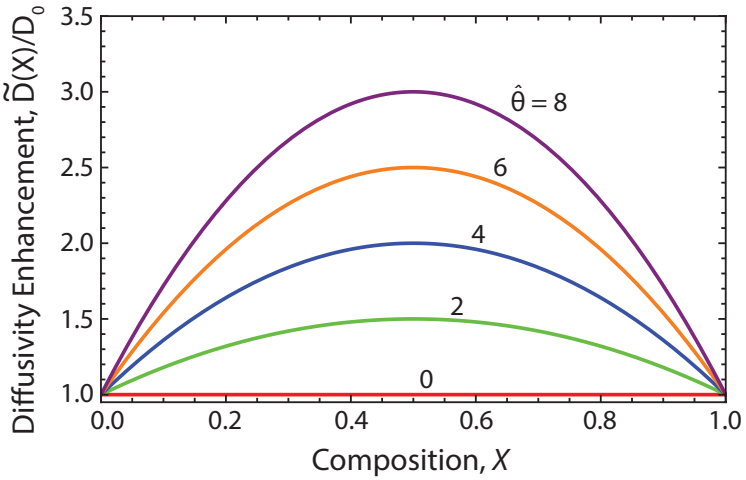

Figure 2-4: Enhancement of the chemical diffusivity $\frac{\tilde{D}(X)}{D_0}$ for a range of values of the chemomechanical coupling parameter $\hat{\theta}$ and with an ideally Nernstian open-circuit voltage.

chemical diffusivity using Equation 2.5, the open-circuit voltage $V(X)$ of $Li_XMn_2O_4$ is specified using the function fit by Doyle, *et al.* [92], which is given in the Appendix as Equation B.36 and is plotted in Figure 2-5(a). The key features of the open circuit voltage are the plateau-like regions at 4.0 V ($0.6 \leq X \leq 0.995$) and 4.1 V ($0.5 \leq X \leq 0.25$), and the region of rapidly varying open circuit voltage for intermediate compositions ($X \approx 0.6$). The lower 4.0 V region is a single phase of continuously varying composition, $0.5 \leq X \leq 0.995$. In real $Li_XMn_2O_4$, the upper 4.1 V plateau is due to two-phase coexistence between a Li-rich phase α, with composition $X_\alpha = 0.5$, and a Li-poor phase β, with composition $X_\beta = 0.25$. For the purposes of the present analysis, this 4.1 V region is assumed to be a single-phase plateau-like region analogous to the lower 4.0 V region. The effect of two-phase coexistence in $Li_XMn_2O_4$ is considered in detail in Chapter 4 and the present model for electrochemical cycling is revised in Chapter 5 to account for the phase-transformation. The assumption of continuous solid solubility is valid for a material such as $Li_XMn_{1.5}Ni_{0.42}Fe_{0.08}O_4$, which is shown in Chapter 4 to be single-phase and has an open-circuit voltage with a shape similar to that of $Li_XMn_2O_4$.

While the present model is strictly valid for single-phase materials, similar models us-

ing experimentally-determined open-circuit voltage profiles have been suggested as approximate methods for phase-transforming electrodes [84, 85]. In this chapter, the possibility of using such a method for electrochemical shock modeling of phase-transforming ion-intercalation materials is critically examined. By comparing the results obtained for single-phase "$Li_XMn_2O_4$-like" material to experimental observations in $Li_XMn_2O_4$, the validity of this approximate method may be assessed.

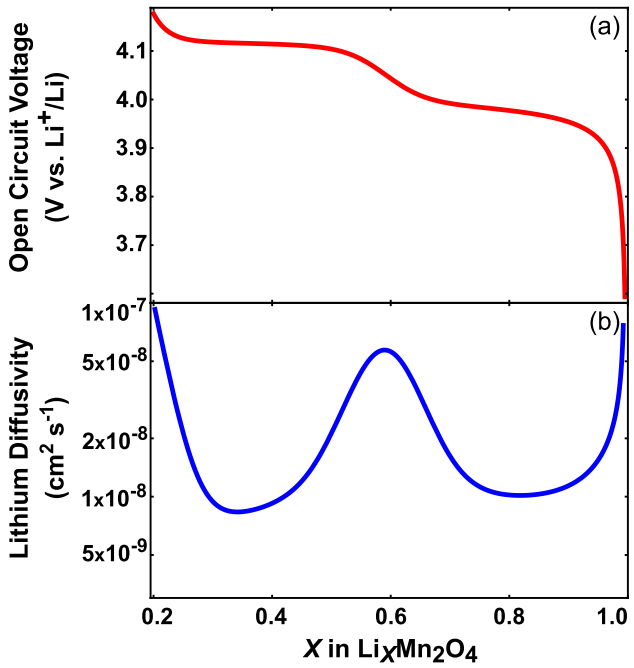

Figure 2-5: (a) Open circuit voltage of $Li_XMn_2O_4$ as given in Ref [92] for $0.2 \leq X \leq 0.995$. (b) Composition-dependent chemical diffusivity of "$Li_XMn_2O_4$-like" material with $D_0 = 6 \times 10^{-9}$ cm^2/s and $\hat{\theta} = 4.57$ plotted according to Equation 2.5. This matches the qualitative behavior seen in experimental data for $Li_XMn_2O_4$.

For the "$Li_XMn_2O_4$-like" material, there is a close correspondence between features in the open-circuit voltage and features in the chemical diffusivity. Figure 2-5(b) shows the composition-dependent chemical diffusivity determined from Equation 2.5. The composition-dependent chemical diffusivity $\tilde{D}(X)$ is quantified assuming a constant characteristic diffusivity $D_0 = 6 \times 10^{-9}$ cm^2/s and a chemomechanical coupling factor $\hat{\theta} = 4.57$. At compositions where the open circuit voltage changes sharply, *e.g.* $X \approx 0.6$, the chemical diffusivity spikes;

conversely, at compositions where the open circuit voltage is plateau-like, the chemical diffusivity is low. This chemical diffusivity $\tilde{D}(X)$ is in good agreement with the shape of the experimentally measured chemical diffusivity [91].

The close correspondence between the open-circuit-voltage and the chemical diffusivity can be rationalized in terms of chemical driving forces. When the open-circuit voltage curve is flat, a large composition change is necessary to induce an appreciable change in the chemical potential. Conversely, when the open-circuit voltage curve is rapidly varying, a small composition change induces a large change in chemical potential. Since the diffusion potential (a generalized chemical potential), Φ, is the true driving force for diffusion, but we wish to describe diffusion in terms of composition, the composition-dependent chemical diffusivity provides the link between the driving force and the composition field. Note that the two end-member compositions surrounding the two-phase region have nearly equal diffusivities: $\frac{\tilde{D}(0.5)}{\tilde{D}(0.25)} = 1.05$.

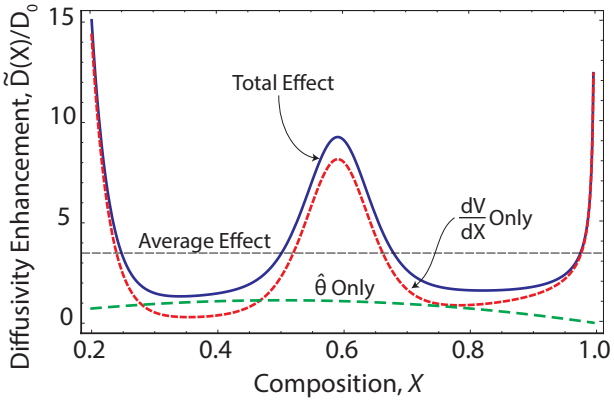

Figure 2-6: Enhancement of the chemical diffusivity $\frac{\tilde{D}(X)}{D_0}$ for the "$Li_XMn_2O_4$-like" material. The total enhancement is shown as the blue solid curve, and this is decomposed into contributions from chemomechanical-coupling and open-circuit voltage effects.

The open-circuit voltage term modulates the composition-dependent chemical diffusivity by an order of magnitude. The chemomechanical and open-circuit voltage contributions to the composition-dependent diffusivity shown in Figure 2-5(b) can be decomposed by taking

the limits that $\hat{\theta} \to 0$ and $\frac{\partial V(X)}{\partial X} \to 0$, as shown in Figure 2-6. The two contributions sum to the total chemical diffusivity. The composition-averaged diffusivity enhancement over the range on which electrochemical cycling is modeled, $0.2 \leq X \leq 0.995$ is 3.43, and is shown as the dashed horizontal line in Figure 2-6.

2.4 Composition Profiles

The composition profiles $X(r,t)$ are strongly and clearly affected by the shape of the chemical diffusivity $\tilde{D}(X)$. Figure 2-7 shows the time evolution of the composition at three different radial positions during the 5C charge of Nernstian particles with no chemomechanical coupling ($\hat{\theta} = 0$) and with chemomechanical coupling equal to that in $\mathrm{Li}_X\mathrm{Mn}_2\mathrm{O}_4$ ($\hat{\theta} = 4.57$). In both cases, the composition monotonically decreases at all radial positions, as expected for deintercalation. To illustrate the effect of the composition-dependent diffusivity on the composition gradient in a particle, Figure 2-8(b) shows the composition difference between the particle surface and center $\Delta X(t) \equiv X(r = 0, t) - X(r = r_{\max}, t)$ as a function of time during the constant current charge. The composition drop $\Delta X(t)$ scales with the average composition gradient in the particle. At all times, the composition drop is positive, as the surface composition is always lower (less lithium content) than the bulk of the particle. In the particle with no chemomechanical coupling, the composition difference across the particle monotonically increases, with a rapid initial incease and an asymptotic approach to a steady-state value. In the particle with chemomechanical coupling, there is a similar transient, but with a local maximum. The maximum occurs because of the increasing diffusivity which is obtained by a small amount of deintercalation, which helps to smooth out the composition gradient.

Figure 2-8 shows the same composition plots for the "$\mathrm{Li}_X\mathrm{Mn}_2\mathrm{O}_4$-like" material, also for a 23 μm particle subjected to a 5C constant current charge. The double-well shape of

the chemical diffusivity $\tilde{D}(X)$ clearly affects the time-dependent composition drop through the particle $\Delta X(t)$. During the electrochemical charge cycle, the composition drop initially increases, then decreases to nearly zero at $t \approx 250$ s, and finally increases again to a maximum. The decrease in the composition drop at intermediate times happens when the volume averaged composition is $\bar{X} \approx 0.6$, where the chemical diffusivity $\tilde{D}(X)$ is locally maximized.

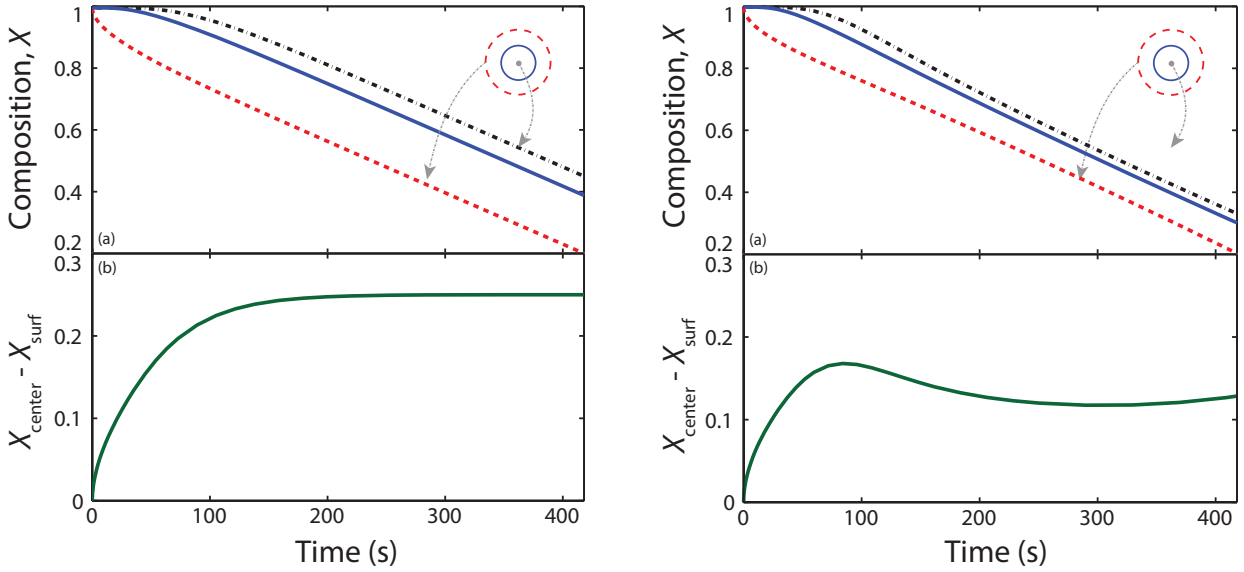

Figure 2-7: Composition, $X(r,t)$, at three different radial depths and Composition drop $\Delta X(t)$—the difference in composition between the particle center and particle surface—for Nernstian materials with (left) no chemomechanical coupling $\hat{\theta} = 0$ and (right) finite chemomechanical coupling $\hat{\theta} = 4.57$. The composition difference $\Delta X(t)$ scales with the average composition gradient in the particle. Both cases are quantified for a 23 μm particle charged at a 5C rate, corresponding to a dimensionless current of $\hat{I} = 0.5$.

2.5 Stress Profiles

The spatially inhomogeneous composition profiles give rise to diffusion-induced stresses in these particles. Figure 2-9 shows the spatial distribution of the tangential and radial stress profiles in Nernstian particles with no chemomechanical coupling ($\hat{\theta} = 0$) charged at C-Rates of 1C, 2.5C and 5C, which correspond to dimensionless currents of $\hat{I} = 0.1$, 0.25, and 0.5,

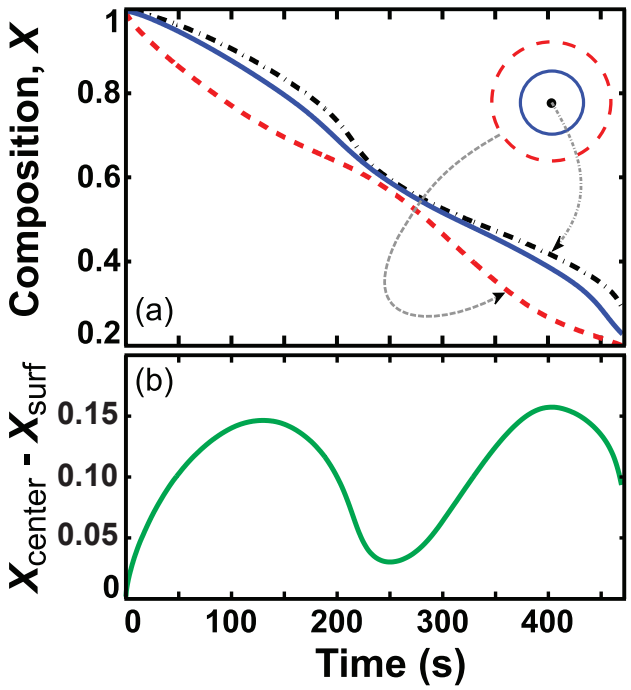

Figure 2-8: Composition, $X(r,t)$, at three different radial depths and composition drop $\Delta X(t)$ for a 23 μm "$Li_XMn_2O_4$-like" particle subject to a 5C constant current charge, corresponding to a dimensionless current of $\hat{I} = 0.5$.

respectively. Each snapshot is taken at the time corresponding to the maximum stress-intensity factor for that C-Rate. The spatial profiles are qualitatively identical for all three cases of solution thermodynamics and at all C-Rates; the time-dependence and magnitudes of the stresses are quantitatively different among the three cases. In all three cases, the magnitude of the stresses scale with the dimensionless current. Radial stresses are zero a particle surface, as required by the traction-free boundary condition; at particle center, there is hydrostatic compression, with $\sigma_r = \sigma_h$. As expected for de-intercalation of a material with a positive partial molar volume of lithium, the surface tangential stress is tensile (positive), while the tangential stress at the particle center is compressive. The spatial profile would be reversed for discharge or if the partial molar volume was negative.

Figure 2-10 shows the time evolution of the tangential stress profile at five different radial positions during the 5C charge for particles with no chemomechanical coupling ($\hat{\theta} = 0$) and

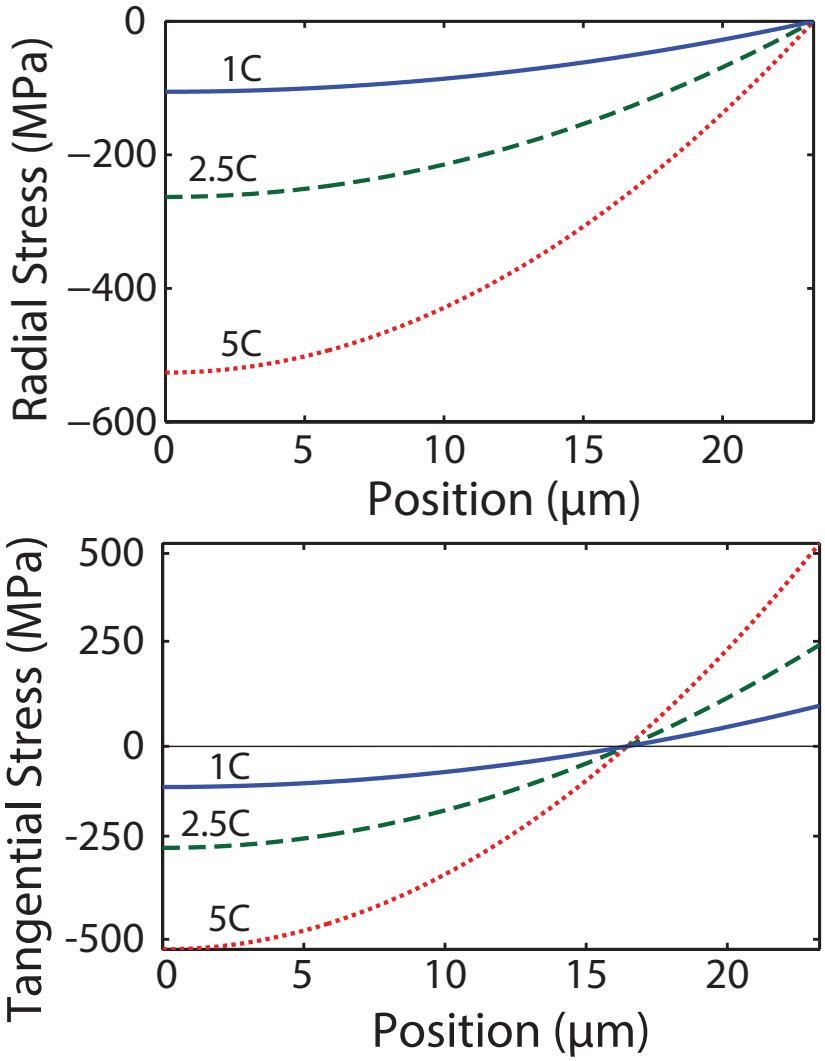

Figure 2-9: Radial and tangential (hoop) components of the elastic stress distributions distributions at the time of maximum dimensionless stress-intensity factor $\hat{K}_{\mathrm{I}}$ for 23 μm particles with Nernstian potential with no chemomechanical coupling $\hat{\theta} = 0$, charged at C-Rates of 1C, 2.5C, and 5C, corresponding to at dimensionless currents of $\hat{I} = 0.1$, 0.25, and 0.5.

with chemomechanical coupling equal to that in $Li_XMn_2O_4$ ($\hat{\theta} = 4.57$). The time evolution of these stress profiles closely mirrors the behavior observed in the composition profiles. At the same particle size and C-Rate, the hoop stresses are more severe in the particle with no chemomechanical coupling; the chemomechanical coupling effectively increases the diffusivity, which allows the system to resist the large stresses induced by severe composition gradients.

As the elastic stress distributions are determined by the composition profile, these quantities have the same qualitative time dependence as the composition drop $\Delta X(t)$. In the Nernstian particle without chemomechanical coupling, the hoop stress profiles rise and reach steady state values. In the chemomechanically coupled particle, there is a non-monotonic behavior associated with the shape of the composition-dependent chemical diffusivity. There is initially a rise, but as the composition is changed, the diffusivity is increasing, and these two factors trade off, giving rise to a local extrema in the stresses. Figure 2-11 shows the hoop stress profiles for the "$Li_XMn_2O_4$-like" material, which are clearly affected by the double-well shape of the chemical diffusivity. The hoop stress profiles show the same key temporal features noted in the composition drop: the stresses reach local extrema early in the charge cycle, decrease to nearly zero at intermediate time when the particle composition homogenizes, then increase again to global extrema in the latter part of the charge cycle.

2.6 Stress-Intensity Factor Profiles

Figure 2-12 shows the instantaneous stress-intensity factor–flaw size curves for the 23 μm Nernstian particles with no chemomechanical coupling, charged at C-Rates of 1C, 2.5C, and 5C. These are computed from the tangential stress distributions shown in Figure 2-9, and these are snapshots at the time of maximum stress-intensity factor for the respective simulations. The magnitude of the stress-intensity factor scales with electrochem-

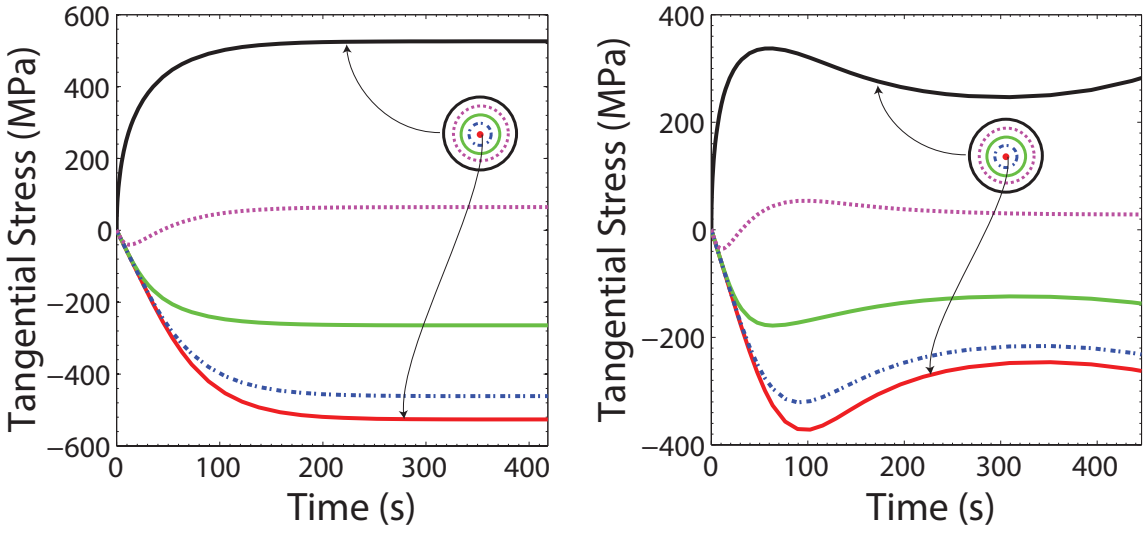

Figure 2-10: Hoop stress distributions $\sigma_\theta(r,t)$ for Nernstian particles with (a) no chemomechanical coupling $\hat{\theta} = 0$ and (b) finite chemomechanical coupling $\hat{\theta} = 4.57$. Both cases are quantified for 23 μm particles charged at a 5C rate, corresponding to a dimensionless current of $\hat{I} = 0.5$.

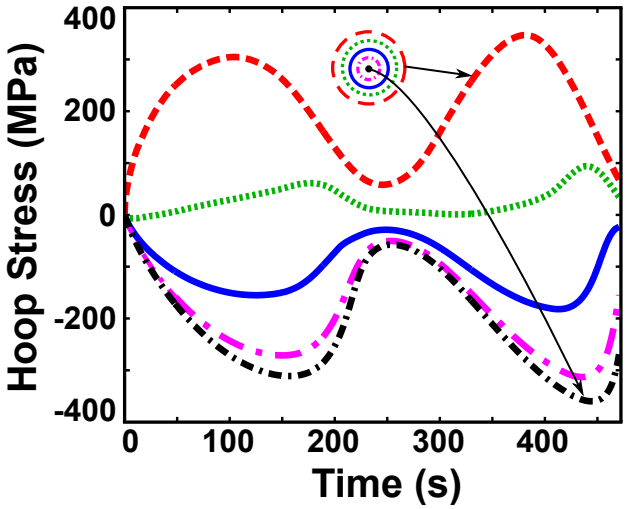

Figure 2-11: Hoop stress $\sigma_\theta(r,t)$ for the "$Li_XMn_2O_4$-like" material, plotted against time at five different radial positions for a 23 μm particle during a 5C charge, corresponding to a dimensionless current of $\hat{I} = 0.5$.

ical cycling rate. The stress-intensity factor is decreased when chemomechanical coupling is present. These stress-intensity factor–flaw size curves have the same qualitative shape for all three solution thermodynamic cases, and at all times in each of those cases; the time-dependence and magnitudes are different in all three cases.

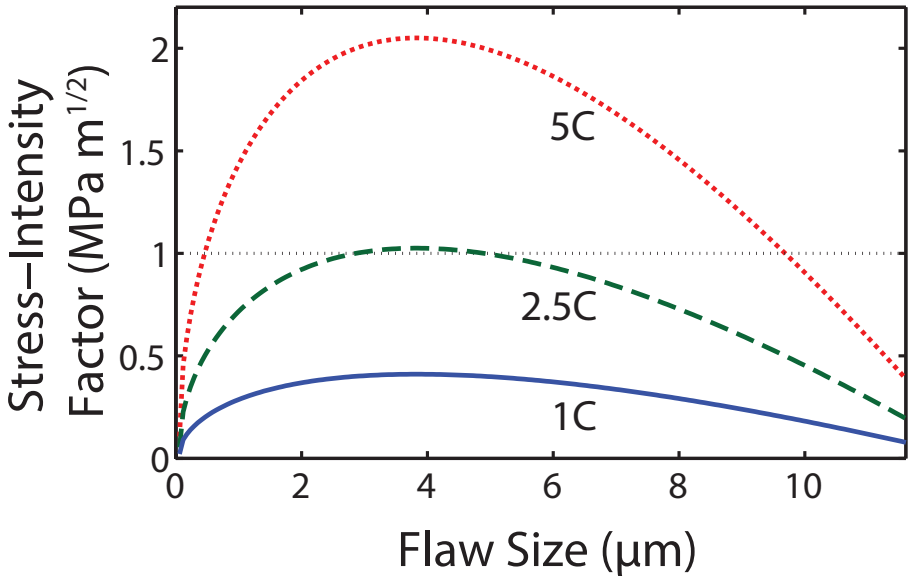

Figure 2-12: Stress-intensity factor $K_{\mathrm{I,max}}$ as a function of flaw size a for 23 μm Nernstian particles with no chemomechanical coupling ($\hat{\theta} = 0$), charged at C-Rates of 1C, 2.5C, and 5C, which correspond to dimensionless currents of $\hat{I} = 0.1$, 0.5, and 1, respectively. At each C-Rate, the stress-intensity factor increases rapidly for small flaws, but quickly reaches a maximum and decreases, becoming negative for very large flaws. The dashed horizontal line represents a plausible value of fracture toughness, $K_{\mathrm{Ic}} = 1$ MPa·m$^{1/2}$.

Figure 2-13 shows the time and flaw-size dependent stress-intensity factor profiles for the two Nerstian particles charged at 5C rate, visualized as contour maps. The overall magnitudes of the stress-intensities are greater without chemomechanical coupling. The time dependence of the stress-intensity factor profiles matches that observed in the composition drops $\Delta X(t)$ and the hoop stresses $\sigma_\theta(r,t)$. For Nernstian particles with no chemomechanical coupling, the stress-intensity factor increases monotonically at a fixed flaw size. For the Nernstian particle with chemomechanical coupling, there is non-monotonic behavior matching the time-dependence of the tangential stress profile. Figure 2-14 shows the dynamics

stress-intensity factor profile for the "$Li_XMn_2O_4$-like" case, where the double-peaked time-dependence mirrors the behavior oberved in the composition drop and hoop stress profiles for this case. In all three solution thermodynamic cases, the instantaneous stress-intensity factor–flaw size curves have the same shape as those shown in Figure 2-12, but the magnitudes are time-dependent.

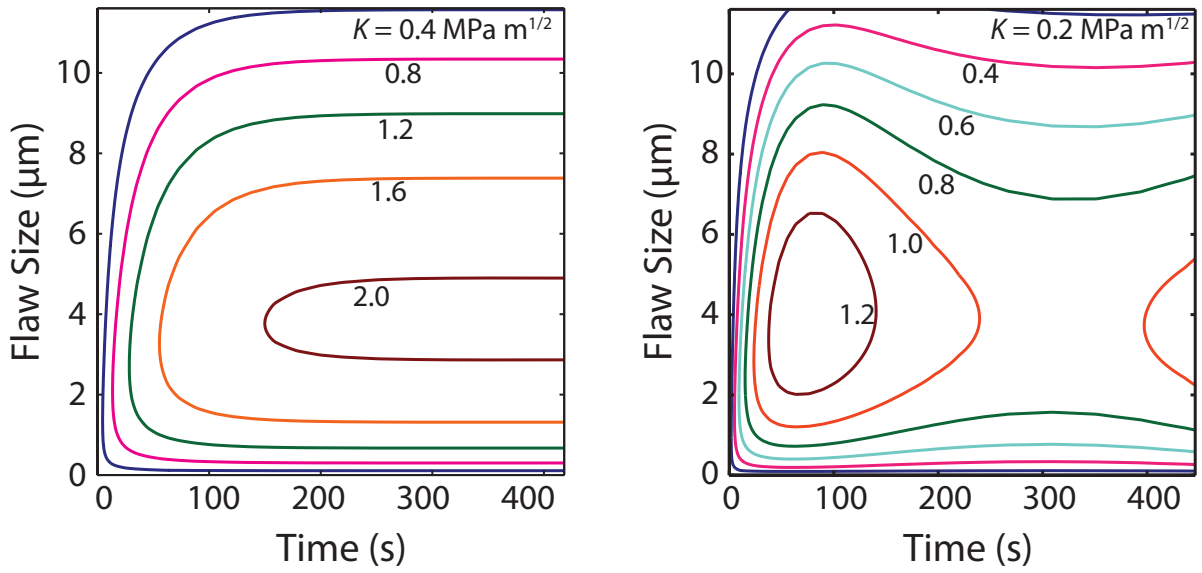

Figure 2-13: Contour maps of the stress-intensity factor as a function of crack length and time, $K_I(a,t)$, for 23 μm Nernstian particles with (a) no chemomechanical coupling parameter, $\hat{\theta} = 0$ and (b) with finite chemomechanical coupling $\hat{\theta} = 4.57$. The instantaneous stress-intensity factor–flaw size curves all have the shape shown in Figure 2-12, increasingl rapidly for small flaws, but quickly reaches a maximum. These calculations are for 5C galvanostatic charges, corresponding to a dimensionless current of $\hat{I} = 0.5$.

In each solution thermodynamic case, the time-varying stress-intensity factor distributions $K_I(a,t)$ have unique global maxima. These maxima place a lower bound on the combinations of particle size and C-Rate that can cause fracture. As an illustrative example, consider the Nernstian particle with no chemomechanical coupling. The curves in Figure 2-12, are instantaneous snapshots at the time of maximum stress-intensity factor for charging of a 23 μm particle at C-Rates of 5C (red), 2.5C (green), and 1C (blue) For the sake of a concrete discussion, assume that the fracture toughness is $K_{Ic} = 1$ MPa m$^{1/2}$, a reasonable

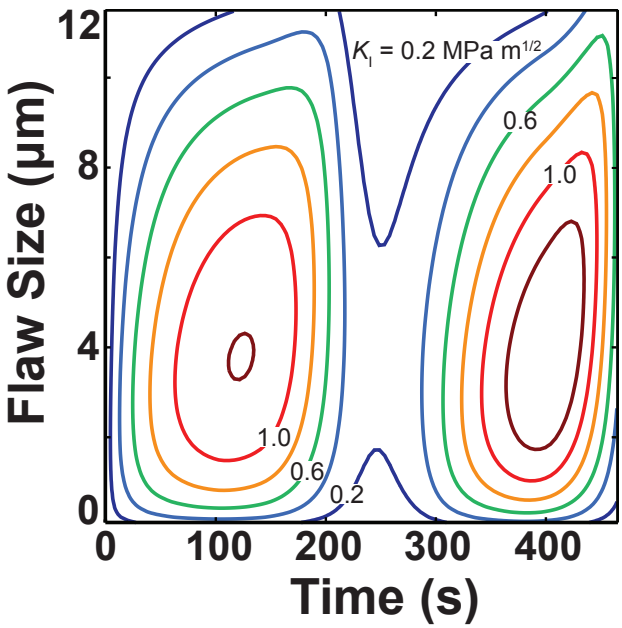

Figure 2-14: Contour plot of the stress-intensity factor as a function of crack length and time, $K(a,t)$, for a 23 μm "$Li_XMn_2O_4$-like" particle charged at a 5C rate, corresponding to a dimensionless current of $\hat{I} = 0.5$.

value for a brittle oxide material, which is illustrated by the dashed horizontal line in Figure 2-12. For the charges at 1C and 2.5C, there are no flaw sizes at which the stress-intensity factor exceeds the fracture toughness. For these conditions of particle size and C-Rate, it is not favorable for pre-existing cracks to grow. On the other hand, for the 5C charge, there is a range of flaw sizes over which the stress-intensity factor exceeds the fracture toughness; under this condition, fracture is possible.

Generalizing from this particular example, fracture only occurs if the maximum stress-intensity factor for a given particle size and C-Rate exceeds the material's inherent fracture toughness. Fracture will not occur if the maximum stress-intensity factor—maximized over time and flaw size—for a particular particle size and C-Rate does not exceed the fracture toughness.

2.7 Electrochemical Shock Maps

The fracture mechanics criterion for electrochemical shock is applied across a wide range of particle sizes and C-Rates using the dimensionless current and dimensionless stress-intensity factor. Figure 2-15 summarizes the maximum dimensionless stress-intensity factor, $\hat{K}_{\mathrm{I,max}}$ observed over a range of dimensionless currents, $\hat{I}$, for all three solution thermodynamic cases: a material with a Nernstian potential and no chemomechanical coupling $\hat{\theta} = 0$, a material with a Nernstian potential and finite chemomechanical coupling $\hat{\theta} = 4.57$, and a "$\mathrm{Li}_X\mathrm{Mn}_2\mathrm{O}_4$-like" material with the open-circuit voltage of $\mathrm{Li}_X\mathrm{Mn}_2\mathrm{O}_4$ and chemomechanical coupling $\hat{\theta} = 4.57$. In each case, the maximum dimensionless stress-intensity factor initially increases with dimensionless current across several orders of magnitude. For the Nernstian particles, sufficiently high current densities were investigated to observe a decreasing maximum dimensionless stress-intensity factor at very high dimensionless currents. The increase is easily understood as an overall increase of the diffusion-induced tangential stress as the current increases. The decrease can be explained as a "skin" effect: while the nominal maximum stresses may be large, the tensile stress field rapidly decays through a thin region near the particle surface. Therefore, only the smallest flaws—those with their crack-tip in the vicinity of the surface—are affected and the maximum stress-intensity factor is diminished. The decrease is expected also for the "$\mathrm{Li}_X\mathrm{Mn}_2\mathrm{O}_4$-like" particles, but was not observed in the range of parameter space presently explored. Interestingly, the chemomechanical coupling effect has a larger quantitative effect than including a measured, non-ideal open-circuit voltage, even though the open-circuit voltage appears to have a stronger effect on the composition-dependent chemical diffusivity.

Figure 2-16 shows the critical combinations of particle size and C-Rate that can cause fracture during galvanostatic charging. This figure—which we call an *electrochemical shock map*—gives a simple picture of fracture-safe and fracture likely conditions. This figure is

quantified for the Nernstian particle with chemomechanical coupling (the second solution thermodynamic case). As proxies for the unknown fracture toughness of $LiMn_2O_4$, we plot four values of fracture toughness representative of brittle materials: 0.1, 1, 3, and 5 $MPa{\cdot}m^{1/2}$. For comparison, the fracture toughness of soda-lime-silicate glass is $\sim$1 $MPa{\cdot}m^{1/2}$, the single crystal fracture toughness of magnesium aluminate spinel, $MgAl_2O_4$, is 1.2 – 1.9 $MPa{\cdot}m^{1/2}$ [93], and the fracture toughness of single-crystal sapphire (α-Al_2O_3) is 2.4 – 4.5 $MPa{\cdot}m^{1/2}$ [94]. The range of values for $MgAl_2O_4$ and α-Al_2O_3 is due to the crystallographic anisotropy of the single crystal fracture toughness in these materials. We anticipate that the fracture toughness of $LiMn_2O_4$ is within this range of values. Combinations of particle size and C-Rate lying below (and to the left of) the curve for the fracture toughness of $LiMn_2O_4$ will not induce fracture; conditions lying above (and to the right of) the curve may cause fracture, depending on the pre-existing flaw size.

The example case of a 23 μm particle charged at a 5C rate is indicated on the electrochemical shock map (Figure 2-16) as an orange point. The position of the star shows that this particle is subject to fracture if the fracture toughness is (a) 0.1 or (b) 1 $MPa{\cdot}m^{1/2}$ but will not fracture if the fracture toughness is (c) 3, or (d) 5 $MPa{\cdot}m^{1/2}$. The general trend of decreasing critical C-Rate with increasing particle size matches our intuition that large particles subjected to fast charges are most readily damaged.

2.8 Validity of Approximation for Phase-Transforming Materials

Models using a composition-dependent chemical diffusivity, have been suggested as approximate methods for modeling phase-transforming ion-intercalation electrode materials. These models are very similar to the "$Li_XMn_2O_4$-like" case considered in this chapter. Therefore, it is interesting to compare the predictions of the "$Li_XMn_2O_4$-like" case to experimental

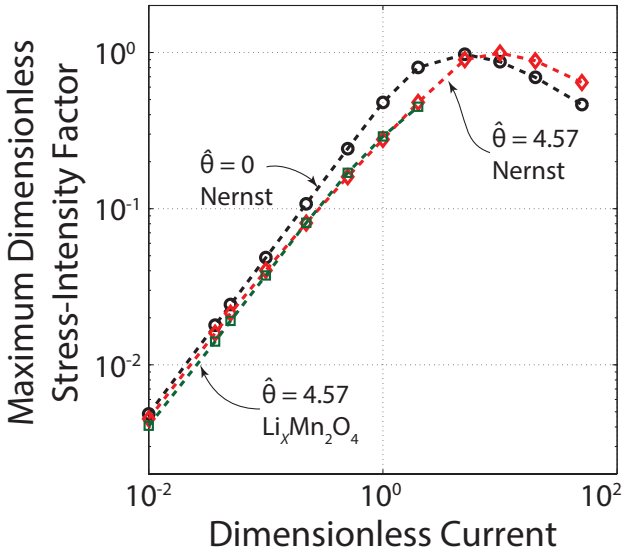

Figure 2-15: The maximum dimensionless stress-intensity factor $\hat{K}_{\mathrm{I}}$ increases with dimensionless current $\hat{I}$ for small to moderate values of $\hat{I}$, but decreases somewhat at very large values of $\hat{I}$. The turnover is attributed to a skin effect, where only shallow surface flaws are subjected to tensile diffusion-induced stresses. The red points represent computation results and the dashed black curve indicates a cubic spline interpolating function.

observations to assess whether such a model may be applied as a reasonable approximation for a phase-transforming ion-intercalation material.

Experimental observations presented Chapter 4 show that $\mathrm{Li}_X\mathrm{Mn}_2\mathrm{O}_4$ particles with sizes $\sim 2-5$ μm are subject to low C-Rate (C/50) electrochemical shock, which is attributed to two-phase coherency stresses. These experimental observations are supported by finite element analysis of two-phase $\mathrm{Li}_X\mathrm{Mn}_2\mathrm{O}_4$ particles, which are performed in the static (zero C-Rate) limit. Any approximate kinetic model for electrochemical shock in a phase-transforming ion-intercalation material must capture this essential behavior.

The "$\mathrm{Li}_X\mathrm{Mn}_2\mathrm{O}_4$-like" case considered in this chapter does not meet this essential criterion, as the particle size for electrochemical at a C/50 rate is nearly 100 μm. *Thus, this approximate method for treating solid-phase diffusion in phase-transforming electrodes does not give an accurate accounting of the mechanical response of individual particles.* Therefore, the results for the composition, elastic stress, and stress-intensity factor distributions should be

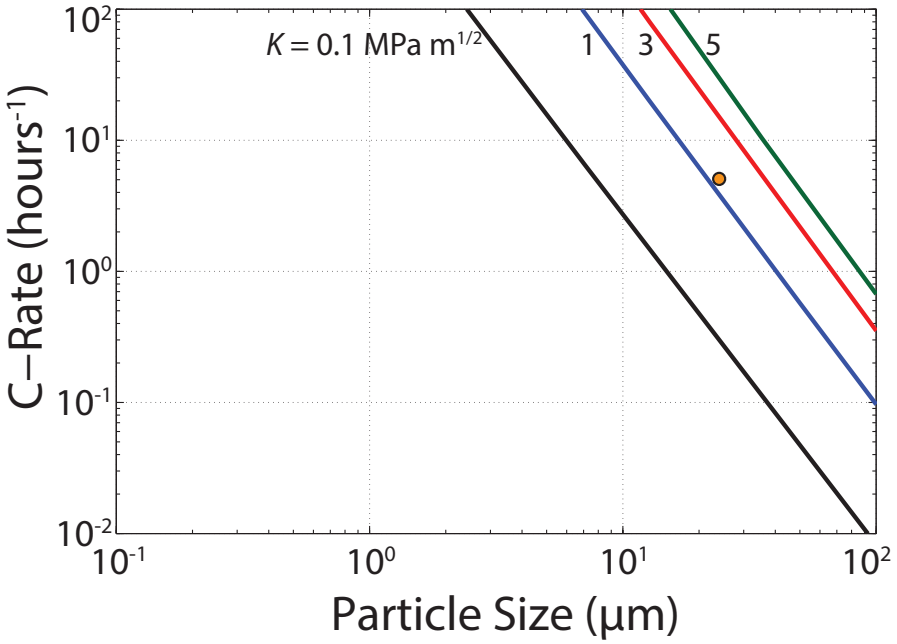

Figure 2-16: Electrochemical shock map for galvanostatic charging of a Nernstian particle with chemomechanical coupling $\hat{\theta} = 4.57$, plotted on logarithmic axes. Curves represent the onset of fracture for five representative values of the fracture toughness, K_{Ic}, of brittle materials: (a) 0.1 MPa·m$^{1/2}$ (b) 1 MPa·m$^{1/2}$ (c) 3 MPa·m$^{1/2}$ (d) 5 MPa·m$^{1/2}$. Above the curve representing each value of fracture toughness, fracture is possible. The orange point near the 1 MPa·m$^{1/2}$ line represents the example case of a 23 μm particle charged at a 5C rate.

treated as valid only for materials that form continuous solid-solutions with respect to lithium composition. An accurate description of the mechanical response of phase-transforming electrode particles during electrochemical cycling must explicitly treat the phase transformation. The present model for electrochemical cycling is revised and generalized in Chapter 5 to incorporate phase-transformations in ion-intercalation materials, including and especially real $Li_X Mn_2O_4$.

Principally, this model fails to accurately capture the two-phase coherency stresses because it does not produces phase-separation at low current densities. The composition inside of particles at is plotted against dimensionless radius at different times is shown for two different dimensionless currents in Figure 2-17. The left figure (a) shows a low dimensionless current $\hat{I} = 0.01$ and the right figure (b) shows a high dimensionless current $\hat{I} = 1$. In the low dimensionless current case, the composition is nearly uniform throughout the particle, showing no evidence of a phase-separating behavior when the average composition is in the two-phase region $0.5 \geq X \geq 0.25$. In the high dimensionless current case, there is something approximating a diffuse interface between a lithium-rich phase and a lithium-poor phase. However, the interface never becomes highly localized because there is no concentration gradient penalty. For conventional electrochemical modeling, the average and surface compositions must be accurately determined to match experimental observations. As described in this chapter, the stress distributions which drive electrochemical shock are sensitive to the whole composition profile.

2.9 Discussion

In summary, we have derived a fracture model to predict electrochemical shock using particle size and C-Rate as inputs. We used a theoretical framework to model electrochemical cycling of non-ideal, chemomechanically coupled materials, and applied this model to pre-

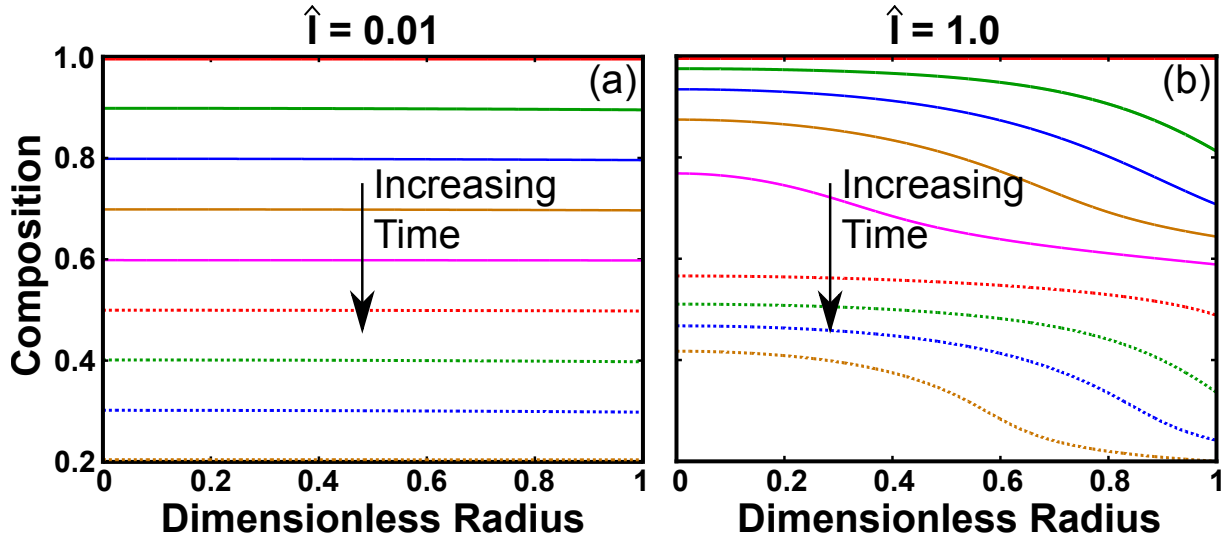

Figure 2-17: Comparison of the composition distribution inside of individual particles as a function of time for two different charging rates (dimensionless currents) (a) $\hat{I} = 0.01$ and (b) $\hat{I} = 1$.

dict coupled composition and stress profiles for individual spherical particles. Then, we use our fracture mechanics model to calculate the corresponding stress-intensity factor - flaw size relationships. The fracture mechanics model is general enough to be integrated with any model for diffusion-induced stress, including those of Garcìa *et al.* [61], Christensen and Newman [48, 47], or Cheng and Verbrugge [62, 49]. This integration would provide a fracture mechanics failure criterion for those stress models and could be used to extend the applicability of our model to include non-ideal solution thermodynamics, nonlinear partial molar volume, and phase transformations.

This fracture mechanics model could also be integrated into a porous electrode model to predict mechanical damage accumulation in composite battery electrodes. The C-Rate in Figure 2-16 refers to the local single particle C-Rate, not the homogenized macroscopic C-Rate describing a composite electrode. In a composite electrode, there may be spatial inhomogeneities in the current density, especially in the thickness direction. If we have a model for the current distribution of a porous composite electrode, this fracture model can be applied to predict fracture of individual active particles composing that electrode.

Integration of this model with a conventional porous electrode theory would mirror the approach of Christensen [65] and Renganathan [64].

While we have not incorporated the statistical nature of flaw size distributions, it will significantly impact the mechanical reliability of real electrode materials. Our model assumes the existence of a single largest pre-existing flaw in a given particle. Theories of reliability statistics in brittle materials assume that the probability of finding a "large" flaw scales rapidly with the volume of material. A model for the flaw distribution could be used when extending this model to real composite electrodes containing many individual active particles. Statistical approach to electrochemical shock from C-Rate-independent mechanisms given in Chapter 6, and model could be extended to include concentration-gradient effects.

2.10 Conclusions

Fracture mechanics predicts a critical C-Rate for fracture during galvanostatic charging, which decreases with increasing particle size. We show the critical combinations of C-Rate and particle size for the model system $Li_xMn_2O_4$ on an electrochemical shock map, which shows the division between fracture-safe and fracture-likely conditions. Electrochemical shock maps can be used as a material selection tool; as one simple example, a designer given a required C-Rate could identify mechanically durable electrode active materials and particle sizes on the map.

The highly non-uniform tangential stress profiles caused by galvanostatic charging produces a maximum stress-intensity factor for a given combination of C-Rate and particle size. In cases where the maximum stress-intensity factor is less than the fracture toughness of the material, fracture will not occur. In cases where the maximum stress-intensity factor exceeds the fracture toughness of the material, pre-existing cracks can grow.

The solution thermodynamics of ion-intercalation materials affect the magnitude of the

elastic stresses and stress-intensity factors developed in particles, and also qualitatively change the time-dependence of the stress and stress-intensity factor profiles. However, regardless of the solution thermodynamics, single phase ion-intercalation materials develop concentration-gradient stresses in proportion to the applied C-Rate, and are sensitive to C-Rate-dependent electrochemical shock. For phase-transforming ion-intercalation materials, an approximate model using a composition-dependent chemical diffusivity that incorporates the observed open-circuit voltage does not accurately describe electrochemical shock.

The dependence of stress-intensity factor on both particle size and galvanostatic charge rate suggests that electrochemical shock can be avoided by tailoring the microstructure and charging profiles of intercalation electrodes to minimize the diffusion-induced stress-intensity factor.

THIS PAGE INTENTIONALLY LEFT BLANK

Chapter 3

Anisotropy-Driven Grain Boundary Microfracture

Most models of electrochemical-mechanical coupling—including the analysis in Chapter 2—assume isotropic shape change with lithium composition, an isotropic and homogeneous particle microstructure, and isotropic linear elastic response. These assumptions are useful to identify important scalings, but rarely do real battery materials fit this idealized description. As the data collected in Tables 1.1 & 1.2 demonstrate, the Vegard coefficients accompanying (de)intercalation are often anisotropic, and may result in whole or in part from first-order phase-transformations. Moreover, depending on their synthesis, active particles can be single- or poly-crystalline. [95]

Experimentally, there have been numerous observations of electrochemical shock in polycrystalline particles of several different active materials, including $Li_{1+X}Mn_2O_4$,[96] $Li_XNi_{0.8}Co_{0.15}Al_{0.05}O_2$ (NCA), [29] and Li_XNiO_2; [97] all of these materials have anisotropic Vegard coefficients. In fact, as the data collected in Table 1.1 demonstrate, almost all technologically important Li-storage compounds have anisotropic Vegard coefficients. Li-storage compounds with ordered rocksalt, olivine, and tavorite structures all show signifi-

cant anisotropy. The exceptions are the cubic spinels, most notably $Li_{4+X}Ti_5O_{12}$ which has negligible dimensional change with varying Li composition. However, even the manganese oxide spinel $Li_XMn_2O_4$ undergoes an anisotropic cubic to tetragonal phase-transformation upon lithium insertion along the 3 V plateau ($1 \leq X \leq 2$). To understand and mitigate electrochemical shock in real battery electrodes, anisotropic Vegard coefficients must be considered.

The analogy between thermal shock and electrochemical shock provides useful expectations about electrochemical shock in anisotropic, polycrystalline materials. In thermal shock, anisotropic materials such as Fe_2TiO_5 undergo extensive microfracture [98, 99] at grain boundaries and junctions. Large stresses are generated at these microstructural features due to the incompatible shape changes in neighboring, crystallographically misoriented grains. However, thermal shock microfracture can be suppressed by careful control of the microstructure. Microfracture does not occur when all grains are smaller than a material-specific critical grain size; this critical grain size does not depend on the cooling rate. Above the critical grain size, thermal shock microfracture occurs when the material is subjected to a sufficiently large temperature change to drive crack growth.

Observations of electrochemical shock in Li-battery electrodes are consistent with this understanding of thermal shock microfracture: for example, the observations made by Itou, *et al.* who studied polycrystalline NCA particles with initial primary crystallite size of ∼0.5-1 μm and secondary particle size ∼8-10 μm. [29] These particles showed extensive fracture, concentrated at the grain boundaries, when cycled in 18650 cells against graphite negative electrodes. The full cell impedance growth up to 800 cycles was almost entirely due to impedance growth at the positive electrode, which in turn, was strongly correlated with the extent of fracture in the NCA particles. By limiting the state-of-charge change swing at the positive electrode, fracture and subsequent impedance growth was suppressed. This final observation suggests that there is a critical state-of-charge swing—analogous to the critical

temperature drop in thermal shock—for electrochemical shock microfracture.

The consonance between observations of electrochemical shock microfracture and thermal shock microfracture leads to the hypothessis that anisotropic Vegard coefficients cause the experimentally observed mechanical degradation of polycrystalline Li-storage materials. Further, the analogy implies that the existence of a critical primary crystallite size, below which electrochemical shock microfracture does not occur; this critical primary crystallite size should be independent of the electrochemical cycling rate (C-Rate), but should depend on the state-of-charge through which the active material is cycled.

The objective of this chapter is to demonstrate C-Rate independent electrochemical shock analogous to thermal shock microcracking with *in operando* acoustic emission experiments and micromechanical models, using Li_XCoO_2 as a model system. These results provide new microstructure design criteria and materials selection criteria for mechanically robust battery electrode materials.

This chapter is organized as follows. First, we revise and apply a micromechanical model originally due to Clarke, [100] which incorporates anisotropic Vegard coefficients, polycrystalline microstructures, and allows for first-order phase-transformations, thereby relaxing many of the assumptions made in the analysis of C-Rate-dependent electrochemical shock in isotropic spherical particles of Chapter 2. The analytical model is validated by comparison to finite element calculations of the elastic stress distributions and the strain-energy-release rate. Next, the results of *in operando* acoustic emission experiments performed with model electrodes of monolithic sintered Li_XCoO_2 are presented; these experimental results confirm C-Rate independent electrochemical shock during the first electrochemical cycle. Finally, the analytical microfracture model is applied to additional Li-storage compounds with anisotropic Vegard coefficients, explaining several observations of fracture in polycrystalline electrode particles.

First-order phase-transformations with misfit strains, such as in Li_XCoO_2, require a

separate analysis of fracture at the single crystallite level due to two-phase coherency stresses; this problem is studied in Chapter 4 and the analysis of Li_XCoO_2 is given in Section 4.2.2. An important conclusion from the analysis of Li_XCoO_2 is that two-phase coherency stresses will not drive fracture of two-phase Li_XCoO_2 crystallites smaller than $\sim$8 μm.

3.1 Grain Boundary Microfracture in Polycrystalline Ensembles

In thermal shock, it is well known that polycrystalline materials with anisotropic thermal expansion coefficients and/or phase-transformations with anisotropic transformation strains suffer from thermal shock microfracture. Numerous experimental and theoretical studies have addressed this problem, and there is consensus that microfracture can be suppressed by processing the material in a manner that keeps all grain sizes below a material-specific critical grain size. [101, 102, 103, 100, 104, 105, 98, 106, 107, 108] Here, we revise and apply a model originally due to Clarke to describe electrochemical shock microfracture resulting from anisotropic Vegard strains in polycrystalline Li-storage materials. [100]

While Clarke's model is described in detail in the original publication, we summarize here the essential features of this two-dimensional model. The central entity is an ensemble of four grains in which each grain undergoes an anisotropic stress-free transformation strain as depicted in Figure 3-1. The ensemble is embedded in an infinite isotropic linear elastic matrix. The four-grain ensemble is chosen because it captures the essential physics of collective, misaligned anisotropic shape changes in neighboring grains in a polycrystalline sample, and can be solved analytically. Each grain is square with an edge length l, and there is a pre-existing crack centered at the quadruple junction with an initial length $2a$. The four grains are mutually oriented in a worst-case configuration, so that the transformation strains are most damaging to the pre-existing crack.

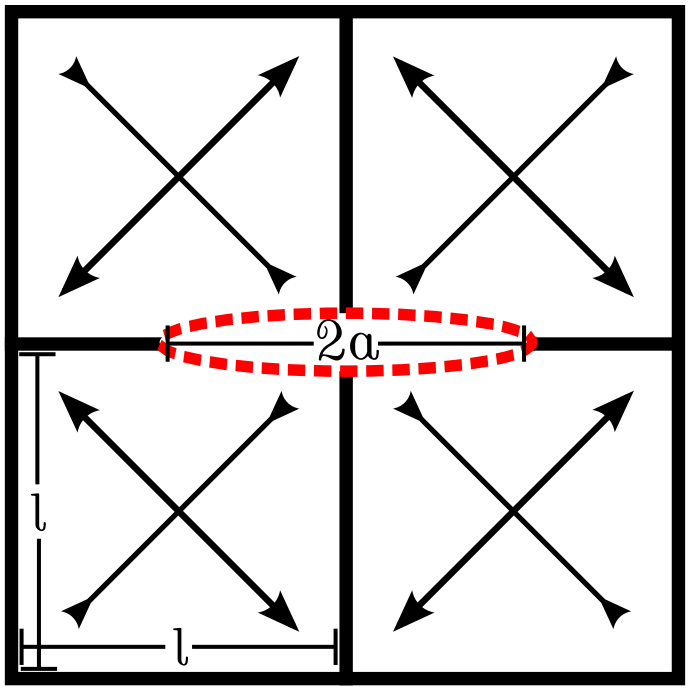

Figure 3-1: Four-grain ensemble used for grain boundary microfracture model. The arrows in each grain indicate the principal axes of the crystallographically anisotropic Vegard strain. Grain edges have length l and the pre-existing crack at the quadruple junction has length $2a$. The four-grain ensemble is embedded in an infinite isotropic linear elastic matrix.

The quantity of interest is the critical grain size, below which it is not favorable for the pre-existing crack to grow, irrespective of its initial size. This problem is formulated in the framework of linear-elastic fracture mechanics, [87] using the stress-intensity factor K_{I} as a measure of the crack growth driving force. When the stress-intensity factor for all flaw sizes is below the fracture toughness K_{IC}, no pre-existing cracks can grow. We estimate the critical grain size at which fracture becomes possible by computing the stress-intensity factor as a function of flaw size and finding the grain size at which the maximum stress-intensity factor is equal to the fracture toughness. To complete this fracture mechanics analysis, we first calculate the elastic stress distribution $\sigma_{nn}(x)$ acting across the horizontal grain boundary. Then, the stress-intensity factor as a function of flaw size is calculated using a standard superposition integral.

$$K_{\mathrm{I}} = \frac{1}{\sqrt{\pi a}} \int_{-a}^{a} \sigma_{nn}(x) \sqrt{\frac{a+x}{a-x}} \mathrm{d}x \tag{3.1}$$

To calculate the stress distribution in the crack-free four-grain ensemble, the problem is treated by the method of Eshelby [109] with a series of virtual cutting and welding operations. The following steps are taken to calculate the stress distribution: first, the four-grain ensemble is cut from the surrounding matrix and allowed to undergo the stress-free transformation strain; then, stresses are applied to the ensemble grains to restore them to their original shape; finally, the ensemble is re-inserted to the matrix and matrix-relaxation forces are applied at the boundary to ensure continuity of the stresses. The matrix relaxation forces are calculated using as a Green's function the stress field due to a point load acting at the surface of a semi-infinite isotropic half space; these expressions are given in Timoshenko and Goodier [86] and are repeated here as Equations 3.2–3.4.

$$\sigma_{xx}(x,y) = \frac{P\cos\theta}{4\pi r}\left[(1-\nu) - 2(1+\nu)\sin^2\theta\right] \tag{3.2}$$

$$\sigma_{yy}(x,y) = \frac{P\cos\theta}{4\pi r}\left[-(3+\nu) + 2(1+\nu)\sin^2\theta\right] \tag{3.3}$$

$$\sigma_{xy}(x,y) = -\frac{P\sin\theta}{4\pi r}\left[(1-\nu) + 2(1+\nu)\cos^2\theta\right] \tag{3.4}$$

The anisotropic transformation strain is decomposed into shear (ϵ_S) and volumetric (ϵ_V) components, which are treated separately and then superposed to give the full stress distribution. To reduce the full three dimensional transformation strain to the two dimensional model we take the two dimensional volumetric strain ϵ_V equal to one half the three dimensional volume change and the two-dimensional shear strain ϵ_S equal to one half the difference between the maximum and minimum linear strains. The resulting stress distribution acting across the horizontal grain boundaries is given as

$$\sigma_{nn} = \frac{E}{4\pi}\left(\frac{\epsilon_S}{1+\nu} g_S(x) + \frac{\epsilon_V}{1-\nu} g_V(x)\right) \tag{3.5}$$

where $g_S(x)$ and $g_V(x)$ are dimensionless functions that describe the shape of the stress distributions due to the shear and volumetric components of the transformation strain. The parameter x is the distance from the quadruple junction, traversed along the horizontal grain boundary. However, the printed expression for the dimensionless function $g_S(x)$ in Clarke's original paper lacks the requisite symmetry under $x \to -x$. We have re-derived the dimensionless function $g_S(x)$, and the resulting expression is given in Equation **??**. An important check of the correctness of our expression for $g_S(x)$ is that the present expression is symmetric for $x \to -x$ as required by the symmetry of the four-grain ensemble. The volumetric strain contribution to the total elastic stress distribution is described by the dimensionless function $g_V(x)$, which we find to be identical to the original expression; this is given in Equation 3.7. These functions $g_S(x)$ and $g_V(x)$ are plotted for Poisson's ratios of $\nu = 0,\ 0.25,$ and 0.5 in Figures 3-3 and 3-2. The dilatational component $g_V(x)$ provides a compressive, stabilizing stress for a positive dilatational strain ϵ_V and a tensile stress for a negative dilatational strain. The magnitude of the dilatational component decreases with increasing Poisson's ratio. The shear component $g_S(x)$ is heterogeneous, with singularities as $x \to 0$ and $x \to l$. As the shear component ϵ_S is defined to be non-negative, the four-grain ensemble always expriences a singular tensile stress at the quadruple junction. This singular tensile stress distribution provides the driving force for fracture. Near the edge of the ensemble, there is a compensating singularity in the compressive direction.

$$
\begin{aligned}
g_S(x) =& (1-\nu)\left[\ln(l^2+(l-x)^2) - 2\ln(x^2+l^2)\right. \\
&\left. + \ln(l^2+(l+x)^2) + 4\ln|x| - 2\ln|x-l| - 2\ln|x+l|\right] \\
& 2(1+\nu)\left[\frac{2l^2}{l^2+(l-x)^2} - \frac{4l^2}{l^2+x^2} + \frac{2l^2}{l^2+(l+x)^2}\right] + \\
& (3+\nu)\left[2\ln(l^2+x^2) - 2\ln(x^2) - \ln(l^2+(l-x)^2)\right. \\
& \left. - \ln(l^2+(l+x)^2) + \ln((l-x)^2) + \ln((l+x)^2)\right]
\end{aligned}
\tag{3.6}
$$

$$
\begin{aligned}
g_V(x) =& 4\nu \left[\arctan\left(\frac{l}{l+x}\right) + \arctan\left(\frac{l}{l-x}\right) \right] \\
& - 4\pi + 4 \left[\arctan\left(\frac{l+x}{l}\right) + \arctan\left(\frac{l-x}{l}\right) \right]
\end{aligned}
\tag{3.7}
$$

We now provide quantitative estimates of the state-of-charge dependent critical primary crystallite size for grain boundary microfracture in our selected model system of polycrystalline Li_XCoO_2. To isolate the effect of collective, misaligned anisotropic shape changes in neighboring grains, we choose several single-phase compositions $X = 0.93$, 0.74, and 0.50 for analysis. We use composition-dependent anisotropic Vegard coefficients determined from state-of-charge dependent lattice parameter data, [7] and assume that the polycrystal is initially stress-free in the fully lithiated (discharged) state, *i.e.* $X = 1$. The two-dimensional shear and volumetric strains for partially delithiated states are calculated with reference to the fully lithiated state. The two-dimensional volumetric ϵ_V and shear ϵ_V strains so defined are given for each composition in Table 3.1 At each selected state-of-charge, we compute the elastic stress distribution and the resulting stress-intensity factor–flaw size relationship. We then use the maximum stress-intensity factor to estimate the critical primary crystallite size below which the crack will not grow irrespective of its initial size.

To model Li_XCoO_2, we use isotropic linear elastic properties $E = 174$ GPa and $\nu = 0.3$, as determined from nanoindentation measurements [79]. These elastic properties are in good agreement with the bulk modulus $B = 149$ GPa measured by high pressure x-ray diffraction experiments [110] and corroborated by density functional theory calculations. We anticipate that the elastic properties of $LiCoO_2$ are anisotropic, but our previous experimental measurements [79] show that the only available elastic tensor data for $LiCoO_2$ [111] greatly overestimates the average elastic stiffness. We use a plane strain fracture toughness $K_{IC} = 1$ MPa$\cdot$m$^{1/2}$ which is intermediate between the median and mean fracture toughness measured in individual grains of dense polycrystalline $LiCoO_2$. [79]

The critical primary crystallite size estimates are performed in terms of the the dimen-

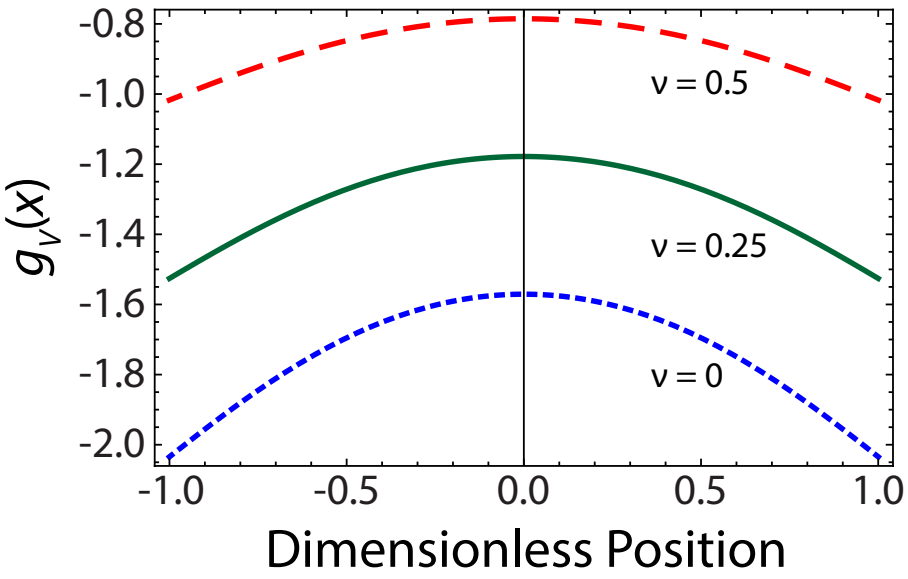

Figure 3-2: Dimensionless function $g_V(x)$ which characterizes the shape of the stress contribution due to the dilitational component of the shape change, plotted for ν of 0, 0.25, and 0.5.

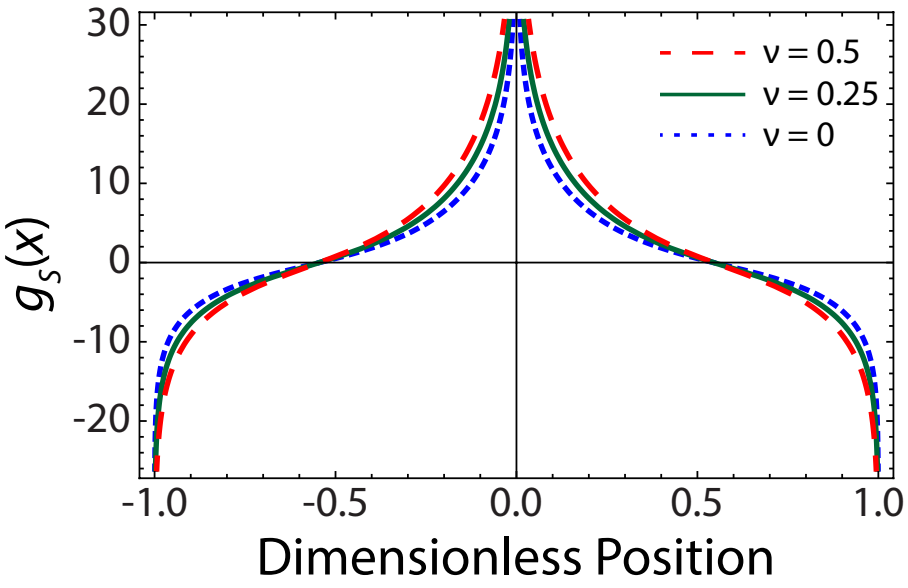

Figure 3-3: Dimensionless function $g_S(x)$ which characterizes the shape of the stress contribution due to the shear component of the shape change, plotted for ν of 0, 0.25, and 0.5.

sionless stress-intensity factor, as outlined in Section 1.4. Here, the two-dimensional shear strain for a composition $X = 0.50$ is used as the characteristic strain for all compositions and the dimenionless-stress intensity factor is defined as

$$\hat{K} = \frac{K}{E\epsilon_S\sqrt{l}} \tag{3.8}$$

For each composition, the dimensionless-stress intensity factor has a unique maximum $K_{\max}$, which defines the critical primary crystallite size, below which fracture is not favorable

$$l_{\text{crit}} = \left(\frac{K_{\text{Ic}}}{\hat{K}_{\max}E\epsilon_S}\right)^2 \tag{3.9}$$

Figure 3-4 shows the normal stress distribution along the horizontal grain boundary, computed for Li_XCoO_2 with compositions $X = 0.93$, 0.74, and 0.50. The severity of the elastic stress distribution grows as the lithium composition decreases (this corresponds to increasing state-of-charge). Figure 3-5 shows the dimenionless stress-intensity factor–flaw size curves corresponding to the same compositions. Each curve has a unique maximum value, which increases as the lithium composition decreases.

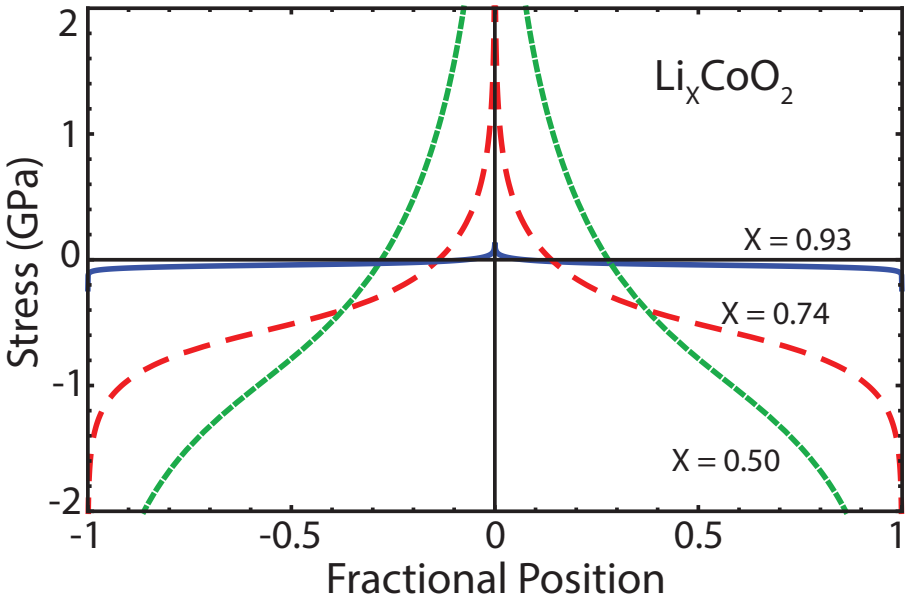

Figure 3-4: Analytical stress distributions for Li_XCoO_2 for $X = 0.93, 0.74, 0.50$.

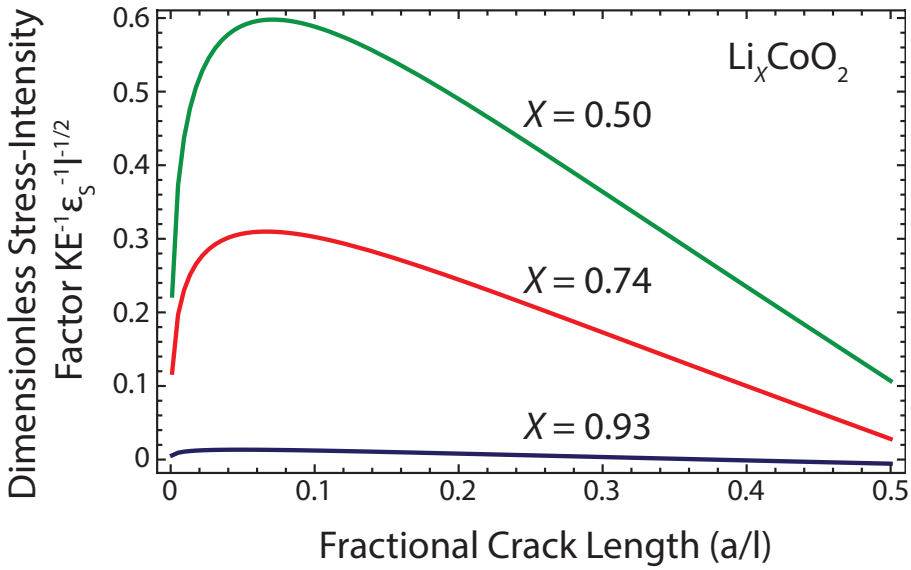

Figure 3-5: Dimensionless stress-intensity factors for $\mathrm{Li}_X\mathrm{CoO}_2$ for $X = 0.93, 0.74, 0.50$.

The critical primary crystallite sizes resulting from this analysis are given for the selected states-of-charge in Table 3.1; we have also listed the corresponding two-dimensional shear (ϵ_S) and volumetric (ϵ_V) strains, and the maximum dimensionless stress-intensity factor $\hat{K}_{\max}$ for each state-of-charge. As the $\mathrm{Li}_X\mathrm{CoO}_2$ polycrystal is initially delithiated, the shape change of individual grains is small and the critical primary crystallite size is large, 844 μm. After half of the lithium is removed, *i.e.* $X = 0.50$ (the conventional limit for cycling of LiCoO_2), the critical primary crystallite size is orders of magnitude smaller, now only 0.42 μm. Thus, to avoid grain boundary microfracture when cycling over the composition range $0.50 \leq X \leq 1$, polycrystalline LiCoO_2 particles should have primary crystallite size less than 0.42 μm. For narrower state-of-charge windows, larger primary crystallites can survive without electrochemical shock by grain boundary microfracture. Note that the critical primary crystallite sizes for compositions $X = 0.74$ and 0.93 differ from those previously reported [45]; in the previous analysis, a constant flaw size, corresponding to the most damaging flaw size for $X = 0.50$ was used at all compositions. Here, the unique maximum for each composition is used.

Table 3.1: Critical primary crystallite size for microfracture in polycrystalline Li_XCoO_2 at different states of charge.

X in Li_XCoO_2	ϵ_S [%]	ϵ_V [%]	$\hat{K}_{\max}$ [-]	Critical Primary Crystallite Size [μm]
0.93	0.020	0.045	0.0134	844
0.74	0.395	0.575	0.309	1.58
0.50	1.475	0.950	0.598	0.42

3.2 Finite Element Validation of Analytical Model

The analytical model is validated by comparison to finite element calculations. First, the analytical stress distributions are compared to numerical results from two-dimensional finite element calculations. Then, the critical primary crystallite size estimate for composition $X = 0.50$ is compared to an explicit calculation of the strain-energy release rate.

All of these finite element calculations are performed usig OOF2. The elastic stress calculations are performed under plane strain conditions, and the strain energy-release rate estimates are performed for both plane strain and plane stress conditions.

Figure 3-6 shows a schematic depiction of the unit cell modeled in the finite element analysis. The two mirror symmetries in the four-grain ensemble are used to reduce the computational domain of the problem. The transforming square grain of size L is embedded in an isotoropic elastic matrix which is four times longer in each direction. The mirror symmetries are applied along the left and bottom boundaries by imposing zero-displacement boundary conditions. The right and top boundaries are allowed to be traction-free.

Figure 3-7 compares the analytical and numerical stress distributions for compositions $X = 0.93$, 0.74, and 0.50. The analytical and numerical results are in excellent agreement, and the analytical model captures the singular tensile stress near the quadruple junction. The analytical model seems to underestimate the compressive stress singularity as near the end of the grain, especially for composition $X = 0.50$, but at this spatial position, it will not

affect the stress-intensity factor estimates.

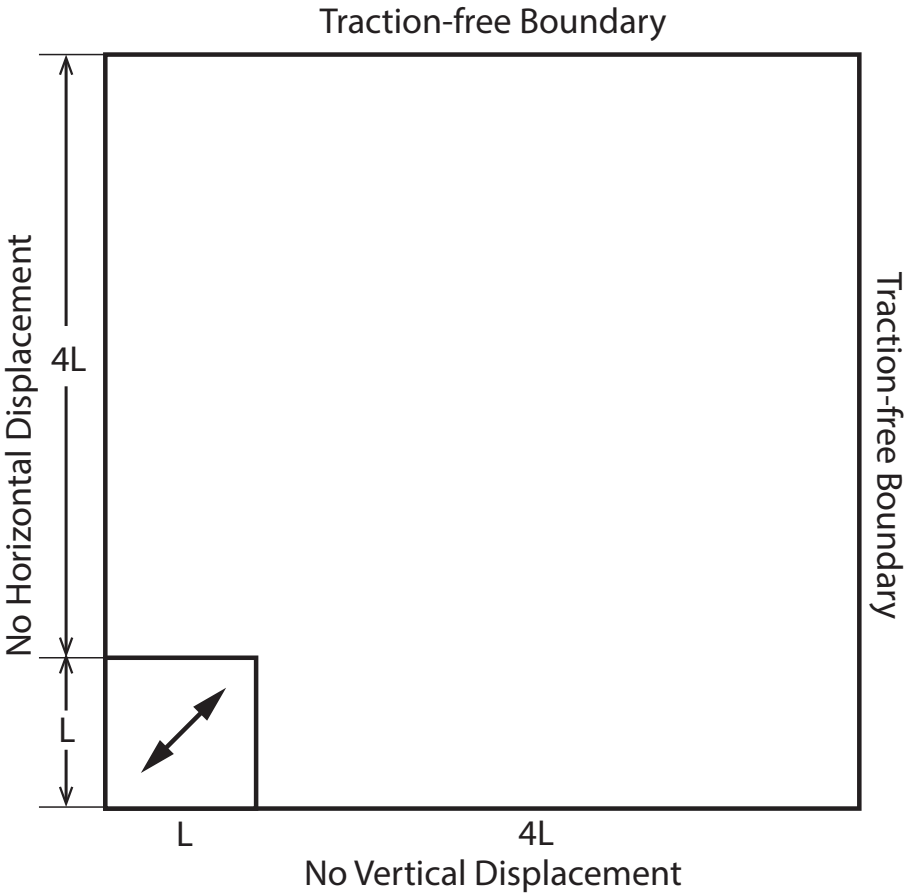

Figure 3-6: Schematic depiction of the FEM model used to validate analytical Clarke model.

The critical primary crystallite size estimates obtained using the analytical model are approximate because the the stress-intensity factor is estimated by a superposition method, which relies on the stress distribution computed in the absence of a crack. The presence of a crack provides additional compatibility, which reduces the crack-growth driving force compared to the superposition method estimtes. To understand the role of the added compatibility, we estimate the strain-energy-release rate using explicit finite element calculations. These calculations allow full relaxation of the crack-face displacements. The finite element analysis is formulated in the equivalent framework of Griffith theory. [87] The crack growth

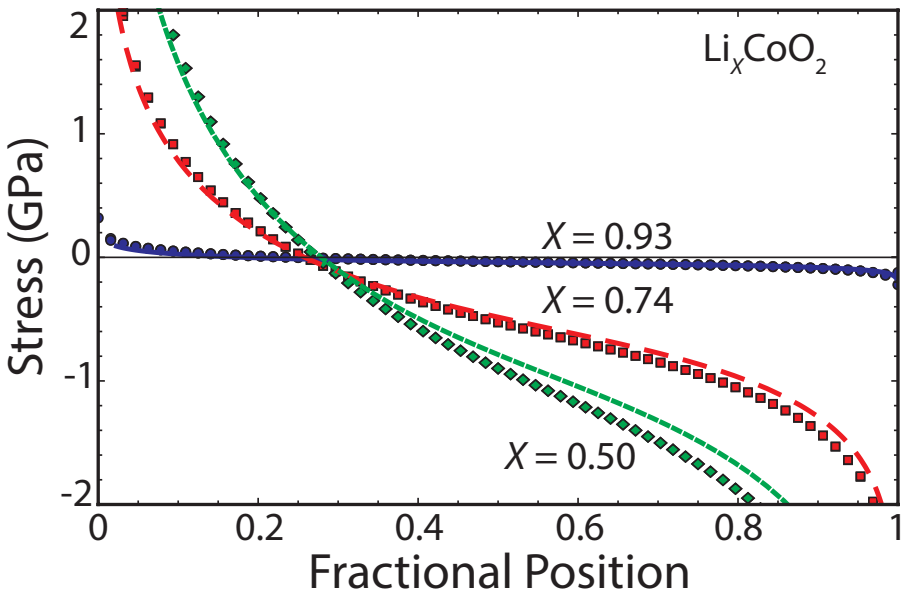

Figure 3-7: Comparison of FEM and analytical results for Clarke model applied to Li_XCoO_2 for $X = 0.93, 0.74, 0.50$.

driving force is specified as a strain-energy-release rate, $\mathcal{G} = -\frac{\partial U_E}{\partial a}$, where U_E is the elastic strain energy and a is the crack length, and crack growth is resisted by the increase in surface energy.

As described in Section 1.4, the strain-energy release rate can expressed as

$$\mathcal{G} = Z\left(\frac{a}{l}\right) E\epsilon_S^2 l \tag{3.10}$$

where Z is the dimensionless strain energy release rate, and the two-dimensional shear strain, ϵ_S at composition $X = 0.50$ is used as the characteristic strain. To estimate the strain-energy release rate, cracks of length $\frac{a}{l} = 0.02$, 0.05, 0.075, 0.1, 0.125, 0.15, 0.2, 0.25, 0.3, 0.35, and 0.4 are introduced into the finite element model. Traction-free boundary conditions are applied along the crack faces to allow relaxation of the crack-face displacements. The finite element meshes are refined more densely near the crack tip, with the smallest elements near the crack tip $\sim 10^{-5}$ times the crack length. The elastic boundary value problem is solved in OOF2 and the strain energy density is computed. Figure 3-8 shows the two-dimensional strain energy densities U_E computed for cracks of differing lengths under both plane strain

and plane stress conditions. The points are the computed data and the curves are B-splines fit to the respective data sets.

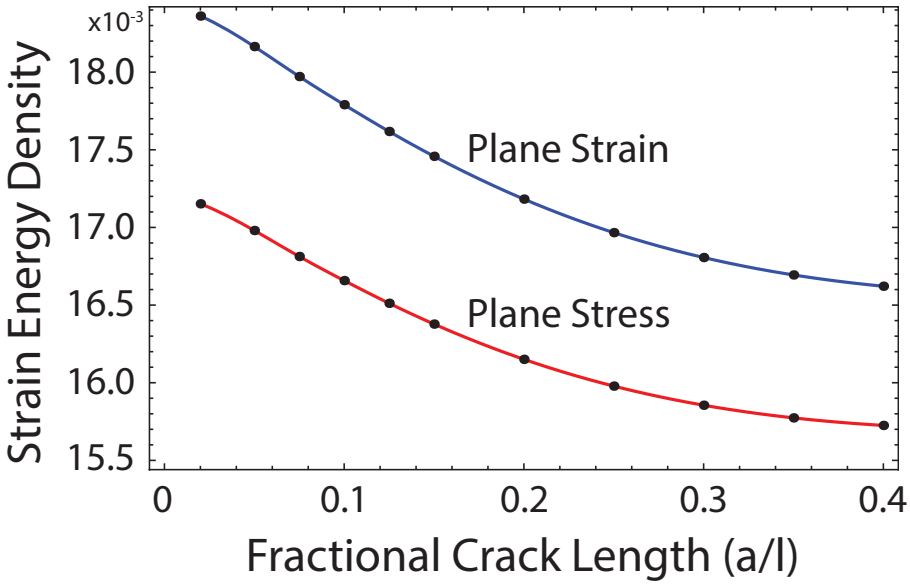

Figure 3-8: Explicit FEM calculations of strain energy density U_E for different fractional crack lengths a/l in Li_XCoO_2 with $X = 0.50$ showing actual computed points and the cubic spline interpolants. Both plane stress and plane strain shown.

Figure 3-9 shows the dimensionless strain energy release rate $Z\left(\frac{a}{l}\right)$ estimated from the finite element calculations. The dimensionless strain-energy release rates are estimated from the derivatives of the B-spline interpolations of the strain energy densities. For Li_XCoO_2 with $X = 0.50$, under plane strain conditions, the dimensionless strain energy release rate $Z\left(\frac{a}{l}\right)$ takes a maximum value of $Z_{\max} = 0.206$. To estimate the critical primary crystallite size, a critical strain-energy-release rate equivalent to the fracture toughness is used; the value of this effective surface energy is given by the standard plane strain relationship $\mathcal{G}_{\mathrm{C}} = \frac{(1-\nu^2)K_{\mathrm{IC}}^2}{E}$ and the numerical value is $\mathcal{G}_{\mathrm{c}} = 5.2$ J/m^2. The critical primary crystallite size is given as

$$l_{\mathrm{crit}} = \frac{\mathcal{G}_{\mathrm{c}}}{Z_{\max} E \epsilon_S^2} \tag{3.11}$$

These finite element calculations give a critical primary crystallite size of $l_{\mathrm{crit}} = 0.67$ μm for the composition $X = 0.50$, which differs from the analytical result by only a factor of 1.6.

As expected, the superposition solution overestimates the stress-intensity factor, as it does not allow for additional compatibility provided by the crack. This comparison confirms that the analytical model gives reasonable results, and as it is more readily applied to a variety of materials, may be used in place of explicit strain-energy-release rate calculations.

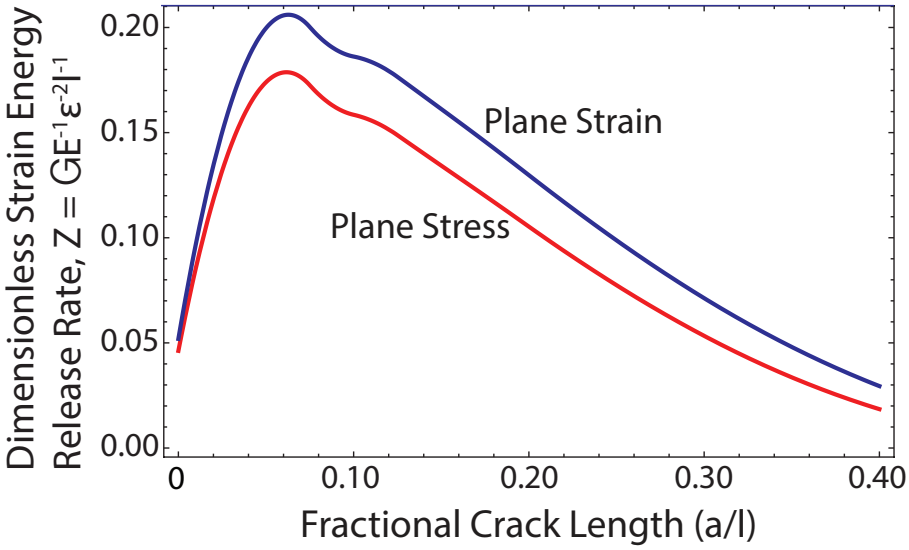

Figure 3-9: Dimensionless strain energy release rates estimated from explicit FEM calculations for different fractional crack lengths a/l in Li_XCoO_2 with $X = 0.50$ showing both plane stress and plane strain.

3.3 Acoustic Emission Experiments

To experimentally assess the hypothesized C-Rate independent electrochemical shock of polycrystalline materials with anisotropic Vegard coefficients, we performed *in-situ* acoustic emission experiments during low C-Rate cycling of monolithic sintered $LiCoO_2$ electrodes. Acoustic emission has previously been used to study fracture in lithium battery materials, including conversion-type materials, [112] silicon anodes, [113] and electrolytic MnO_2; [33, 114, 34] acoustic emission methods have also been used to study metal-hydride battery electrodes. [115] These monolithic sintered electrodes are single continuous polycrystals; which may be considered the infinite size limit of a polycrystalline particle. $LiCoO_2$ is an

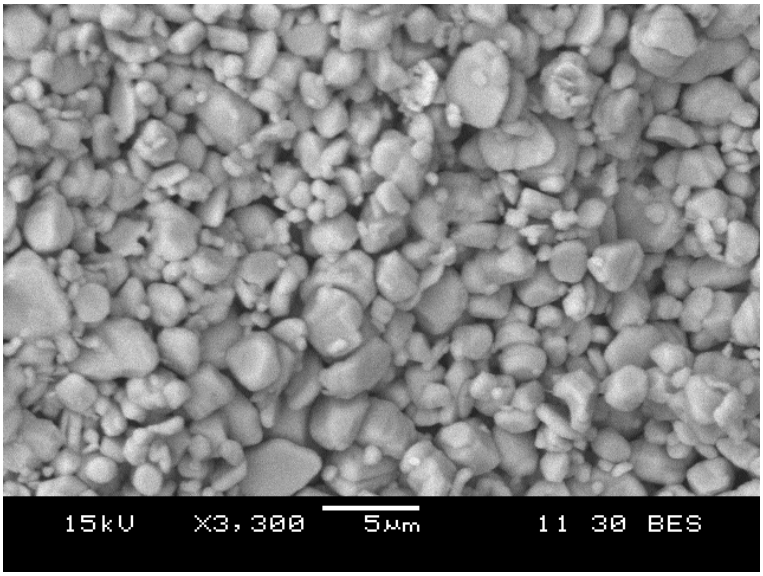

Figure 3-10: Backscatter electron micrograph of a fracture surface in a sintered $LiCoO_2$ electrode, prepared identically to those used for *in-situ* acoustic emission experiments, showing typical grain size of ∼1-3 μm.

ideal model system for these experiments because the elastic properties and anisotropy of the Vegard coefficients of $LiCoO_2$ closely approximate those of $Li_XNi_{0.8}Co_{0.15}Al_{0.05}O_2$ (NCA) and $LiNi_{1/3}Mn_{1/3}Co_{1/3}O_2$ (NMC) which are of practical interest as second generation cathode materials. As demonstrated previously by Lai, *et al.*, [116] monolithic $LiCoO_2$ electrodes can be cycled extensively at moderate rates. This is due in part to the excellent electronic conductivity (∼0.1-1 S cm^{-1} [117]) of partially delithiated $LiCoO_2$ which ensures that the polarization from solid phase electronic conduction is negligibly small ($\leq$ 1 mV) for the present experiments. The microstructure of a typical sintered electrode is shown along a fracture surface in Figure 3-10, revealing a typical grain size of 2-5 μm, consistent with Lai, *et al.* [116]

First, we study the acoustic emission during the first few cycles (three cycles at C/15 CC-CV to 4.4 V vs. Li metal) of a monolithic sintered $LiCoO_2$ electrode as shown in Figure 3-11. This slow cycling rate does not induce large solid phase concentration gradients, and therefore we do not expect C-Rate sensitive electrochemical shock mechanisms are active. The cell

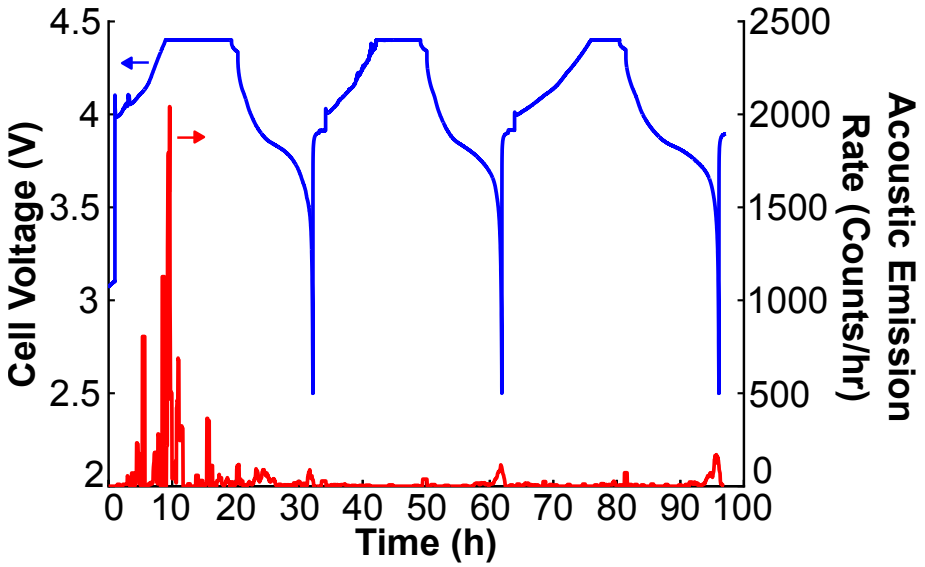

Figure 3-11: Cell voltage (blue, left axis) and acoustic emission rate (red, right axis) measured during first three cycles of a $LiCoO_2$ sintered electrode. Acoustic emission events are highly concentrated in the first charge cycle. The cell was charged with a constant current-constant voltage (CC-CV) protocol at a C/15 rate to 4.4V with a constant voltage hold until the current fell below C/50.

voltage (upper curve) is plotted in against the left axis and the rate of acoustic emission in counts per hour (lower curve) is plotted against the right hand axis; the horizontal axis is time in hours. We observe that the most pronounced acoustic emission is concentrated in the first charge cycle and that the large bursts of acoustic emission occur in the middle of the first charge cycle rather than at the beginning or end of charging. Smaller bursts of acoustic emission occur at the end of each discharge cycle; we have not yet identified the source of this recurring event, but we speculate that it may be related to the large polarization at this point in the cycle.

To assess if the polycrystalline character of our continuous sintered electrode is responsible for the observed acoustic emission behavior, we performed control experiments with composite electrodes. The high areal specific capacity of our sintered electrodes (∼30 mAh cm^{-1}) precludes direct comparison against conventional cast electrodes, so we prepared composite pellet electrodes with identical thickness and comparable areal capacity (∼27 mAh

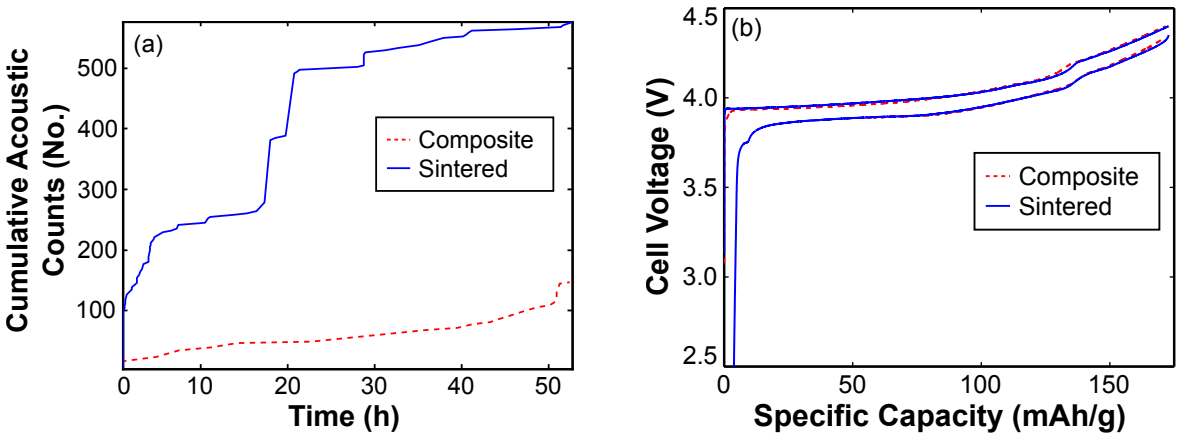

Figure 3-12: (a) Comparison of cumulative acoustic counts from sintered and thick composite pellet $LiCoO_2$ electrodes during the first charge at a C/50 (50 h) rate and (b) electrochemical voltage-capacity curves for same electrodes. The sintered electrode shows 5 times as many cumulative acoustic counts, despite the almost perfectly overlapping voltage curves.

cm^{-1}).

Figure 3-12(a) compares the cumulative acoustic emission counts measured during the first C/50 charge of a monolithic sintered $LiCoO_2$ electrode and a thick composite $LiCoO_2$ electrode. The respective voltage-capacity curves are shown in Figure 3-12(b) and are almost perfectly overlapping. This measured acoustic emission from the sintered electrode shows that the first cycle fracture events observed at C/15 persist to the extremely slow rate of C/50. The role of grain boundaries as a key source of acoustic emission events in the sintered electrode is confirmed by the five times difference in cumulative acoustic emission counts between the sintered and composite electrodes. The overlapping voltage-capacity curves suggest that the difference in acoustic emission is not due to a difference in the electrochemical behavior of the two electrodes.

These *in-situ* acoustic emission results demonstrate that there is C-Rate independent electrochemical shock in polycrystalline $LiCoO_2$. As shown in Section 4.2.2 of the next chapter, the critical size for two-phase coherency fracture of an individual Li_XCoO_2 crystallite is NN μm. As the typical grain size in our sintered $LiCoO_2$ electrode is 2-5 μm, this is clearly below the critical grain size for intragranular fracture due to coherency stresses, but above

the critical grain size for grain boundary microfracture. The conclusion that intragranular coherency stress fracture is not active in our monolithic sintered electrodes is consistent with observations by Clemencon, *et al.*, who studied ∼3-5 μm diameter Li_XCoO_2 single particles using in-situ atomic force microscopy. [118] $LiCoO_2$ particles charged up to 4.3 V vs. Li-metal did not show any obvious signs of fracture despite cycling through the two-phase region, as evidenced by the close agreement of the sample height change with literature values for the *c*-axis lattice parameter change.

3.4 Application to Other Materials Systems

The present acoustic emission experiments and micromechanical analysis demonstrate that polycrystalline Li_XCoO_2 fractures, independent of C-Rate, due to its anisotropic Vegard coefficients. We now explain related observations in the literature for other polycrystalline materials with anisotropic Vegard coefficients.

First, we apply the microfracture model to $Li_{1+X}Mn_2O_4$, cycled on the 3V plateau, where the material undergoes a first-order phase-transformation from cubic $LiMn_2O_4$ to tetragonal $Li_2Mn_2O_4$. It is well known that the large and anisotropic shape change limits the reversibility and cycle life of this system. From the energy-volume data of Van der Ven, *et al.*, [**?**] we estimate the bulk modulus of $Li_2Mn_2O_4$ as $B = 160$ GPa; assuming a typical value for Poisson's ratio $\nu = 0.3$, this gives a Young's modulus $E = 192$ GPa. Using these elastic properties and the Vegard coefficients listed in Table 1.1, we estimate the critical primary crystallite size is 10.8 nm. This very small critical primary crystallite size is consistent with observations of fractured polycrystalline $Li_{1+X}Mn_2O_4$ with crystallite sizes $\geq$ 20 nm. [96] While it is possible that $Li_{1+X}Mn_2O_4$ cycled along the 3 V plateau can partially accommodate the Vegard strain by formation of ferroelastic domains, this has only been directly observed when starting from an orthorhombic or monoclinic $LiMnO_2$

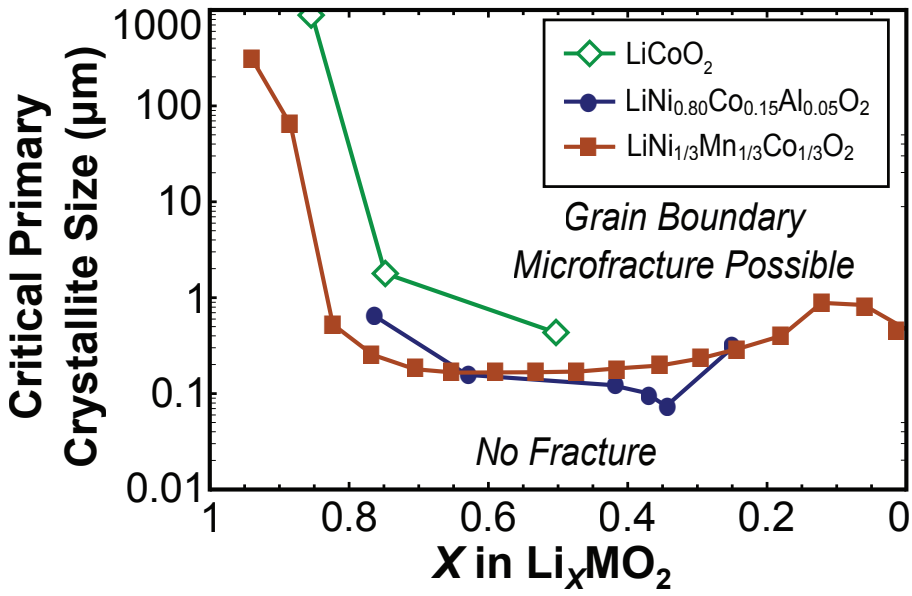

Figure 3-13: State-of-charge dependent critical primary crystallite size for C-Rate independent grain boundary microfracture of polycrystalline particles of selected LiMO$_2$ compounds. For cycling to a given state of charge, if the actual primary crystallite size exceeds the critical value, grain boundary fracture is possible.

starting material, which first transforms to the cubic spinel structure, forming nanoscale (10 nm) anti-phase domains which likely facilitate the formation of ferroelastic $Li_2Mn_2O_4$ domains. [119, 120]

We have also applied the microfracture model to the second generation cathode materials $Li_XNi_{0.8}Co_{0.15}Al_{0.05}O_2$ (NCA) and $LiNi_{1/3}Mn_{1/3}Co_{1/3}O_2$ (NMC), using state-of-charge dependent lattice parameter data from References [29] and [11], respectively. For NCA and NMC compositions with two-phase coexistence, the misfit strains are smaller than those for Li_XCoO_2, [11] so we expect that the critical crystallite sizes for coherency fracture of individual crystallites will be larger than those for Li_XCoO_2. Therefore, we anticipate that in polycrystalline NCA and NMC grain boundary microfracture is the dominant C-Rate independent electrochemical shock mechanism. For both NCA and NMC we have assumed elastic and fracture properties identical to those of $LiCoO_2$ as these materials are structurally similar and no experimental or theoretical values are available for the mechanical properties

of either NCA or NMC. For both NCA and NMC, the critical primary crystallite size for grain boundary microfracture is strongly dependent on the state-of-charge window through which the electrode is cycled. The critical primary crystallite sizes below which materials with the selected NCA and NMC compositions will not fracture are plotted as a function of Li content in Figure 3-13. The values for Li_XCoO_2 (see Table 3.1) are also plotted for comparison. The discrete points represent the compositions at which lattice parameter data was reported for these compounds, and these data points are calculated values; the lines joining data points are guides to the eye only and do not represent the actual transition between the points. Comparing the critical primary crystallite size at $X \simeq 0.5$, for which the Vegard coefficients are given in Table 1.1, the critical primary crystallite size of $Li_{0.5}CoO_2$ is largest, and those of NMC and NCA are similar to each other and both are approximately one fourth as large as the critical size for $Li_{0.5}CoO_2$.

An important conclusion of our analysis is that the observed trends in critical primary crystallite size for microfracture of polycrystals can be rationalized on the basis of the shear component of the transformation strain, which is a measure of the degree of anisotropy in a material's Vegard coefficients. Note that NCA and NMC have opposite sign of the volume change, but the principal shear component of the transformation strain, $\epsilon_c - \epsilon_a$, is almost identical for the two materials: 3.78 % for NCA and 3.97 % for NMC. Therefore, they have similar critical primary crystallite size at $X = 0.5$. The small difference in the critical primary particle size is due to the net volume increase for NMC, which provides a nearly hydrostatic compressive stress which has a stabilizing effect.

The maximum principal shear component of a material's Vegard coefficients thus provides a simple but powerful design criterion for mechanically stable polycrystalline electrode materials. For rhombohedral materials, this maximum principal shear component is linearly proportional to the change in the crystallographic c/a ratio. Previous strategies for crystal chemical engineering of electrode materials have assumed that that near-zero volume

change is the key target. This has led to attempts at engineering compensating anisotropic linear strains to achieve zero net volume change. Such a strategy necessarily introduces a large principal shear component and may be counterproductive if the material is prepared in polycrystalline form. We propose instead that *minimizing the principal shear component* is a more useful design criterion.

It is interesting to compare the predicted critical primary crystallite size for NCA to the experimental results of Itou, *et al.* [29] who observed extensive grain boundary fracture of NCA particles with typical primary crystallite sizes of ∼0.5-1 μm. Based on the first cycle specific capacity of 154 mAh g^{-1}, we estimate that the NCA particles were cycled to a Li-content of $X = 0.45$. The minimum critical primary crystallite size for this state-of-charge window is ∼125 nm, as shown in Figure 3-13. Thus, the actual primary crystallite size of these NCA particles is 4-8 times larger than the critical grain size and it is unsurprising that grain boundary microfracture occurs. Consistent with this analysis, Itou, *et al.* also found that by reducing the first cycle specific capacity to ∼135 mAh g^{-1} ($X \simeq 0.52$), the rate of positive electrode impedance growth was drastically reduced. In light of the state-of-charge dependent critical primary crystallite size, we see that they have electrochemically identified a critical state-of-charge swing, below which widespread microfracture and subsequent impedance growth is avoided. The four-grain ensemble envisaged in the present analytical model assumes the worst possible mutual orientation of the four constituent grains, and therefore provides a conservative lower bound on the critical primary crystallite size below which no electrochemical shock microfracture can occur. Closer quantitative agreement with the observed critical state-of-charge swing may be obtained using a model which embraces a distribution of grain sizes and crystallographic orientations.

There is also an interesting contrast in the impedance growth due to microfracture between monolithic sintered $LiCoO_2$ and polycrystalline NCA particles. While Itou, *et al.* show that microfracture in NCA particles leads to continuous impedance growth, Lai, *et al.*,

have demonstrated stable cycling of monolithic sintered $LiCoO_2$ for ≥ 50 cycles, despite the first cycle damage described here. [116] We speculate that the relative length scales for fracture and electronic conductivity are different in the two microstructures and is the source of their different impedance growth response. In the case of Itou, *et al.*'s NCA particles, cracks are observed throughout the particle, forcing electrons to travel exclusively through the surrounding polymer/carbon composite matrix, even to reach surface sites on what was initially a single polycrystalline particle. In the case of monolithic sintered $LiCoO_2$ electrodes studied presently and by Lai, *et al.*, the sintered electrodes remain intact after extensive cycling; the remaining intact sinter necks between grains provide a continuous percolating path with high electronic conductivity.

Due to its crystal chemical and microstructural origins, we expect that electrochemical shock by grain boundary microfracture will occur in energy storage systems beyond Li-storage compounds. As one example, many Na-storage compounds also have anisotropic Vegard coefficients, as the data collected in Table 4 demonstrate. Therefore, we expect that electrochemical shock will be an important degradation and impedance growth mechanism for Na-ion batteries as well. In many cases, the intercalation host structures are identical between Na- and Li-storage compounds. However, while both Li- and Na-storage compounds have anisotropic Vegard coefficients, there is no general correspondence between the Vegard coefficients of the Li- and Na- analogues. For example, the two-dimensional shear strain ϵ_S for $NaCoO_2$ (4.2 %) is much larger than that of $LiCoO_2$ (1.5 %), but $NaFePO_4$ (2.2 %) is less anisotropic than $LiFePO_4$ (3.4 %). Interestingly, the crystal chemical strategy of offsetting anisotropic linear strains to achieve net zero volume change materials has already been applied to Na-storage compounds: on charging to 4.4 V vs. Na^+/Na, the advanced sodium-ion cathode material $Na_{1.0}Li_{0.2}Ni_{0.25}Mn_{0.75}O_\delta$ undergoes a principal shear strain of 1.4 %, despite the near zero volume change. [25] Based on the analysis presented here, we predict that if this material is prepared as polycrystalline particles, it will nevertheless

experience electrochemical shock and subsequent impedance growth.

3.5 Conclusions

By analogy to thermal shock of anisotropic materials, we predicted, analytically modeled, and experimentally observed C-Rate independent electrochemical shock due to anisotropic Vegard coefficients in polycrystalline Li-storage materials. This degradation mechanism, previously undocumented in electrochemical systems, applies generally to battery materials with anisotropic Vegard coefficients and polycrystalline microstructures. We have used the analytical micromechanical model to explain several observations of grain boundary microfracture in anisotropic Li-storage compounds. The micromechanical model predicts a critical primary crystallite size below which microfracture will not occur, providing an opportunity for microstructural engineering of polycrystalline electrode active particles. Insights gained from this model suggest the principal shear strain as a new and important design criterion for crystal chemical engineering of mechanically robust electrode materials.

THIS PAGE INTENTIONALLY LEFT BLANK

Chapter 4

Two-Phase Coherency Stresses

4.1 Introduction

The third distinct mechanism for electrochemical shock in ion-intercalation materials are coherency stresses, which develop between coexisting phases with dissimilar lattice parameters. As the lattice parameter data in Figure 1-3 demonstrate, many Li-storage compounds have miscibility gaps, evidenced compositions with two distinct lattice parameters. At the interface between the two co-existing phases, the lattice parameter must vary rapidly, which can generate large coherency stresses. Coherency stresses are the dominant electrochemical shock mechanism in Li_XFePO_4 [72], an anisotropic material with essentially no miscibility in the end-member phases at bulk particle sizes (for Li_XFePO_4, particle sizes above $\sim$100 nm behave as bulk).

Even in cubic materials—which have isotropic Vegard coefficients—C-Rate-independent electrochemical shock can occur if there is a miscibility gap. For example, the cubic spinels $Li_XMn_2O_4$ and $Li_XMn_{1.5}Ni_{0.5}O_4$, have isotropic Vegard coefficients (all second rank tensor properties are isotropic for cubic materials), so the grain boundary microfracture mechanism detailed in Chapter 3 is not active. However, these materials have first-

order phase-transformations—with accompanying transformation strains—over parts of the lithium composition region, so two-phase-coherency stresses may be an important electrochemical shock mechanism. Indeed, experimental observations suggest the misfit strain between coexisting cubic phases is strongly correlated with capacity fade in doped spinel materials [121, 122, 123].

The objectives of this chapter are to analyze coherency-stress fracture in model systems, $Li_XMn_2O_4$, $Li_XMn_{1.5}Ni_{0.5}O_4$, and Li_XCoO_2. The spinels $Li_XMn_2O_4$ and $Li_XMn_{1.5}Ni_{0.5}O_4$ are cubic, while layered Li_XCoO_2 is rhombohedral. As with the other electrochemical shock mechanisms, a critical microstructure feature size is identified from a fracture mechanics model. The critical size for coherency-stress driven electrochemical shock is experimentally tested with $Li_XMn_2O_4$ and $Li_XMn_{1.5}Ni_{0.5}O_4$ by acoustic emission experiments during slow C/50 cycling. This electrochemical shock is overcome by identifying a cubic spinel material with no miscibility gap—$Li_XFe_{0.08}Mn_{1.5}Ni_{0.42}O_4$, and even with very coarse particles, this material shows no The effects of anisotropic surface energies, coherency strains, and elastic properties are discussed. In Li_XCoO_2, the coherency strains are stronly anisotropic and a (0001) habit (preferred interface orientation) is expected. In the cubic spinels, anistropy in the elastic constants which may promote a habit plane; as no measured or computed anisotropic elastic properties have been reported for any of the Li-storage spinels, this anisotropy is discussed on the basis of crystal chemical trends in other oxide spinels. This chapter concludes with design criteria for ion-intercalation materials that are resistant to electrochemical shock from coherency stresses.

4.2 Critical Size Estimates

Static calculations of cracked, slab-like particles with a coherent interface between dissimilar phases are performed to study coherency-stress fracture of phase-transforming electrode

materials. These static calculations provide the zero current limit which an appropriate kinetic model must approach. The method of Hu, *et al.*, [72] is employed to estimate the critical crystallite size, below which coherency stresses cannot drive fracture. Two-dimensional finite-element calculations are used to estimate the strain-energy-release rate $\mathcal{G}$, which is a measure of the crack growth driving force. When the strain energy release rate exceeds a critical value, set by the surface energy, pre-existing cracks can grow. A fixed geometry, shown in Figure 4-1, is assumed, with equal fractions of two coexisting, misfitting phases in a single slab-like particle, with each phase having a characteristic linear dimension d. A pre-existing crack, of length L is assumed to exist along the interface between the two phases. The analysis is restricted to cracks growing inward from a free surface on the interface plane, as illustrated in Figure 4-1.

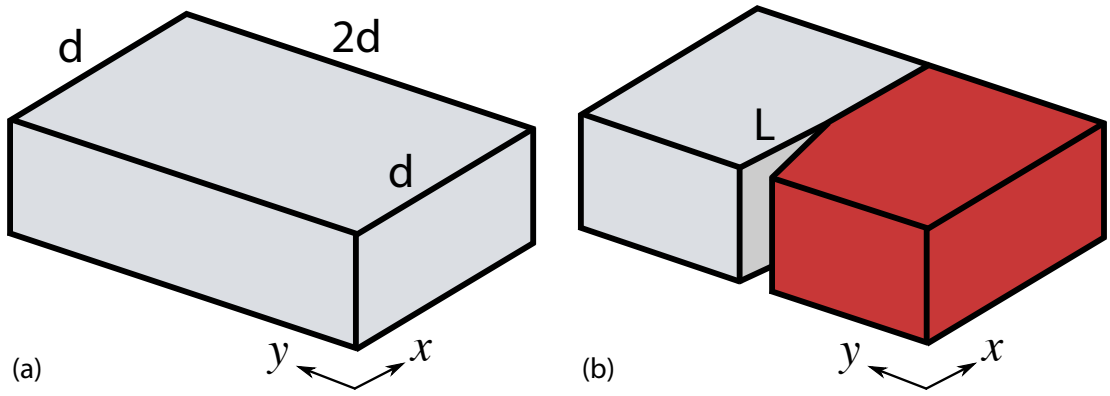

Figure 4-1: Illustration of the single crystal particle geometry envisaged in the coherency stress fracture analysis. (a) particle in the untransformed single phase state and (b) two-phase particle with a crack growing inward from the crystallite surface along the two-phase interface.

As described in Section 1.4, dimensional arguments show that the strain energy release rate can be expressed as

$$\mathcal{G} = Z\left(\frac{L}{d}\right) E\epsilon^2 d$$

Where E is a characteristic elastic modulus and ϵ is a characteristic strain. Pre-existing cracks can grow when the strain-energy-release rate exceeds the work required to create two

new fresh surfaces, of surface area γ. The dimensionless function $Z\left(\frac{L}{d}\right)$ has a maximum value, $Z_{\max}$, which ensures that there is a critical particle size d below which no pre-existing crack can grow. This critical particle size is given by

$$d_{\text{crit}} = \frac{2\gamma}{Z_{\max} E \epsilon^2} \tag{4.1}$$

To determine the dimensionless strain-energy release rate, $Z\left(\frac{L}{d}\right)$, we compute the total stored elastic strain energy for cracked particles with crack lengths $\frac{L}{d} = 0.05$, 0.08, 0.1, 0.15, 0.2, 0.3, 0.4, 0.5, 0.6, 0.7, 0.75. All Finite Element calculations are performed using OOF2 (version 2.1.7), a 2-dimensional finite element tool developed at NIST [124, 125, 126, 127] for finite element calculations. The crack tip is densely meshed with the finest elements near the tip less than 5×10^{-3} of the crack length. The two dimensional finite element calculations remove the third dimension with a plane strain assumption and the external surfaces are traction-free. At each crack length, the total stored elastic strain energy is integrated and we interpolate between these crack lengths with a cubic spline to estimate the strain energy density as a function of crack length $U_E\left(\frac{L}{d}\right)$. The dimensionless strain-energy release rate $Z\left(\frac{L}{d}\right)$ is estimated from the derivative of this strain energy function as $Z = -\frac{1}{E\epsilon^2 d}\frac{\mathrm{d}U_E}{\mathrm{d}(L/d)}$.

4.2.1 Critical Size for Coherency Fracture in Cubic Spinels

$\mathrm{Li}_X\mathrm{Mn}_2\mathrm{O}_4$ and $\mathrm{Li}_X\mathrm{Mn}_{1.5}\mathrm{Ni}_{0.5}\mathrm{O}_4$ are both cubic spinel materials which remain cubic throughout electrochemical cycling for compositions $X \leq 1$. In each of these materials, there is a two-phase region, in which two cubic phases with lattice parameters differing by $\sim 1\%$ coexist. In $\mathrm{Li}_X\mathrm{Mn}_2\mathrm{O}_4$, there is a single two-phase region for compositions $0.5 \leq X \leq 0.25$. In $\mathrm{Li}_X\mathrm{Mn}_{1.5}\mathrm{Ni}_{0.5}\mathrm{O}_4$ the phase behavior is closely linked to the ordering of Ni and Mn cations on their sublattice [128], and if they are highly ordered, two distinct two-phase regions are observed, whereas if they are disordered (as occurs under oxygen-deficient conditions), the phase behavior mirrors that of $\mathrm{Li}_X\mathrm{Mn}_2\mathrm{O}_4$ with a single-phase region and a single two-phase

region.

For both of these spinel materials, the two-phase coherency fracture problem is quantified using isotropic elastic constants of $E = 143$ GPa [78], $\nu = 0.3$, and a linear transformation strain of $\epsilon = 0.01$. For $Li_XMn_{1.5}Ni_{0.5}O_4$, the elastic properties are assumed identical to that of $LiMn_2O_4$. Figure 4-2 shows the computed stored elastic strain energy at different crack lengths for these two-phase spinel particles. The points represent computed values and the red curve is the B-spline interpolant.

Figure 4-3 shows the dimensionless strain-energy-release rate $Z\left(\frac{L}{d}\right)$ estimated from the strain energies of the cracked, two-phase spinel particles. The maximum value of the dimensionless strain-energy-release rate is $Z_{\max} = 0.0735$ which occurs at a fractional crack lenth of $\frac{L}{d} = 0.27$. Substituting the value of $Z_{\max}$ into Equation 4.2 along with the misfit strain of $\epsilon = 0.01$, the elastic modulus of $E = 143$ GPa gives estimates of the critical particle size. As the surface energies are anisotropic, different interface orientations are considered; Table 4.1 lists the surface energies and estimated critical particle sizes for a variety of possible interface orientations based on the surface energies computed by Benedek, *et al.*, [129]. The range of critical particle size, depending on crystallographic orientation is 1.1-2.47 μm. Note that because the shape change is isotropic, and isotropic elastic properties are used, the strain energy is not a function of the interface orientation. With anisotropic elastic constants, this would no longer hold; at present, the bulk modulus is the only measured or computed elastic property of either of these spinels.

4.2.2 Critical Size for Coherency Fracture in Layered Li_XCoO_2

The region of two-phase coexistence [7] $0.93 \leq X \leq 0.74$ in Li_XCoO_2 presents the possibility of fracture within individual primary crystallites due to coherency stresses. The same methodology is applied to estimate the critical crystallite size below which a two-phase Li_XCoO_2 crystal will not fracture along the two-phase interface. As the lattice pa-

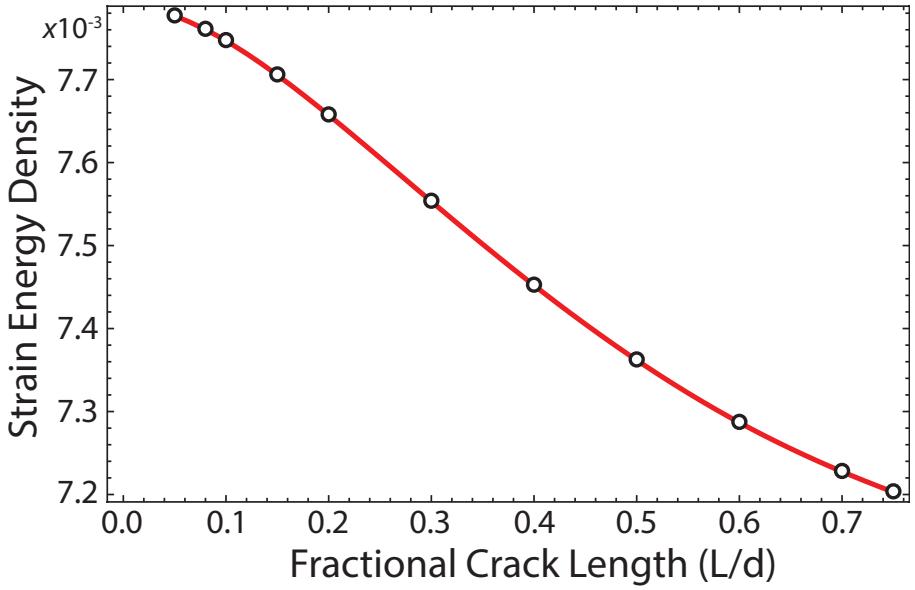

Figure 4-2: The calculated (dimensionless) strain energy density for a two-phase $LiMn_2O_4$ particle.

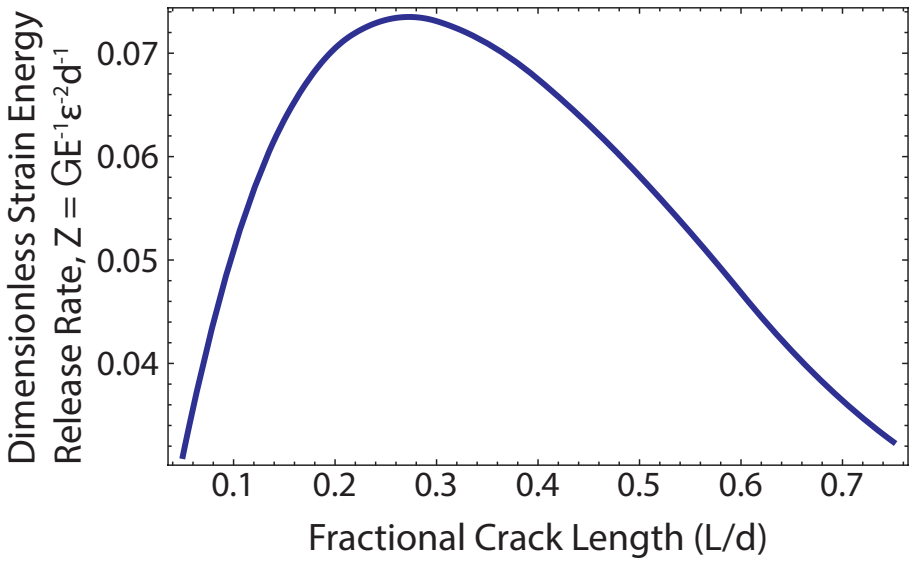

Figure 4-3: The calculated (dimensionless) strain energy release rate for a two-phase $Li_XMn_2O_4$ particle.

Table 4.1: Surface energies (from Ref. [129]) for specific surfaces and the corresponding critical primary crystallite size for coherency fracture along that interface in a two-phase $Li_XMn_2O_4$ crystal (plane strain conditions).

Interface Orientation	Surface Termination	Surface Energy (J m^{-2})	Critical Crystallite Size (μm)
(001)	MO	0.98	1.86
(001)	L	0.58	1.10
(110)	MO	1.19	2.26
(110)	LMO	0.99	1.88
(111)	LMO	1.29	2.45
(111)	O	1.30	2.47
(111)	M,L	0.85	1.62

rameters of both phases vary with composition, the worst-case scenario is analyzed where the misfit strains are $\epsilon_a = \epsilon_b = -0.12\%$ and $\epsilon_c = +1.23\%$. The c-axis strain, $\epsilon_c = 0.0123$ is used as the characteristic strain defining the dimensionless strain-energy release rate, Z ($^L/_d$). We consider both plane strain (thick slab) and plane stress (thin slab) conditions for several possible interface orientations: $(0001), (10\bar{1}0), (11\bar{2}0)$, and $(10\bar{1}4)$.

As in Chapter 3, isotropic linear elastic properties and anisotropic coherency strains are used for Li_XCoO_2. The linear elastic properties (E, ν) are taken identical to those used in the grain boundary microfracture analysis, and the orientation-dependent surface energies calculated by Kramer, *et al.* [130] are used to estimate the orientation-dependent critical strain-energy-release rate. While anisotropic elastic constants have been calculated for $LiCoO_2$ using an empirical potential [111], they are strongly overbound compared to experimental measurements of the elastic properties of $LiCoO_2$ [79, 110] and therefore they are not used in the critical size analysis.

Figure 4-4 shows the strain energy density at different crack lengths for two-phase Li_XCoO_2 particles under both plane strain and plane stress conditions with an interface orientation of $(10\bar{1}4)$. The points are the computed values and the curves are B-spline interpolants. Figure 4-5 shows the computed dimensionless strain energy release rate for plane

strain and plane stress conditions of a two-phase Li_XCoO_2 particle with a $(10\bar{1}4)$ interface orientation.

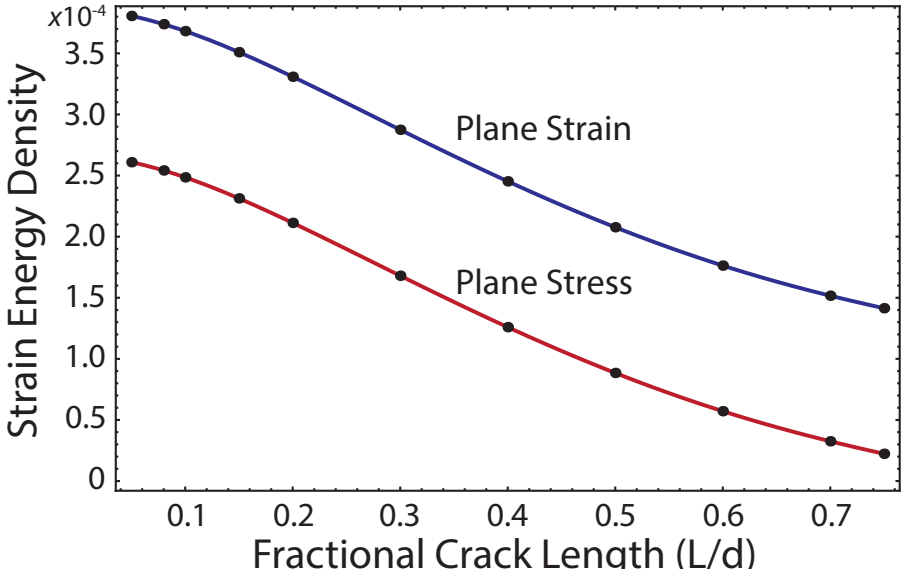

Figure 4-4: The calculated (points) and third-order spline interpolants to the (dimensionless) stored elastic strain energy density U_E for a two-phase Li_XCoO_2 particle with the phase boundary oriented along a $(10\bar{1}4)$ plane.

For Li_XCoO_2, the critical crystallite size is strongly dependent on the interface orientation, and the minimum critical crystallite size for all the configurations modeled here is 8.3 μm, for an $(11\bar{2}0)$ interface orientation. The critical crystallite sizes for each of the interface orientations considered under plane strain conditions are given in Table 4.2, along with the corresponding surface energy from Kramer, *et al.* [130] The critical crystallite sizes under plane stress are greater than those under plane strain conditions, consistent with the results of Hu, *et al.* for coherency stress fracture in Li_XFePO_4. [72] The greatest critical primary crystallite size among all orientations considered was 229 μm, for an (0001) interface orientation. While the surface energy is an effective crack growth resistance, the results in Table 4.2 show no simple relationship between surface energy and the calculated critical crystallite size; this implies that the elastic stress distributions are strongly sensitive to the interface orientation. This is consistent with previous analyses of other Li-storage

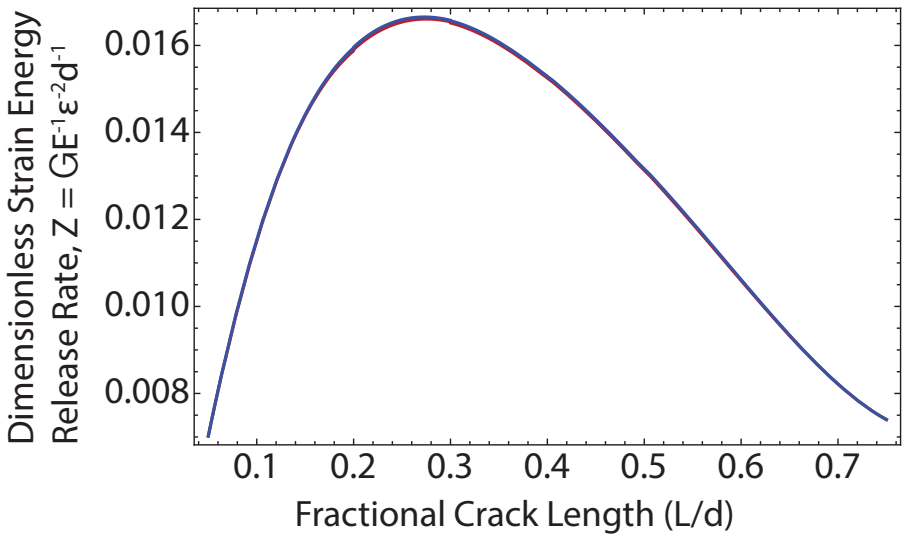

Figure 4-5: The calculated (dimensionless) strain energy release rate for a two-phase Li_XCoO_2 particle with the phase boundary oriented along a $(10\bar{1}4)$ plane. The lines for plane strain and plane stress conditions overlap significantly.

Table 4.2: Surface energies (from Ref. [130]) for specific surfaces and the corresponding critical primary crystallite size for coherency fracture along that interface in a two-phase Li_XCoO_2 crystal (plane strain conditions).

Interface Orientation	Surface Energy (J m^{-2})	Critical Crystallite Size (μm)
(0001)	~1	229
$(10\bar{1}0)$	2.943	10.9
$(11\bar{2}0)$	2.241	8.3
$(10\bar{1}4)$	1.048	9.6

compounds with anisotropic coherency strains such as Li_XFePO_4. [131, 132]

4.3 Experimental Validation of Critical Size

The critical particle size effect is experimentally tested with comparative acoustic emission measurements duing slow first cycle charging of spinel $Li_XMn_2O_4$ and $Li_XMn_{1.5}Ni_{0.5}O_4$ electrodes with different particle sizes.

Figure 4-6 shows scanning electron micrographs of the $LiMn_2O_4$ materials as received

and after coarsening by sintering and grinding. The as-received powder has primary particle sizes ~ 1 μm while the coarsened material has primary particles $\sim 2-5$ μm. Both materials are used to prepare 500 μm thick composite pellet electrodes composed of 90 weight percent active material, 5 weight percent binder, and 5 weight percent carbon black. The composite electrodes are electrochemically cycled in a coin cell against a lithium metal negative electrode with simultaneous acoustic emission measurement.

Figure 4-7 shows the cumulative acoustic emission counts as a function of composition during the first C/50 charge of composite $Li_XMn_2O_4$ electrodes with different particle sizes. The electrode prepared from as-received $Li_XMn_2O_4$, with typical particle size of ~ 1 μm, shows almost no acoustic emission. On the other hand, coarsened $Li_XMn_2O_4$, with typical particle size of 2–5 μm, shows substantial acoustic emission, concentrated in the two-phase region. These experimental observations are in agreement with the predicted critical particle sizes of ~ 2 μm in Table 4.1.

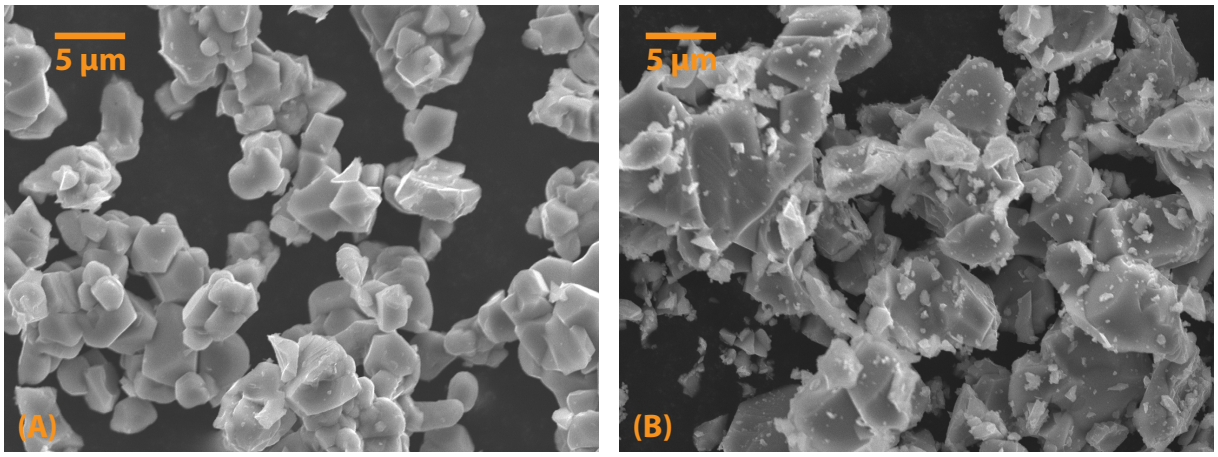

Figure 4-6: SEM comparison of $LiMn_2O_4$ particles. The as-received particles have a primary particle size of $\sim$1 μm while the coarsened particles are $\sim$2-5 μm.

Figure 4-8 shows scanning electron micrographs of the $LiMn_{1.5}Ni_{0.5}O_4$ materials as received and after coarsening by sintering and grinding. The as-received powder has primary particle sizes $\sim$ 500 nm while the coarsened material has primary particles $\sim 2-5$ μm.

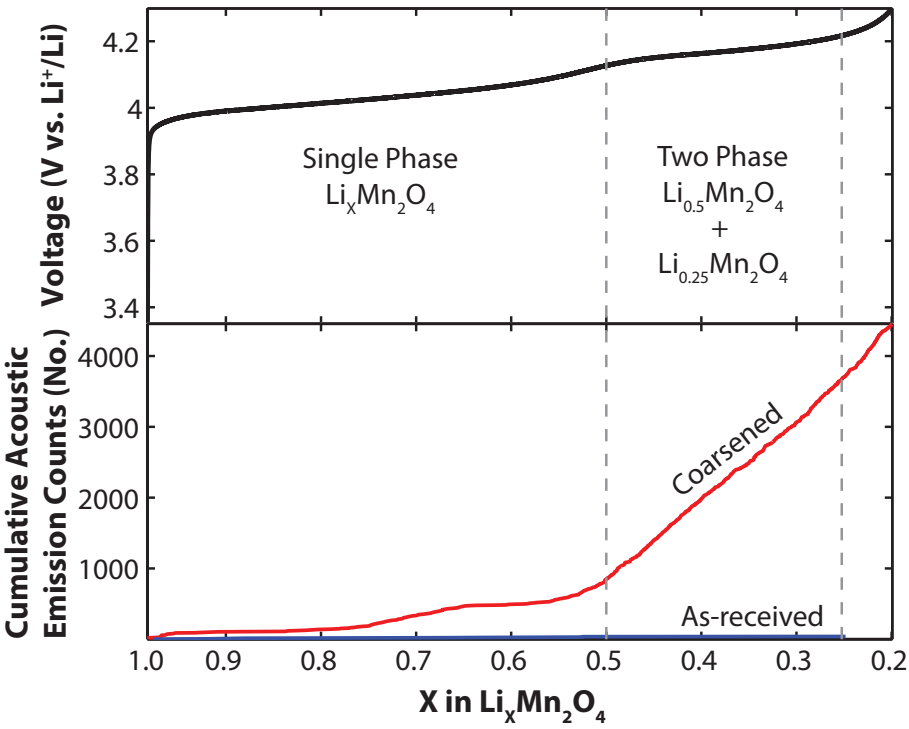

Figure 4-7: Half-cell voltage and cumulative acoustic emission counts measured during first-cycle C/50 charge of the $Li_XMn_2O_4$ materials shown in Figure 4-6. The as-received material has typical particle size of ~1 μm while the coarsened particles are ~2-5 μm.

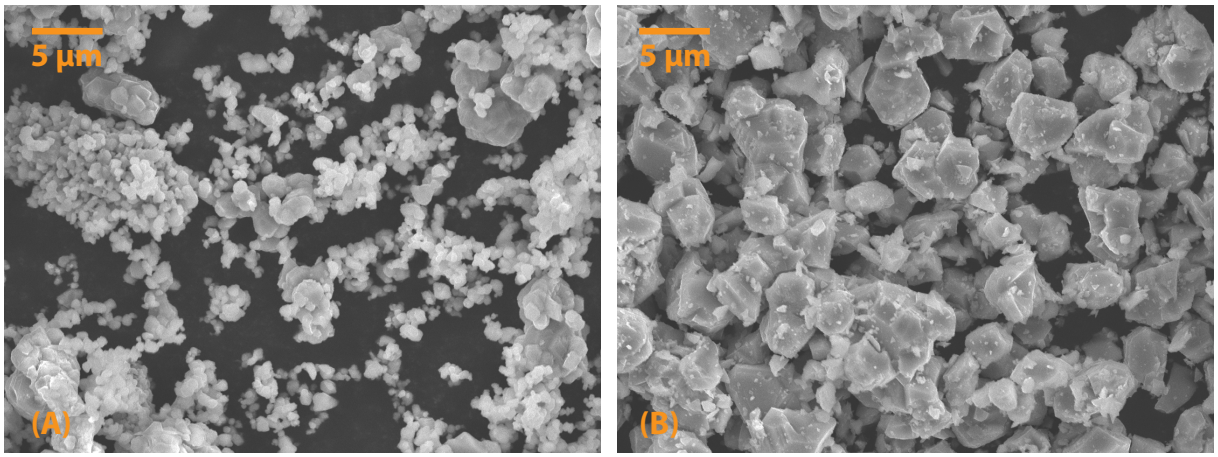

Figure 4-8: SEM comparison of $LiMn_{1.5}Ni_{0.5}O_4$ particles. The as-received particles have a primary particle size of ~500 nm while the coarsened particles are 2-5 μm.

Figure 4-9 compares the observed acoustic emission during C/50 cycling of thick composite electrode with each of these materials. The heat treatment applied to the coarsened materials yields material with a disordered transition metal sublattice, in which case the material has a single two-phase region, analogous to $Li_XMn_2O_4$. The measured acoustic emission in the coarsened $Li_XMn_{1.5}Ni_{0.5}O_4$ material is in excellent agreement with the results from $Li_XMn_2O_4$, showing significant acoustic emission again concentrated in the two-phase region. Again, the as-received material is below the critical particle size identified in the preceding section, while the coarsened material exceeds that critical particle size.

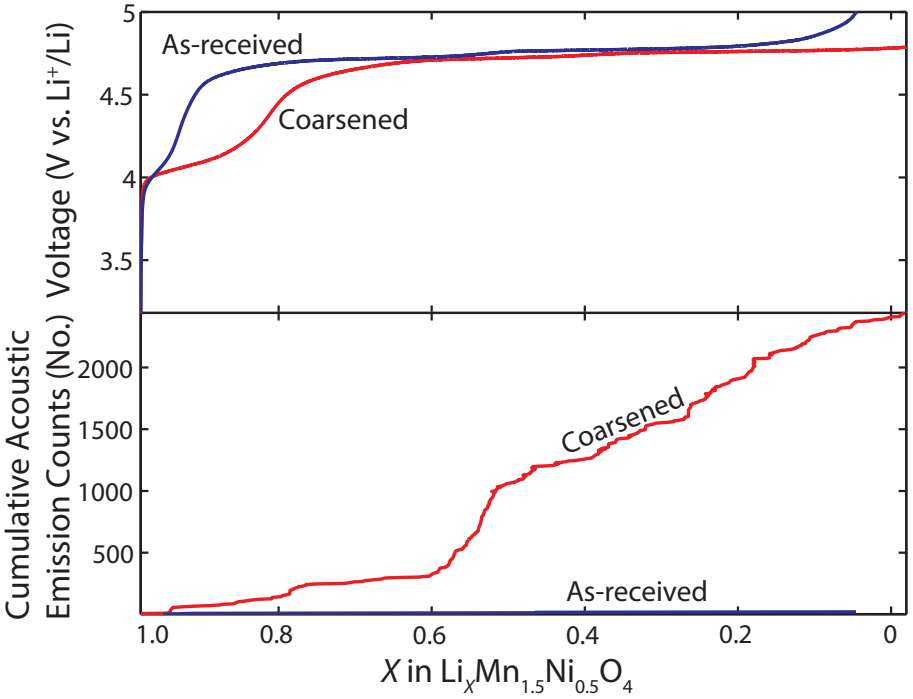

Figure 4-9: Half-cell voltage and cumulative acoustic emission counts measured during first-cycle C/50 charge of the $Li_XMn_{1.5}Ni_{0.5}O_4$ materials shown in Figure 4-8. The as-received material has typical particle size of ~500 nm while the coarsened particles are 2-5 μm.

4.3.1 Averted Fracture in Single-Phase Spinel

One strategy for averting coherency-stress electrochemical shock is to identify ion-intercalation materials which do not undergo a first-order phase-transformation.

$LiMn_{1.5}Ni_{0.42}Fe_{0.08}O_4$ has been identified as one such material, which remains in a single cubic spinel phase over the range of compositions through which electrochemical cycling is performed. This material has been studied previously, and has been reported to have improved rate capability and capacity retention compared to undoped material $Li_XMn_{1.5}Ni_{0.5}O_4$ [123], which has been attributed to spontaneous preferential segregation of Fe-ions to the surface of the particles [133]. However, the composition-dependent lattice parameters of the Fe-doped material have not been previously reported in the literature.

Figure 4-10 shows the measured lattice parameters for $Li_XFe_{0.08}Mn_{1.5}Ni_{0.42}O_4$ at different lithium compositions X; the points are the measured lattice parameter values and he dashed line is the best linear fit to the data. Extrapolation of the linear fit shows that this material has a total volume change of $\sim$4% for complete delithiation. These samples were electrochemically delithiated in composite pellet electrodes charged at a C/50 rate to 4.9 V vs. Li^+/Li, then discharged at C/50 to specified state of charge. Due to the high operating voltage of this material, there is appreciable uncertainty in the compositions, which are determined coulometrically, due to electrolyte oxidation at high potentials. Based on the best-fit line to the measured lattic parameters, the total volume change for this material is $\sim$4% for complete deintercalation from a composition of $X = 1$ to $X = 0$.

Figure 4-11 compares the observed C/50 acoustic emission from $Li_XFe_{0.08}Mn_{1.5}Ni_{0.42}O_4$ to the $Li_XMn_{1.5}Ni_{0.5}O_4$ data from Figure 4-9. Again, the C/50 cycling of thick composite electrode with each of these materials. While the $Li_XFe_{0.08}Mn_{1.5}Ni_{0.42}O_4$ particles are even coarser than the coarsened $Li_XMn_{1.5}Ni_{0.5}O_4$ particles, $\sim$5-7 μm, they show essentially no acoustic emission; a total of 47 counts are measured during the C/50 cycle. The capacity is less because some Ni has been replaced by Fe, reducing the theoretical capacity of the material. While there have been reports of preferential Fe-segregation to the particle surface, the thickness of the Fe-rich shell region is on the order of 10 nm, for particles of several micron size (as determined by Secondary Ion Mass Spectroscopy) [133]; this thin of a shell cannot

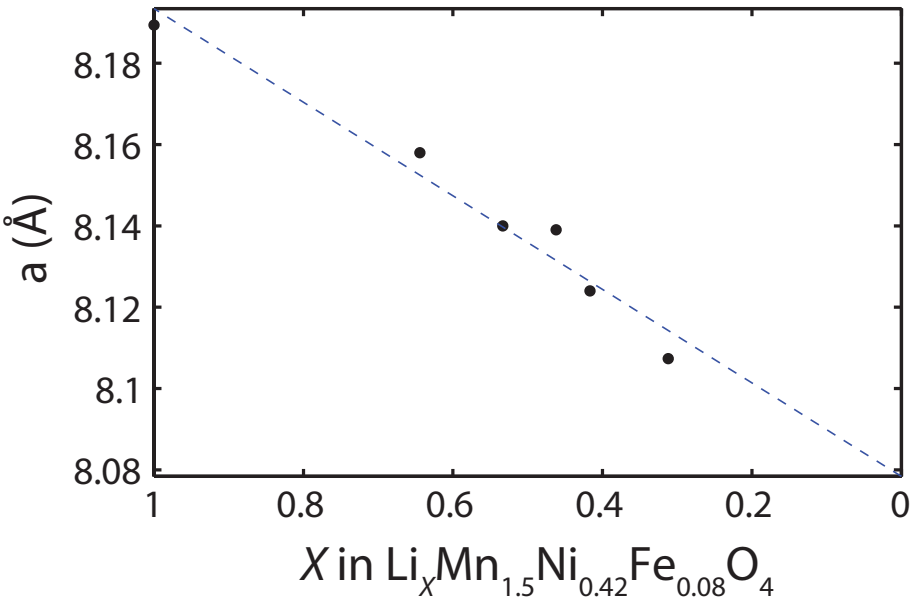

Figure 4-10: Lattice parameter data as a function of lithium composition X for electrochemically delithiated $Li_XMn_{1.5}Ni_{0.42}Fe_{0.08}O_4$.

provide sufficient clamping to prevent electrochemical shock.

At each of these compositions, the X-ray diffraction patterns appear single phase to the limit of detection of the measurement. In any case, if there is two-phase coexistence, the misfit strain is very small. However, it is not clear *why* the material is single phase with respect to lithium composition. Lee and Persson report that in the undoped material, the phase-behavior is strongly coupled to the Ni/Mn cation ordering [128] and this is supported by experimental observations [134]. There is also evidence of local ordered-domains, even in nominally disordered material, on the basis of Reitveld refinement of neutron diffraction data [133]. The addition of iron may promote a disordered cation arrangement due to an increase in configurational entropy for a three-component cation sublattice over a two-component (at 300 K and with $x_{\mathrm{Fe}} = 0.08$, the three component system has a $-T\Delta S$ stabilization of 274 J/mol), but there may be additonal enthalphic contributions that are difficult to name *a priori*.

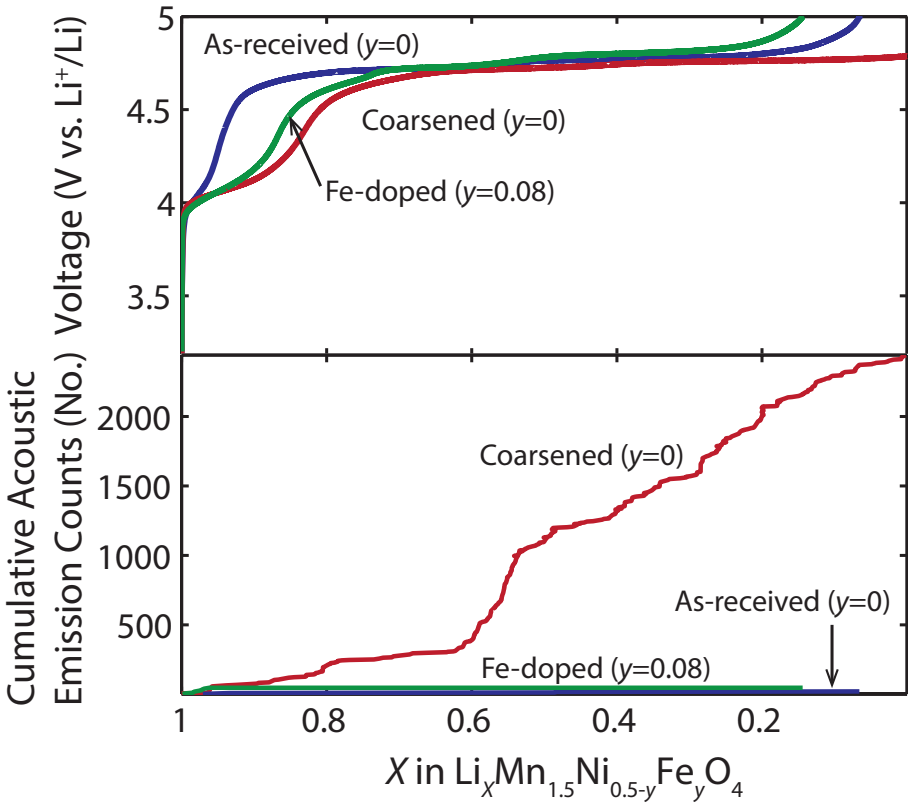

Figure 4-11: Half-cell voltages and cumulative acoustic emission counts measured during first-cycle C/50 charge of ~7 μm $LiMn_{1.5}Ni_{0.42}Fe_{0.08}O_4$ particles, compared to the $LiMn_{1.5}Ni_{0.5}O_4$ materials previously shown in Figure 4-9.

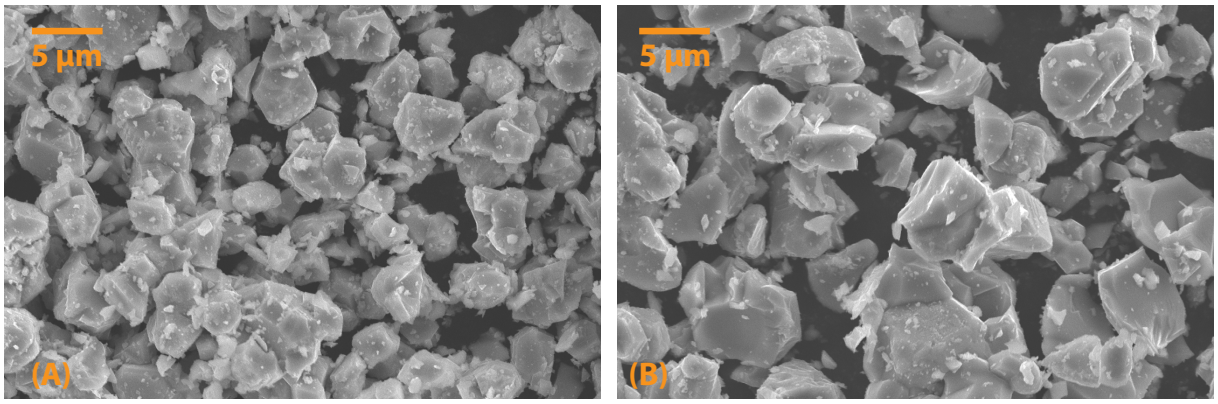

Figure 4-12: SEM comparison of coarsened $LiMn_{1.5}Ni_{0.5}O_4$ and particles. The coarsened $LiMn_{1.5}Ni_{0.5}O_4$ particles are 2-5 μm while the coarsened particles are larger still, ~5-7 μm.

4.4 Preferred Interface Orientations

In most coherent phase-transformations there is a specific interface orientation which minimizes the elastic energy of the coherent two-phase configuration. Such a preferred interface orientation is known as a habit plane, and the orientation of the habit plane depends on the elastic properties of the coexisting phases and the misfit strain between them. For non-cubic materials, such as Li_XCoO_2, both the transformation strain and the elastic constants can be anisotropic, while for cubic materials, anisotropy in the elastic constants determines the habit.

The habit plane orientation can be estimated using the formalism developed by Khachaturyan [135, 136]. Under the assumption that the two co-existing phases have identical elastic properties (homogeneous modulus assumption), the orientation-dependent strain energy density $B(\vec{n})$ for a coherent interface normal to the direction $\vec{n}$ is given as

$$B(\vec{n}) = c_{ijkl}\epsilon^{\circ}_{ij}\epsilon^{\circ}_{kl} - n_i\sigma^{\circ}_{ij}\Omega_{jl}(\vec{n})\sigma^{\circ}_{lm}n_m \tag{4.2}$$

where σ°_{ij} is the homogensous stress that would arise if the stress-free strain were applied elastically and $\Omega_{jl}(\vec{n})$ is an effective directional modulus, defined by its inverse

$$\Omega^{-1}_{ij}(\vec{n}) = c_{ijkl}n_k n_l \tag{4.3}$$

The habit plane minimizes the strain energy density $B(\vec{n})$.

For Li_XCoO_2, the anisotropic elastic constants computed by a pair-potential model [111] are used to qualitatively assess the possibility of a habit plane. While these elastic properties are quantitatively overbound compared to experimental measurements, they can be used to provide qualitative insight to likely habit planes. The anisotropic misfit strains used to estimate the critical crystallite size are used to quanitify $B(\vec{n})$.

Figure 4-13 shows the three-dimensional strain energy function $B(\vec{n})$ for two-phase configurations in Li_XCoO_2. The key feature is the minimized energy density near a (0001) two-phase interface orientation; thus, interface orientations slightly away from (0001) should

be **strongly** preferred relative to the other orientations considered in Table 4.2. The minimum in $B(\vec{n})$ is at an irrational direction; the closest rational direction is [3002]. This can be simply rationalized due to the small misfit strain along the crystallographic a and b directions. While the other interface orientations described in the preceding section are possible, they should be less likely than the (0001) interface. Thus, two-phase coherency stresses may only drive fracture in extremely large particles of Li_XCoO_2.

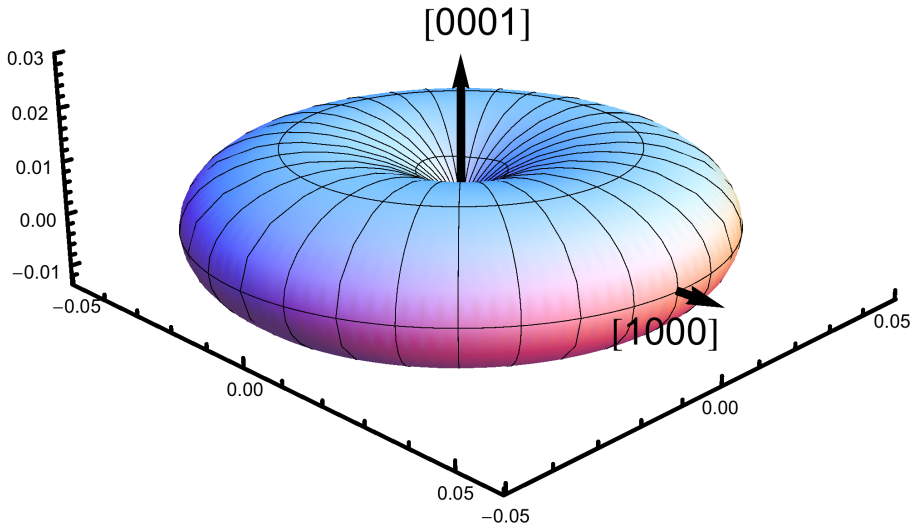

Figure 4-13: The strain energy density $B(\vec{n})$ for a coherent two-phase interface in Li_XCoO_2 for different phase boundary orientations.

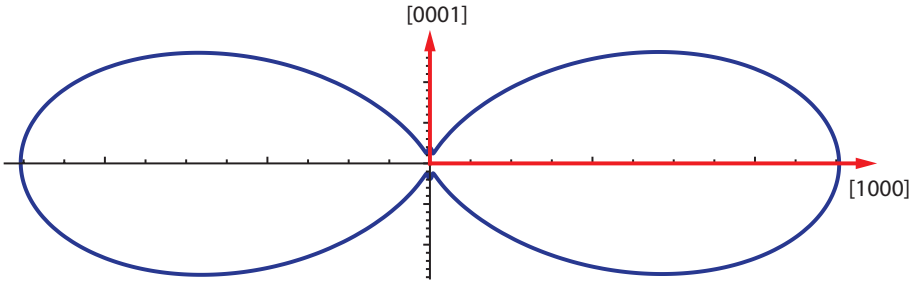

Figure 4-14: The strain energy density $B(\vec{n})$ for a coherent two-phase interface in Li_XCoO_2 for different phase boundary orientations projected in the $a-c$ plane. The minimum energy orientation is an irrational direction close to the [0001] direction.

In cubic-to-cubic phase-transformations, a habit plane can develop due to the anisotropy

of the elastic constants. The critical crystallite size calculations for the cubic spinels have been performed assuming isotropic elastic constants, where there is no preferred interface orientation. At present, this assumption was necessitated by the lack of measured or computed anisotropic elastic properties for the Li-storage spinel materials. To date, only bulk modulus measurements have been reported.

In the absence of quantitative values for the anisotropic elastic constants of these Li-storage spinel materials, it is useful to consider crystal chemical trends observed in other cubic oxide spinels. In cubic materials, the Zener anisotropy factor (Zener ratio) defined as

$$A = \frac{2c_{44}}{c_{11} - c_{12}} \tag{4.4}$$

is a scalar metric which describes the elastic anisotropy. For materials with $A > 1$, the <111> directions are stiffest and the <100> directions most compliant. For materials with $A < 1$, the opposite is true and the material is stiffest along <100> directions and most compliant along <111> directions. Finally, note that for a stable material, $A > 0$ (This is required to ensure the elastic constants are positive definite).

Table 4.3 collects the elastic constants for several oxide spinels and the corresponding Zener ratio. For all of the spinel oxides listed here, $A > 1$, suggesting that these materials are all stiffest along the <111> directions (this is normal to the approximately cubic-close-packed oxygen anion layers in these materials. As a result, cubic-to-cubic phase-transformations in any of these spinel oxides will prefer a (100) habit. In fact, among oxide spinels, it has been noted that the bulk modulus is strongly correlated with the valence of the tetrahedral cation, with reasoning that the tetrahedra are more compliant than the octahedra, and lower valent tetrahedral cations generally form weaker A-O bonds than more highly charged cations [137, 138]. The degree of elastic anisotropy, as quantified by the Zener ratio, is correlated with the value of the oxygen positional parameter u [139]. Figure 4-15 plots the Zener ratio A for the cubic oxide spinels in Table 4.3 as a function of the oxygen position parameter u. For a prototype spinel, $u = 0.25$, and departures from this value represent

Table 4.3: Experimental single crystal elastic constants of some cubic oxide spinels.

Material Composition	Cation Distribution	c_{11} (GPa)	c_{12} (GPa)	c_{44} (GPa)	B (GPa)	u (-)	A (-)	Ref
$MgAl_2O_4$	normal	279	153	153	195	0.262	2.42	[140]
Ni_2SiO_4	normal	366	155	106	225	0.244	1.00	[139]
Mg_2GeO_4	normal	300	118	126	179	0.251	1.38	[141, 142]
$ZnFe_2O_4$	normal	250	148	96	182	0.261	1.89	[143, 144]
$CoAl_2O_4$	normal	291	170	139	210	0.262	2.30	[145, 146]
Fe_3O_4	inverse	268	106	95	160	0.255	1.18	[147]
Mg_2SiO_4	normal	327	126	112	193	0.244	1.11	[148]
Fe_2TiO_4	inverse	139	112	40	121	0.265	2.9	[149]
$FeAl_2O_4$	normal	266	183	134	211	0.265	3.2	[150]
$ZnAl_2O_4$	inverse	290	169	146	209	0.263	2.41	[151, 152]
$LiMn_2O_4$	normal				110-140	0.263		[78, 138]
$LiMn_{1.5}Ni_{0.5}O_4$	normal					0.263		[153]

distortions of the BO_6 octahedra (the AO_4 tetrahedra are not distorted, regardless of the value of u). The observed oxygen positional parameter in both $LiMn_2O_4$ and $LiMn_{1.5}Ni_{0.5}O_4$ is $u = 0.263$, which is very similar to that of $MgAl_2O_4$, which has a Zener ratio of $A = 2.42$. Thus, there may be a strong preference for (100) interface orientations in these cubic Li-storage spinels.

4.5 Conclusions

Electrochemical shock is observed during low C-Rate (C/50) first cycle charging of phase-transforming electrode materials $Li_XMn_2O_4$ and $Li_XMn_{1.5}Ni_{0.5}O_4$ *via* acoustic emssion measurements. In both materials, the observed acoustic emission is concentrated in the two-phase region, and has a strong particle size dependence, consistent with predictions from static analysis of coherency stresses in slab-like particles. This electrochemical shock mechanism is averted in $Li_XFe_{0.08}Mn_{1.5}Ni_{0.42}O_4$, a Fe-doped version of $Li_XMn_{1.5}Ni_{0.5}O_4$; this material

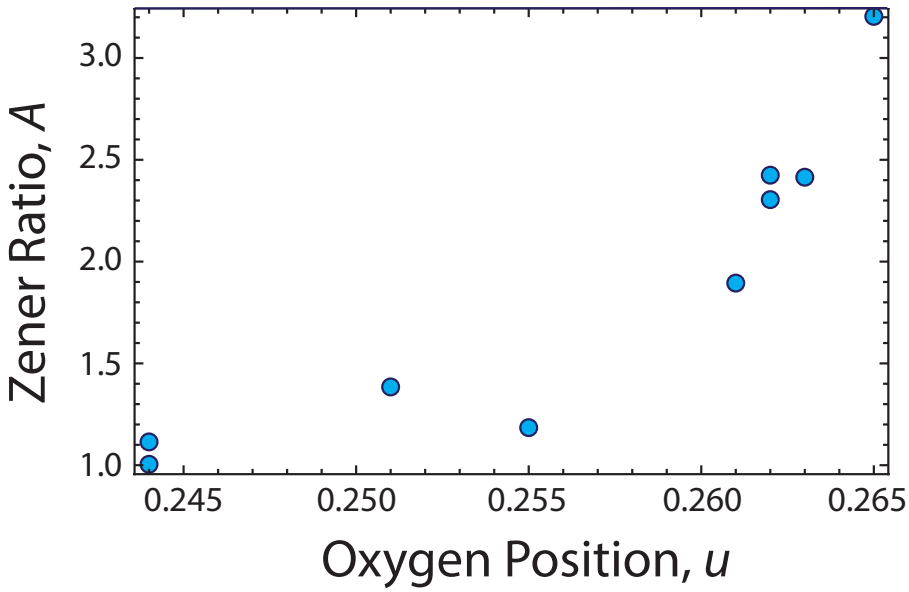

Figure 4-15: The Zener ratio A of cubic oxide spinels is well correlated against the oxygen position parameter u. The Li-storage spinels $LiMn_2O_4$ and $LiMn_{1.5}Ni_{0.5}O_4$ both have $u = 0.263$ which interpolates to a value of $A \simeq 2.4$.

is isostructural to $Li_XMn_2O_4$ and $Li_XMn_{1.5}Ni_{0.5}O_4$, but the phase-behavior is qualitatively different, avoiding coherency stresses as a possible electrochemical shock mechanism.

The design of materials that avoid misfitting, coherent phase-transformations has been previously identified as a route to electrode materials with enhanced rate capability [154, 155, 156, 157]. Metastable intermediate phases, and enhanced solid solubility have been observed in olivine materials such as $LiFePO_4$ at very small particle sizes, $\sim 10-100$ nm, where chemical modifications which reduce misfit strains can also promote facile phase-transformation kinetics [12]. Similar effects may be observable in these spinel materials, which also have a first-order phase-transformation and a misfit strain. Based on the collected observations that chemical modifications can modulate the transformation strains and miscibility limits of the spinels, there is an opportunity to explore analogous size-dependent phase-transformation pathways in chemically modified-spinel materials. Nano-sized, chemically modified, spinel materials will provide an interesting model system to explore the generality of these strategies to modulate phase behavior in ion-intercalation materials.

Chapter 5

Concurrent Concentration-Gradient and Coherency Stresses

5.1 Introduction

Many ion-intercalation compounds have complex phase-behavior with regions of limited solid solubility and regions of two-phase coexistence [15, 18, 6, 7, 13, 11]. In these realistic systems, C-Rate-dependent and C-Rate-independent electrochemical shock mechanisms may be simultaneously active, and therefore it is important to distinguish which mechanism dominates at different particle sizes and cycling rates. While there are several existing kinetic analyses of elastic stresses in electrode materials with limited solid-solubility [74, 47, 75, 64], none has employed a fracture mechanics failure criterion, which is essential for brittle oxide materials [87].

The objective of this chapter is to develop a kinetic model for electrochemical shock in a lithium-storage material with complex phase-behavior. Such a model will allow simultaneous and equal treatment of C-Rate-dependent concentration-gradient stresses and C-Rate-independent two-phase-coherency stresses. In general, transitions in the dominant

mechanism may be expected at different characteristic microstructural length scales or different electrochemical cycling rates; it is important to understand if these transitions occur at practically relevant particle sizes and cycling rates.

This chapter is organized as follows. First, the electrochemical kinetics model presented in Chapter 2 is generalized to apply to phase-transforming electrode materials, using an explicit boundary tracking method to solve the resulting moving phase boundary problem. This generalized electrochemical model is coupled with the previously derived linear-elastic fracture mechanics model for electrochemical shock. Using $Li_XMn_2O_4$ as a model system, for which quantiative results are obtained, concurrent C-Rate-dependent and C-Rate-independent electrochemical shock mechanisms are compared to determine which mechanism dominates under various conditions of particle size and C-Rate. The model confirms that coherency stress fracture occurs essentially independent of C-Rate and corroborates both the experimental acoustic emission measurements and static fracture mechanics analysis from Chapter 4.

5.2 Methods

We model constant-current electrochemical charging (delithiation) of a single spherical particle of radius $r_{\max}$ in a half cell. The particle is assumed to contain a dominant pre-existing flaw in the form of a finite-sized semi-elliptical surface crack of length a, and we assume that the crack faces are electrochemically inert so that only the spherical outer surface of the particle is reactive. This configuration is identical to that described in Chapter 2. Again, the stress-intensity factor is estimated using a two-step approach in which the composition and diffusion-induced elastic stress distributions for the flaw-free particle are first computed; then, we use the hoop (tangential) stress distributions as input to a method of weight functions calculation of the Mode I stress-intensity factor as a function of flaw-size and time $K_{\mathrm{I}}(a,t)$ as described in Chapter 2.

We model the evolving composition field in each particle using a generalized diffusion equation with a composition-dependent chemical diffusivity as described in Chapter 2

$$\frac{\partial X}{\partial t} = \frac{1}{r^2}\frac{\partial}{\partial r}\left(r^2 \tilde{D}(X)\frac{\partial X}{\partial r}\right)$$

The composition-dependent chemical diffusivity $\tilde{D}(X)$ includes thermodynamic non-ideality and elastic coupling effects and can be expressed in terms of fundamental materials properties as

$$\tilde{D}(X) = D_0 X\,(1-X)\left(-\frac{\mathcal{F}}{RT}\frac{\partial V(X)}{\partial X} + \hat{\theta}\right) \tag{5.1}$$

where D_0 is a characteristic diffusivity, X is the composition, $\mathcal{F}$ is Faraday's constant, R is the gas constant, T is the absolute temperature, $V(X)$ is the composition-dependent open-circuit voltage, and $\hat{\theta}$ is a dimensionless chemomechanical coupling parameter that quantifies the effect of stress-driven diffusion and is given as

$$\hat{\theta} = \frac{2\Omega^2 E c_{\max}}{9RT(1-\nu)} \tag{5.2}$$

where Ω is the partial molar volume of the intercalating species ($\mathrm{cm}^3/\mathrm{mol}$), E is the Young's elastic modulus (GPa), ν is the Poisson's ratio (dimensionless), $c_{\max}$ is the maximum concentration ($\mathrm{mol}/\mathrm{m}^3$).

5.2.1 Moving Phase Boundary Problem

In phase-transforming electrode materials (*i.e.* those with limited solid solubility), this generalized diffusion equation applies to each phase individually. Under conditions of two-phase coexistence, the interface between the coexisting phases must be tracked to determine the global composition field. Such multi-phase kinetic problems can be modeled with sharp-interface theories in which the interface is tracked explicitly, or with diffuse-interface theories in which the interface is tracked implicitly [132].

Here, we adopt a spherical core-shell model in the sharp-interface limit. For three-dimensional diffusing materials such as $\mathrm{Li}_X\mathrm{Mn}_2\mathrm{O}_4$, and for particles on the micron-scale, a

core-shell model is a reasonable geometric assumption. Initially, we solve the single-phase diffusion problem using Equation 5.2 until the surface composition reaches the solubility limit $X(r_{\max}, t) = X_\alpha$. Then, the second phase emerges as a shell. While there are two coexisting phases in the particle, we track the composition field in each phase and the position of the interface $h(t)$. The two-phase core-shell model and a corresponding composition profile are shown schematically in Figure 5-1.

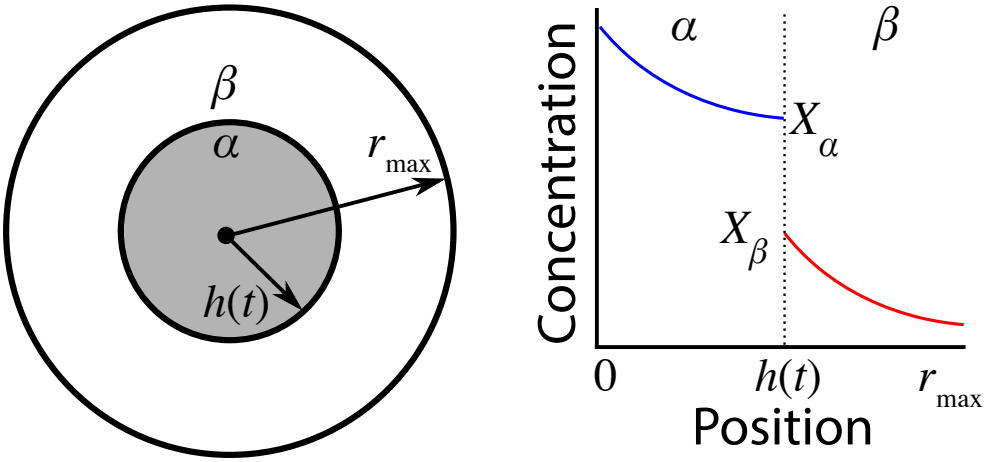

Figure 5-1: The assumed core-shell geometry for two-phase coexistence and schematic concentration profiles corresponding to that geometry.

We assume that the motion of the interface is diffusion-limited and that the compositions at the interface are in local equilibrium. At the interface, $h(t)$, there is a discontinuity in the composition profile $X(r, t)$. Approaching the interface from within either phase, the composition approaches the corresponding equilibrium solubility limit of that phase (Throughout, we refer to the Li-rich phase as α and the Li-poor phase as β)

$$\lim_{r \to h^-} = X_\alpha$$

$$\lim_{r \to h^+} = X_\beta$$

For the model system of $Li_XMn_2O_4$, we take $X_\alpha = 0.5$ and $X_\beta = 0.25$

When the fluxes in each phase are unequal at the interface, the interface must move to conserve mass. Using a control volume around the interface, this mass conservation requirement leads to the Stefan condition [158] which we use to compute the interface velocity $\frac{dh}{dt}$

$$[X_\beta - X_\alpha]\frac{dh}{dt} = \left[\tilde{D}(X_\alpha)\frac{\partial X}{\partial r}|_{r\to h^-} - \tilde{D}(X_\beta)\frac{\partial X}{\partial r}|_{r\to h^+}\right]$$

We discretize and solve the moving phase boundary problem using a strategy similar to that of Zhou and North, in which the interface position is tracked between finite difference grid points [159].

5.2.2 Elastic Stress Distributions

The elastic stress distributions are determined by solving a linear-elastic boundary value problem analogous to the calculation of thermal stresses [86]. Assuming isotropic linear elasticity and traction-free boundaries, the radial and tangential stress profiles are given by

$$\sigma_r(r,t) = \frac{2\Omega E c_{\max}}{9(1-\nu)}\left[X_{av}(r_{\max},t) - X_{av}(r,t)\right]$$
$$\sigma_\theta(r,t) = \frac{\Omega E c_{\max}}{9(1-\nu)}\left[2X_{av}(r_{\max},t) + X_{av}(r,t) - 3X(r,t)\right]$$

$X_{av}(r,t)$ is the average composition within a sphere of radius r, calculated as

$$X_{av}(r,t) = \frac{3}{r^3}\int_0^r X(r,t)r^2\mathrm{d}r$$

These expressions are valid for both single-phase and two-phase configurations, assuming that Ω and E are composition-independent.

5.2.3 Stress-Intensity Factors

The stress-intensity factor is estimated following the approach of Mattheck [88] using the integral equation

$$K_{\mathrm{I}} = \frac{E}{K_{\mathrm{ref}}(1-\nu^2)} \int_0^a \sigma_\theta(x) m(x,a) \mathrm{d}x$$

where K_{ref} is a reference stress intensity factor and $m(x,a)$ is the weight function (a kernel or Green's function) against which the diffusion-induced stress profile is integrated.

5.2.4 Non-Dimensionalizing

All numerical simulations are performed with dimensionless variables. The particle radius, time, interface position, flaw size, and the stress-intensity factor are cast in the following dimensionless forms:

$$\hat{r} = \frac{r}{r_{\max}} \qquad \hat{t} = \frac{tD_0}{r_{\max}^2} \qquad \hat{h} = \frac{h}{r_{\max}} \qquad \hat{a} = \frac{a}{r_{\max}} \qquad \hat{K}_{\mathrm{I}} = \frac{9(1-\nu)K_{\mathrm{I}}}{c_{\max}\Omega E\sqrt{r_{\max}}}$$

The boundary conditions for constant-current charging of a spherical particle are zero flux at the particle center and constant flux at the particle surface. In the dimensionless variables, the boundary conditions are

$$\left.\frac{\partial X}{\partial \hat{r}}\right|_{\hat{r}=0} = 0 \qquad\qquad \left.\frac{\partial X}{\partial \hat{r}}\right|_{\hat{r}=1} = -\frac{\hat{I}}{\tilde{D}(X|_{\hat{r}=1})}$$

with the surface flux specified as a dimensionless current $\hat{I}$

$$\hat{I} = \frac{(\text{C-Rate})\alpha\rho r_{\max}^2}{3D_0 c_{\max}\mathcal{F}}$$

where α is the theoretical specific capacity (Ah/kg) and ρ is the mass density (kg/m^3).

5.2.5 $Li_XMn_2O_4$ as a Model System

$Li_XMn_2O_4$ is a well-known electrode material which is an ideal model system for the present study. First, this material has complex phase-behavior: in the typical 4 V electrochemical cycling window ($0.2 \leq X \leq 0.995$), there are both single phase regions and a region of two-phase coexistence. While $Li_XMn_2O_4$ remains cubic throughout this range of lithium composition, it does not form a continuous solid-solution in the 4 V cycling region, a common misperception [47, 58, 59, 1]. Indeed, the present results show that even cubic-to-cubic phase transformations, which have an isotropic strain, can be highly damaging. Upon initial delithiation, there is a region of continuous solid-solution $0.5 \leq X \leq 0.995$ followed by two-phase coexistence for compositions $0.5 \leq X \leq 0.25$ and finally a second single-phase for compositions $0.25 \leq X \leq 0.20$. This complex phase-behavior demands that concentration-gradient and two-phase-coherency stresses must be treated concurrently to obtain an accurate description of this material.

Second, this material has a highly non-ideal open-circuit voltage, which means that it has a non-trivial concentration-dependent chemical diffusivity. Third, many physical properties of this material have been experimentally measured, enabling a quantitative description with few free parameters. Table 5.1 summarizes the materials properties of $Li_XMn_2O_4$ used in this study. We assume the fracture toughness of $Li_XMn_2O_4$ is 1 MPa$\cdot$m$^{1/2}$, which is similar to that of $LiCoO_2$ [79].

To quantify the composition-dependent chemical diffusivity using Equation 5.1, we need a functional form of the open circuit voltage $V(X)$ of $Li_XMn_2O_4$ and values for the characteristic diffusivity D_0 and stress-coupling parameter $\hat{\theta}$. The open-circuit voltage is specified using the function fit by Doyle, *et al.* [92], which is given in the Appendix as Equation B.36 and is plotted in Figure 5-2(a). The lower 4.0 V region is a single phase of continuously varying composition, $0.5 \leq X \leq 0.995$. The upper 4.1 V plateau is due to two-phase coexistence between the Li-rich phase α, with composition $X_\alpha = 0.5$, and the Li-poor phase β,

with composition $X_\beta = 0.25$.

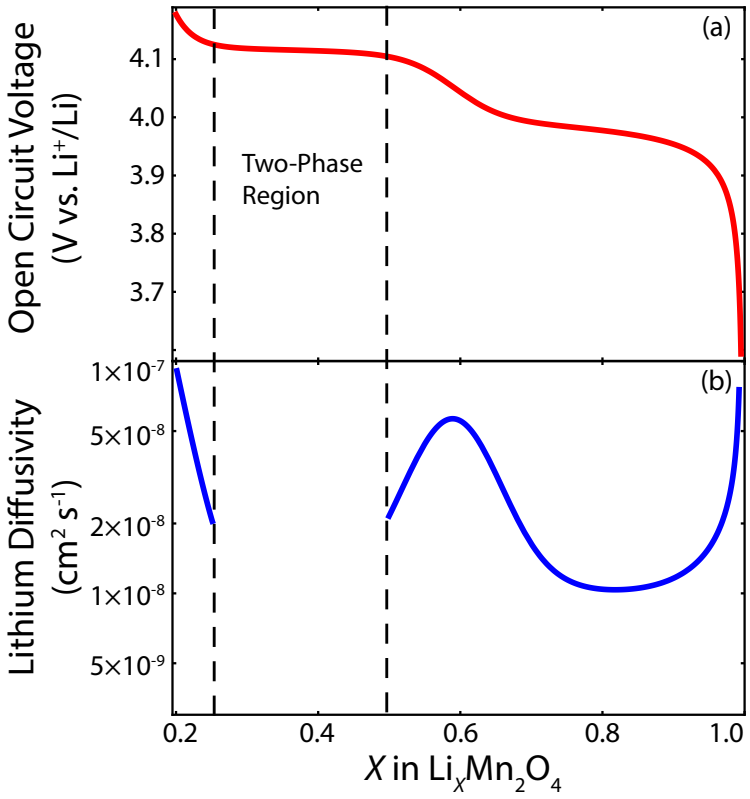

Figure 5-2: (a) Open circuit potential of $\mathrm{Li}_X\mathrm{Mn}_2\mathrm{O}_4$ as given in Ref [92] for $0.2 \leq X \leq 0.995$. (b) Blue solid curve is the thermodynamically-consistent chemical diffusivity of $\mathrm{Li}_X\mathrm{Mn}_2\mathrm{O}_4$ with $D_0 = 6 \times 10^{-9}$ cm^2/s and $\hat{\theta} = 4.57$ plotted according to Equation 5.1. The chemical diffusivity is not defined in the two-phase region, for compositions $0.25 \leq X \leq 0.5$.

Galvanostatic charging (deintercalation) of $\mathrm{Li}_X\mathrm{Mn}_2\mathrm{O}_4$ is simulated in the following way. Particles start with an initial condition of uniform composition near full lithiation, $X(r, t = 0) = 0.995$. We solve the single-phase diffusion equation with the specified surface flux—given as a dimensionless current, $\hat{I}$—until the surface composition reaches the solubility limit of the lithium-rich α phase, X_α. The lithium-poor β phase is then assumed to nucleate as a uniform, infinitesimal shell on the surface of the particle, with composition X_β. Now, the two-phase Stefan problem is solved by simultaneous solution of a diffusion equation in each phase and tracking of the moving boundary. The moving boundary problem is solved until either (1) the surface composition reaches the cutoff composition $X(r_{\max}, t_{\text{end}}) = 0.2$,

Table 5.1: Properties of $Li_XMn_2O_4$ used in numerical calculations. References are given for information taken from or derived from the literature.

Property	**Symbol**	**Units**	**Value**
Young's modulus	E	GPa	143 [78]
Poisson's ratio	ν	-	0.3 [78]
Fracture toughness	K_{Ic}	$\mathrm{MPa{\cdot}m^{1/2}}$	1
Characteristic diffusivity	D_0	$\mathrm{cm^2/s}$	6×10^{-9} [91]
Partial molar volume	Ω	$\mathrm{cm^3/mol}$	3.26 [14]
Maximum concentration	$c_{\max}$	$\mathrm{mol/m^3}$	2.37×10^4 [81]
Density	ρ	$\mathrm{g/cm^3}$	4.28 [81]
Theoretical capacity	α	mAh/g	148 [81]
Temperature	T	K	300

or (2) the moving boundary reaches the particle center $h(t) = 0$. If the surface composition cutoff (condition 1) is reached first, the simulation is terminated. If the interface reaches the particle center (condition 2) first, then we continue solving the single-phase diffusion problem until the cutoff composition is reached at the particle surface and then the simulation is terminated.

5.3 Results and Discussion

First, we compare and contrast the composition distributions that arise during high and low rate charging of an electrode material with complex phase-behavior. Figure 5-3 shows two composition profile 'snapshots' at high ($\hat{I} = 1$) and low ($\hat{I} = 0.05$) dimensionless current. These two dimensionless currents will be used as illustrative examples of high and low charging rates throughout. For both cases, the first snapshot shows the composition profile at time of maximal stress-intensity factor in the single-phase region and the second snapshot shows the composition profile of a two-phase configuration with the interface at position $\hat{h}(t) = 0.85$. The exact time-choices were arbitrary, but the four snapshots highlight

the important similarities and differences among the single-phase and two-phase configurations at high and low charging rates. Comparing the two dimensionless currents, one finds the expected result that increasing dimensionless current produces increasing concentration gradient in each individual phase. Comparing the single- and two-phase configurations, one sees that the two-phase configurations have discontinuous composition profiles, reflecting the underlying miscibility gap. These differences in the composition profiles are manifested in the elastic stress distributions.

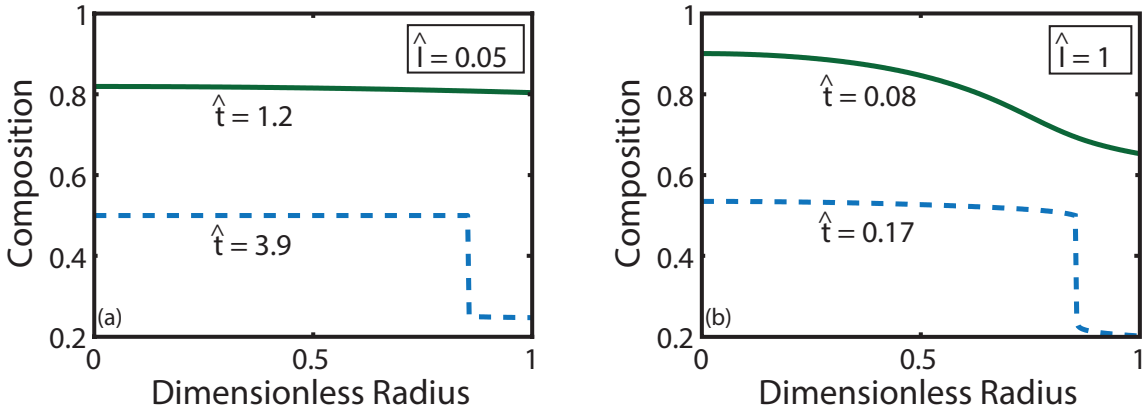

Figure 5-3: Composition profile snapshots for (a) low rate $\hat{I} = 0.05$ and (b) high rate $\hat{I} = 1$ charging. At each charging rate, a representative single-phase and two-phase configuration is shown. The single phase composition profiles snapshots correspond to the maximum stress-intensity factor in the single phase region and the two-phase snapshots are taken when the interface is at $\hat{h}(t) = 0.85$.

While the particles are single-phase, elastic stresses are caused only by composition gradients. Figure 5-4 shows the elastic stress distributions corresponding to the intermediate single-phase configurations at both charging rates. Qualitatively, the single-phase stress distributions have many similarities. In both cases, the particle is traction-free at the surface and the particle core is under hydrostatic compression. The radial stress goes to zero at the particle surface and the tangential stress varies smoothly from tension near the particle surface to compression in the particle center. Quantitatively, however, there are differences between the high- and low-rate stress distributions. The high-rate charge induces more severe

elastic stresses (greater in magnitude both in tension and compression) than the low-rate charge; the peak tensile stress at $\hat{I} = 1$ is fourteen times larger than the peak stress at $\hat{I} = 0.05$.

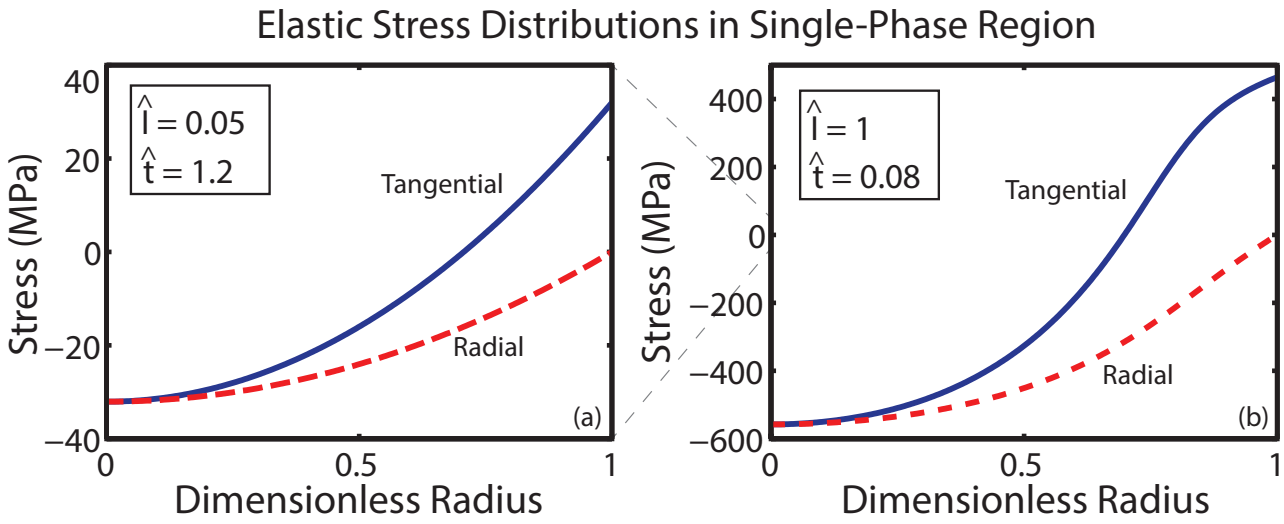

Figure 5-4: Elastic stress distributions in single-phase particles charged at (a) $\hat{I} = 0.05$ and (b) $\hat{I} = 1$. Note the different range of stress levels in the two plots; the dashed gray lines connecting the two plots show this change in scale. Radial stresses, σ_r, are plotted in dashed red and tangential stresses, σ_θ, are plotted in solid blue.

While the particles are two-phase, the elastic stress distributions are dominated by coherency stresses and the two-phase stresses are more severe than the single-phase stresses. Figure 5-5 shows the elastic stress distributions corresponding to the intermediate two-phase configurations at both charging rates. Again, there are many qualitative similarities between the two-phase stress distributions from high- and low-rate charging; these two-phase stress distributions, however, are qualitatively dissimilar from the single-phase stress distributions. In the two-phase particles, the tangential stress is discontinuous at the phase boundary—where the composition has changed discontinuously—jumping from tensile in the shell phase to compressive in the core phase. The radial stress is continuous at the interface, as required for mechanical equilibrium. As the elastic boundary conditions are not changed between the single-phase and two-phase configurations, the particle centers are still under hydrostatic

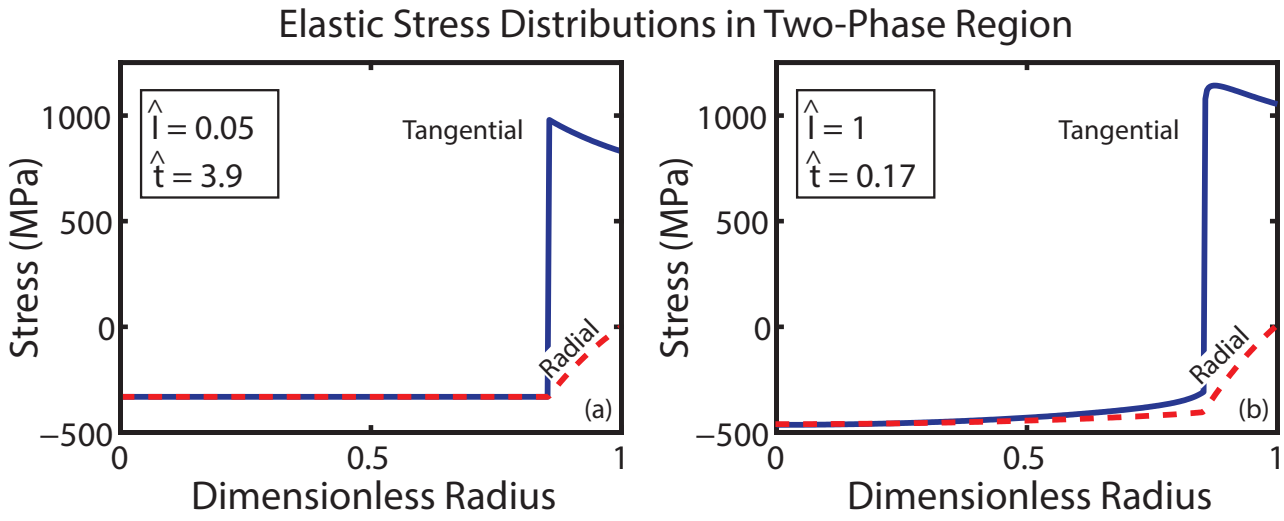

Figure 5-5: Elastic stress distributions in two-phase particles charged at (a) $\hat{I} = 0.05$ and (b) $\hat{I} = 1$. In this figure, the ranges are identical in both plots. Radial stresses, σ_r, are plotted in dashed red and tangential stresses, σ_θ, are plotted in solid blue.

compression and the radial stresses still go to zero at the particle surfaces.

Compared to the single-phase elastic stress distributions, the two-phase stress distributions are remarkably insensitive to the charging rate. Comparing the two-phase configurations with identical interface position, the peak tensile stress at high rate ($\hat{I} = 1$) is only seventeen percent greater than the peak tensile stress at low rate ($\hat{I} = 0.05$). There are, however, some subtle differences in the two-phase elastic stress distributions at low and high charging rates. At low charging rate, the elastic stress distribution is almost pure coherency stress, with very little contribution from concentration gradients. This is evidenced by the nearly hydrostatic stress state in the entire core phase. At high charging rate, there is an additional contribution from concentration gradients in the individual phases and the stress state obtains a deviatoric component; the coherency-stress contributions, however, remain clearly dominant.

To make physical predictions about the possibility of fracture, we quantify the fracture driving force in terms of a stress-intensity factor. The stress-intensity factor takes into account the magnitude of the stresses acting on a crack and the size of the pre-existing

flaw, which serves to intensify those stresses. The stress-intensity factor is a function of flaw size and time: $\hat{K}_{\mathrm{I}} = \hat{K}_{\mathrm{I}}(\hat{a}, \hat{t})$. For self-compensated stress distributions such as those shown in Figures 5-4 and 5-5, the instantaneous stress-intensity factor–flaw size relationships have unique maximum values. Therefore, at any given time, we can use the instantaneous maximum stress-intensity factor as a characteristic descriptor of that state.

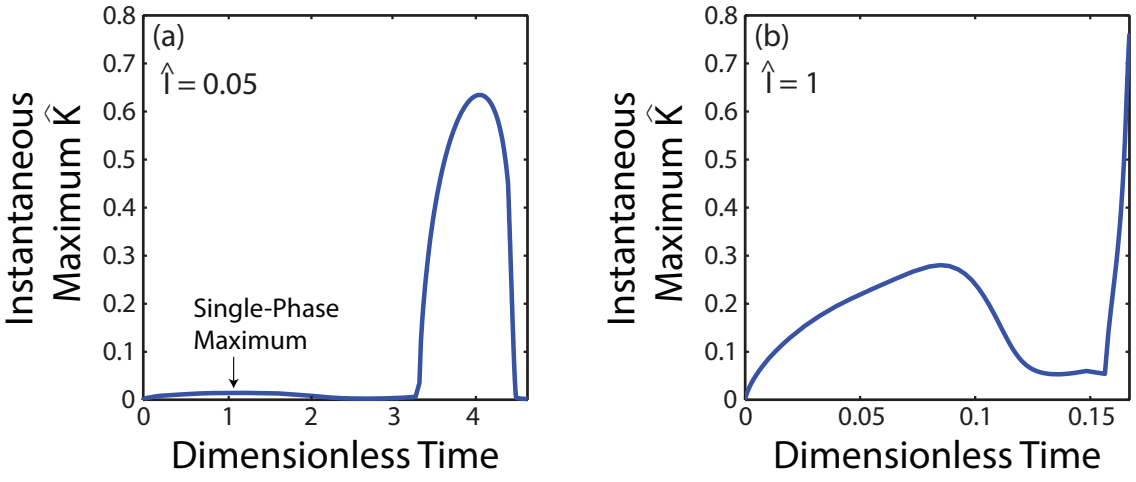

Figure 5-6: Comparison of the time evolution of the maximum instantaneous dimensionless stress-intensity factor for spherical particles charged at a dimensionless currents of $\hat{I} = 0.05$ and 1. In both cases, there is a local maximum in the single-phase region and the magnitude of this maximum increases as the dimensionless current increases. However, the global maximum in both cases occurs in the two-phase region.

For all charging rates presently investigated—spanning two orders-of-magnitude of dimensionless current—the maximum stress-intensity factor always occurs in a two-phase state. Figure 5-6 shows the instantaneous maximum stress-intensity factor as a function of dimensionless time for the low- and high-rate charging with dimensionless currents of $\hat{I} = 0.05$ and $\hat{I} = 1$, respectively. In both cases, there are two local maxima in the instantaneous stress-intensity factor; the first is caused by low chemical diffusivity and the second is caused by two-phase-coherency stresses. The first local maximum occurs when the particle is comprised of a single phase (α), and is due to a spike in the concentration-gradient stresses when the chemical diffusivity is depressed to its minimum value for compositions $0.7 \leq X \leq 0.9$.

The second, global maximum occurs when the particle is two-phase. For the high-rate charge ($\hat{I} = 1$), the stress-intensity factor is still increasing when the charge simulation ends; the terminal surface concentration was hit before the phase boundary reached the particle center. At lower charging rates, the stress-intensity factor peaks and then decays in the two-phase region.

The two-phase maximum occurs due to the tradeoff between magnitude of the elastic stress and size of the affected flaws. Initially, the magnitude of the stress is highest, but it quickly turns from tensile in the shell to compressive in the core, so only very small flaws are substantially affected. When the interface is deep in the particle, very large flaws can be affected, but the tensile stress in the shell is not very large. Most significantly, the stress-intensity factor in the two-phase region is over an order of magnitude larger than in the single-phase region. Thus, we expect that the fracture of these particles is dominated by the two-phase coherency rather than by concentration-gradient stresses.

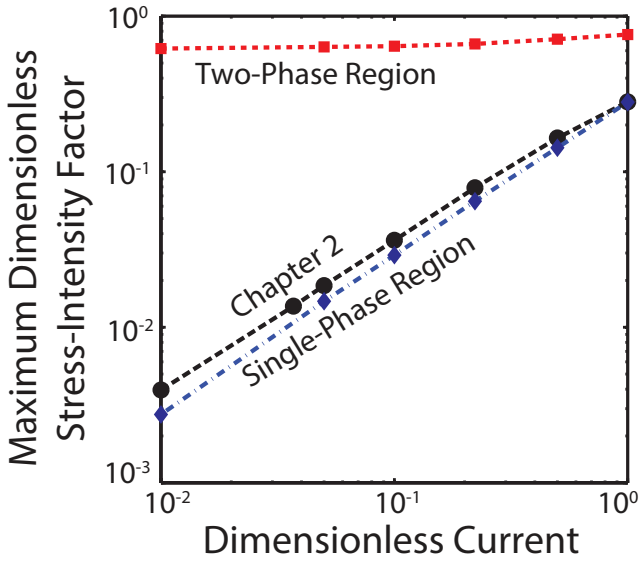

Figure 5-7: Comparison of the maximum dimensionless stress-intensity factors in single-phase and two-phase configurations of spherical particles of $Li_XMn_2O_4$ charged at different dimensionless currents $\hat{I}$. Both axes are logarithmic. Also shown are the dimensionless stress-intensity factors for the simulations from Chapter 2 with $\hat{\theta} = 4.57$ and the open-circuit potential of $Li_XMn_2O_4$.

The same two local maxima—one local single-phase maximum and the global two-phase maximum—are found for every charging rate investigated. As shown in Figure 5-7, the single-phase maxima show a strong linear dependence on the dimensionless current; across the two orders-of-magnitude increase of dimensionless current, the maximum single-phase dimensionless stress-intensity factor increases by a factor of 102. In contrast, the two-phase maxima are nearly insensitive to the charging rate, increasing by only twenty-three percent acrosss the two orders-of-magnitude range of dimensionless current. Even in absolute, rather than relative terms, the increase in the single-phase maximum is greater than the increase in the two-phase maximum.Also shown in Figure 5-7 are the dimensionless stress-intensity factors for a single-phase material with $\hat{\theta} = 4.57$ and the open-circuit voltage of $\mathrm{Li}_X\mathrm{Mn}_2\mathrm{O}_4$, as were determined in Chapter 2. The single-phase maxima in the present study, and the results from Chapter 2 follow nearly identical scaling with increasing dimensionless current.

We construct an electrochemical shock map for $\mathrm{Li}_X\mathrm{Mn}_2\mathrm{O}_4$ which accounts for the complex phase-behavior of this material by restoring dimensions to the data in Figure 5-7; the dimensional electrochemical shock map is shown in Figure 5-8. The electrochemical shock map is a graphical construction which summarizes the critical combinations of particle size and C-Rate which can cause fracture of individual electrode particles [1]. The critical sizes determined from the overall maximum dimensionless stress-intensity factors (those in the two-phase regions) are plotted as the solid red line. The hypothetical single-phase critical sizes, as determined in Chapter 2 are plotted as the dashed black line. *This electrochemical shock map shows that over a wide range of practical particle sizes and C-Rates, fracture of* $\mathrm{Li}_X\mathrm{Mn}_2\mathrm{O}_4$ *is dominated by two-phase-coherency stresses.* Even to C-Rates as high as 1000C, two-phase-coherency stresses are the dominant electrochemical shock mechanism. The critical sizes are plotted here assuming a fracture toughness of $K_{\mathrm{IC}} = 1\ \mathrm{MPa} \cdot \mathrm{m}^{1/2}$, which is similar to the measured fracture toughness of LiCoO_2 [79]. The line for electrochemical cycling through the two-phase region is extrapolated to very low C-Rates, shown as the dashed

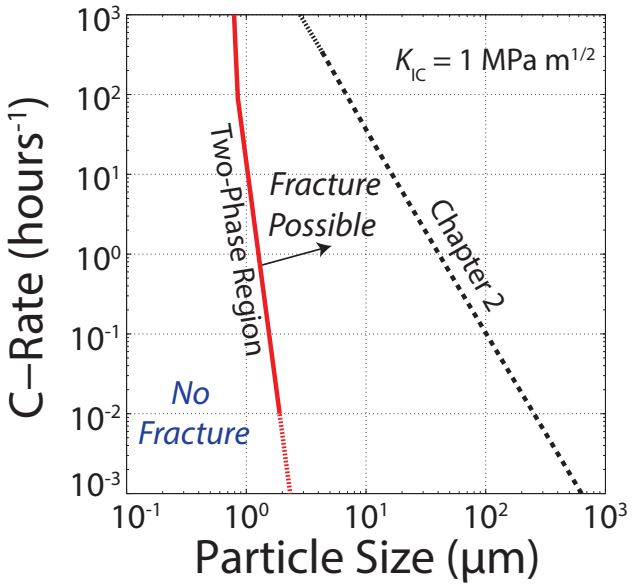

Figure 5-8: Electrochemical shock map for $Li_XMn_2O_4$, accounting for both concentration gradient stresses and coherency stresses, assuming a fracture toughness of $K_{IC} = 1\ MPa{\cdot}m^{1/2}$. Also shown is the hypothetical failure line for a single-phase $Li_XMn_2O_4$-like material, as quantified in Chapter 2. Across a wide range of practical particle sizes and C-Rates, the dominant electrochemical shock mechanism is two-phase coherency stresses, rather than concentration-gradient stresses. Both axes are logarithmic. Both lines are extrapolated beyond the range of parameter space which was explicitly modeled and this is indicated by the fine dashes.

continuation of the solid red line in Figure 5-8 and the line for the single-phase region is extrapolated at very high C-Rates.

Analogous effects may be anticipated in other materials with complex phase-behavior. An obviously analogous system is the high voltage spinel, $Li_XMn_{1.5}Ni_{0.5}O_4$, which is isostructural and has similar transformation strains, in both the ordered and disordered phases. The disordered phase of this material has nearly identical phase-behavior, with a region of solid-solubility followed by two-phase coexistence, while the ordered phase is completely phase-transforming with two regions of two-phase coexistence.

The critical size is strongly sensitive to the magnitude of the transformation strain. In their analysis of Li_XFePO_4 coherency-stress fracture, Hu, *et al.* have noted that the critical size for fracture due to two-phase-coherency stresses scales in proportion to the square of the transformation (misfit) strain, ϵ^2 [72]. Therefore, we anticipate that chemical modifications which reduce the misfit-strain between end-member phases offer a route to dramatic improvements in electrochemical shock resistance. Previous investigations of chemically modified spinel materials, both $Li_XMn_2O_4$ and $Li_XMn_{1.5}Ni_{0.5}O_4$, have demonstrated that substitutions which reduce the misfit strain are effective in limiting capacity fade [160, 41, 122, 43, 123]. We speculate that the reduced driving force for electrochemical shock contributes to the improved cycle-life of these materials.

The core-shell model we have used may not apply to all phase-transforming electrode materials [12, 161]. For equal phase-fractions, a core-shell configuration has much higher elastic energy than a planar interface [12]. Since the spherical core-shell geometry exaggerates the elastic stresses, it is useful to compare to the static (zero-current), two-dimensional finite element calculations of two-phase-coherency stress fracture in a slab-like $Li_XMn_2O_4$ particle with a planar interface from Chapter 4; there, we found a critical particle size of 1.9 μm. Therefore, while the core-shell model exaggerates the stored elastic strain energy compared to a planar interface, the main conclusion that two-phase-coherency stresses dominate the

fracture of $Li_X Mn_2O_4$ is unchanged.

5.4 Conclusions

A kinetic model for electrochemical shock in phase-transforming electrode particles is presented; this model predicts that for micron-sized particles, electrochemical shock is possible in $Li_X Mn_2O_4$, even at vanishly small C-Rates. The model predicts a critical particle size on the order of one micron, below which electrochemical shock can be avoided in this material. For particles larger than this critical size, two-phase-coherency stresses are the dominant electrochemical shock mechanism over a wide range of C-Rates. Two-phase-coherency stresses are an active electrochemical shock mechanism in any lithium storage compound that has a miscibility gap, even cubic materials. As most technologically important lithium storage compounds form non-ideal solutions with single-phase regions and miscibility gaps, this electrochemical shock mechanism is ubiquitous. It is now fair to raise the question: are there any commercially important lithium storage compounds for which C-Rate-dependent electrochemical shock mechanisms are dominant? Although two-phase-coherency stresses may be the dominant electrochemical shock mechansim in many materials, crystal chemical engineering to shrink miscibility gaps and/or to reduce the misfit strains between coexisting phases can be effective to design electrohemical shock resistant materials. Finally, this electrochemical shock mechanism will apply more generally to any intercalation material that undergoes a coherent first-order phase-transformation with varying concentration; the present study focuses on lithium-storage compounds as the best available example of this phenomenon, but it will occur in other ion-intercalation materials such as sodium- and magnesium-intercalation materials.

Chapter 6

Quantifying Reliability Statistics for Electrochemical Shock in Brittle Materials

6.1 Introduction

The mechanical reliability of brittle materials is inherently stochastic and is sensitive to both pre-existing flaw populations—often resulting from processing and fabrication processes—and service conditions. In structural applications, mechanical strength distributions are conventionally described by Weibull statistics, which capture the correct scaling of failure probability with respect to sample size and the applied load. Weibull models are conventionally formulated with a characteristic mechanical stress as the independent variable, but many non-structural applications of brittle materials generate substantial—and microstructurally heterogeneous—stress states, which can drive the materials to mechanical failure. For example, large and heterogeneous stresses can arise from thermal expansion anisotropies, electrochemical cycling-induced compositional changes, and incompatible deformations in

polycrystalline piezoelectric ceramics. In these cases, it may be advantageous to formulate and quantify reliability statistics for in terms of a natural variable for that system: temperature for thermal shock, composition for electrochemical shock, or electric field for piezoelectrics. We present a computational Finite Element plus Monte Carlo (FE+MC) method to quantify reliability statistics in brittle materials subjected to highly heterogeneous stresses, and the reliability statistics are formulated in terms of a natural independent variable for the application at hand.

Several different computational methodologies have been developed to study reliability statistics in brittle materials. Broadly, these previous studies fall into two categories: models that analyze heterogeneous microstructural stresses in materials and models that examine the relationship between flaw size distributions and reliability statistics. The present work combines a microstructurally-resolved elastic analysis with a Monte Carlo study of pre-existing flaws, which enables a general formulation of reliability statistics in brittle materials. Heterogeneous microstructural stresses arise from constrained anisotropic materials, and can be induced by thermal expansion anisotropies [162, 99, 163, 164, 165] or from electrochemically-induced composition changes [166]. Some models of this class have included damage accumulation criteria, with various local failure criteria including a scalar metric of the stress tensor [163, 167, 168, 169], local Weibull statistics [170, 171] or by the use of hybrid elements [165]. In these models, it is necessary to assume a fixed number of pre-existing flaws or flaw nuclei, making it difficult to study the effect of a *distribution* of pre-existing flaws. Other models have specifically studied the relationship between flaw size distributions and reliability statistics under loading conditions where analytical stress solutions are possible, such as flexure or biaxial loading [172, 173, 174]. Many different loading conditions and flaw size distributions have been examined, and there are clear ties between the pre-existing flaw distributions and the resulting reliability statistics in each case.

In this chapter, electrochemical shock is analyzed as a first application of this computa-

tional methodology. The models developed in Chapters 2, 3, and 4 provide microstructure design criteria to avoid electrochemical shock, but these models do not offer any information regarding the degradation of such materials in fracture-possible conditions. Furthermore, it is desirable to develop an understanding of the distribution of likely failure events during electrochemical shock, as it may be more feasible or cost-effective to design lithium-storage materials for a tolerable non-zero level of failure rather than designing for zero failure.

This paper is organized as follows. First, the general methodology of the FE+MC method and the computational details of an initial implementation are described. Second, the method is validated by considering failure under unaxial tension; the FE+MC method reproduces Weibull distributions of failure probability, in close agreement with exact numerical results for this problem. Finally, the FE+MC method is used to study electrochemical shock in polycrsytalline Li_XCoO_2, which involves heterogeneous stress states arising from the anisotropic shape changes which occur as this material is electrochemically cycled. The computed composition-dependent failure probabilities reproduce the key features observed in *in operando* acoustic emission measurements made on polycrystalline Li_XCoO_2 battery electrodes.

6.2 Methods

The most basic idea of the FE+MC method is to combine a finite element elastic stress analysis with a Monte Carlo analysis of failure resulting from a population of flaws with a specified probability distribution of lengths, and which are randomly distributed throughout a microstructure. The general utility of the finite element analysis allows this method to be employed to study reliability statistics for a wide range of structural and non-structural applications. For each hypothetical flaw, the spatially resolved stress distribution information is combined with the flaw size, position, and orientation to estimate a stress-intensity factor

that is compared to the fracture toughness K_{IC} to determine if that flaw will cause failure or not. To estimate failure probabilities, we use repeated trials of the failure analysis with the same sample.

Each virtual microstructure constitutes a sample and it is assumed to contain a specified number of flaws. The specific distribution of flaw sizes, positions, and orientations is varied for each repeated trial on that sample. Each trial, we determine if any of the flaws has a stress-intensity factor exceeding the fracture toughness; if yes, the sample is considered failed, if no, then it is safe. This process is repeated a specified number of times (the number of trials). The failure probability is estimated by the fraction of trials which result in a failure. Different virtual microstructures (samples) are tested to find estimates of the distribution of failure probabilities.

6.2.1 General Methods

In this first report on the FE+MC method, it is useful to distinguish between procedures that any FE+MC implementation should use and the specific computational methods that we have chosen to employ in this intial demonstration. There are three key features that any implementation of the FE+MC method should have. First, virtual microstructures approximating the real microstructure of the material of interest must be obtained. The virtual microstructures can be a digitized representation of a real microstructure, for example obtained from a micrograph, or can be computer-generated. Second, a finite element mesh approximating the virtual microstructure must be prepared that allows a spatially resolved calcuation of the elastic stress distributions in the virtual microstructure. The finite element mesh should allow each grain to have a unique three-dimensional orientation and physical properties such as elastic modulii and Vegard coefficients consistent with crystallographic anisotropies of the desired material. And third, the Monte Carlo analysis should combine the local stress information obtained from the finite element analysis with the size, position,

and orientation of hypothetical flaws which are randomly distributed throughout the microstructure to sample a variety of local environments. The sizes of the randomly generated flaws should be chosen consistenty with an experimental flaw size distribution and the position and orientation of each flaw must be specified. This failure analysis should combine all of the available information to evaluate a physical fracture criterion for each crack.

Any implementation of the FE+MC method should be developed around these general principles. The specific computational methods and tools used to implement the method may vary, depending upon the physical problem of interest and available computational resources. We now describe the details of our initial implementation of the FE+MC method.

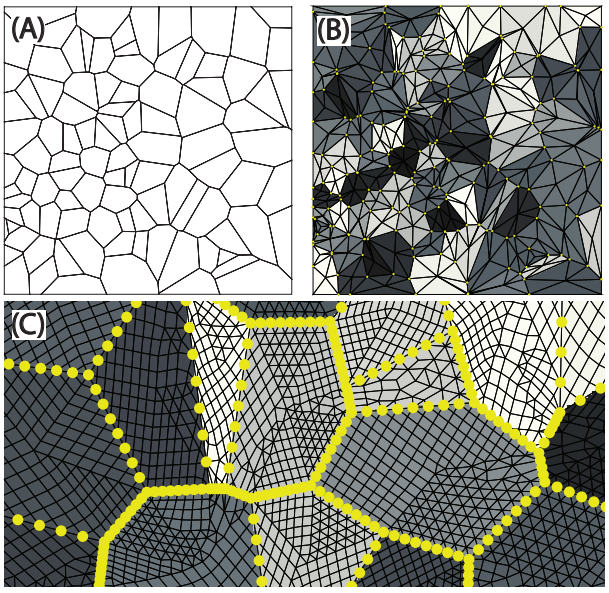

Figure 6-1: (A) An example virtual microstructure of 100 grains generated by a 2-D Voronoi construction with pseudorandom seed points, (B) The initial finite element mesh for the same virtual microstructure which was generated by a simple triangulation of each grain, (C) A portion of the final refined mesh used for actual FEM calculation with the nodes sitting along grain boundaries highlighted. Coloring of grains in (B) and (C) is only to help differentiate between neighboring grains.

6.2.2 Virtual Microstructures

Computer-generated virtual microstructures, obtained by a two-dimensional Voronoi construction using pseudorandom seed points are used throughout this work. An example of one of these microstructures, with 100 grains, is shown in Figure 6-1(A). These computer-generated microstructures are used for easy access to structural information, such as the location of grain boundaries and triple points which are identified and used throughout the process. Each virtual microstructure is generated and its structure characterized in *Mathematica* 8 (Wolfram). Voronoi microstructures with 50, 100, 250, and 500 grains were tested and 100 grains was found sufficient to give well-converged results for the problems studied in this paper. For different physical problems, a greater or lesser number of grains may be required.

6.2.3 Finite Element Calculations

To resolve the elastic stress distributions resulting from the specified duty cycle, an appropriate finite element mesh must be constructed and the resulting boundary value problem solved. This implementation of the FE+MC method uses OOF2 (version 2.1.7), a 2-dimensional finite element tool developed at NIST [124, 125, 126, 127] for finite element calculations. To generate finite element meshes corresponding to our virtual microstructures, we start from a barebones mesh which is a simple triangulation of each grain as shown in Figure 6-1(B). This initial mesh is built in *Mathematica* and is exported along with Python code that automatically drives the refinement of the mesh in OOF2. This automated refinement procedure ensures that any two calculations may be justifiably compared. Figure 6-1(C) shows an example of a fully refined mesh used for the elastic stress analysis. The final refined meshes typically have $\geq$ 46,000 nodes (92,000 degrees of freedom) with 10 nodes along each grain boundary. The Python code also specifies the relevant materials properties—elastic prop-

erties, transformation strains, crystallographic orientation, *etc.*—and boundary conditions and then drives the finite element calculation to completion. The resulting boundary value problems are solved by an iterative conjugate gradient method to a residual error in the displacment field of $\leq 1 \times 10^{-11}$, which typically requires $\sim$ 1500 iterations for the electrochemical shock problems solved here. After solving to a specified error tolerance, the resulting elastic stress distributions are exported for analysis in conjunction with the retained structural information. Figure 6-7(A) shows a filled contour plot of the three in-plane components of stress for an example problem of electrochemically delithiated polycrystalline $\mathrm{Li}_X\mathrm{CoO}_2$ ($X = 0.93$) with the grain network overlaid. Large tensile stresses are shown in red and large compressive stresses in blue.

6.2.4 Monte Carlo over Flaw Distributions

To perform the Monte Carlo analysis over hypothetical flaws, we choose flaws with sizes distributed according to the experimental distribution for surface flaws in glass, as determined by Poloniecki and Wilshaw [175]. This flaw size probability density is empirically fitted as

$$f(a) = \frac{c^{n-1}}{(n-2)!} a^{-n} e^{-c/a} \tag{6.1}$$

where f is the probability density, a is the flaw size, c is a characteristic length scale, and n is a parameter describing the width of the distribution. Figure 6-2 shows this flaw size distribution plotted for three values of n with fixed c. The key features of this distribution are that the most probable flaw size is $a = c/n$ and the tail of the distribution scales as $f \sim a^{-n}$. To generate random flaw sizes consistent with this distribution we generate uniformly distributed random number and invert the corresponding cumulative distribution function to get appropriately distributed flaw sizes.

The objective of the Monte Carlo failure analysis is to sample different stress states in the microstructure, using flaws that are randomly distributed throughout the virtual microstruc-

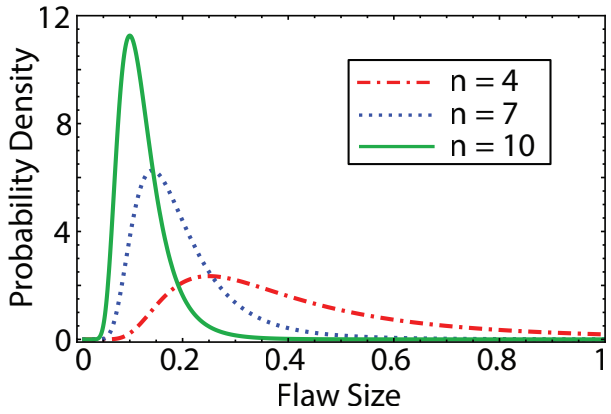

Figure 6-2: The flaw size distribution, shown for $n = 4, 7, 10$, with $c = 1$. The mode flaw size is $a = c/n$ and the breadth of the distribution decreases as n increases.

ture. At present, we limit the position and orientation of flaws by restricting them to lie along the the grain boundaries, and therefore the reliability measures reported here refer strictly to intergranular fracture. With 100 grains, the distribution of grain boundary orientations is nearly uniform. For each flaw, a grain boundary is randomly selected, weighted by the length of the boundaries, and the position along that boundary is randomly determined. To estimate stress-intensity factors for each flaw, we need the local normal stress along the crack. Local normal stress distributions along the grain boundary are extracted by tensor transformation of the laboratory frame stress tensors and fit it to a cubic polynomial (*i.e.* $\sigma_{nn}(s) = a + bs + cs^2 + ds^3$, where s, $0 \leq s \leq 1$, is a parameter which refers to position along a grain boundary) to smooth noise and to speed later calculations of stress-intensity factors. An example of the raw data and the fitted cubic polynomial for one randomly selected grain boundary is shown in Figure 6-7(B) and the selected grain boundary is circled in Figure 6-7(A). Using the polynomial normal stress distribution, the stress-intensity factor for the hypothetical flaw is estimated by a superposition integral method.

6.3 Validation—Uniaxial Tension

To validate the FE+MC method, we first consider failure of brittle materials under uniaxial tension. This problem is useful for validation of our computational method because there is an exact analytical result for the failure probability in terms of loading and flaw distribution, and this exact result is very well approximated by Weibull statistics, which observed experimentally for this loading condition. Figure 6-3 shows a schematic depicting an isotropic material subject to uniaxial tensile loading with a single pre-existing crack, of length $2a$ and inclined to the loading direction by an angle β. Analysis by De S. Jayatilaka and Trustrum shows that for this loading configuration, the Poloniecki flaw distribution (Equation 6.1) leads to a Weibull distribution of failure probabilities [176, 177]. Therefore, under uniform tensile loading, our FE+MC model must predict a Weibull distribution of failure probabilities. We validate the FE+MC method by studying random virtual microstructures subjected to uniform tension and comparing the Weibull modulus obtained from a FE+MC analysis to that obtained from an exact numerical solution of the failure probabilities for different flaw-size distributions.

6.3.1 Analytical Results

For a single pre-existing crack chosen from a flaw-size distribution $f(a)$ and with a random orientation (angle β), the failure probability can be computed as the double integral over orientation and flaw size [176, 177]

$$F(\sigma) = \int_{\frac{K_{\mathrm{IC}}}{\pi\sigma^2}}^{\infty} \left[\int_{\frac{K_{\mathrm{IC}}}{2a\sigma^2}}^{\frac{\pi}{2}} \frac{2}{\pi} f(a) \mathrm{d}\beta \right] \mathrm{d}a \tag{6.2}$$

Given the flaw distribution of Poloniecki and Wilshaw, this double integral can be solved exactly. We evaluated the result analytically using *Mathematica* and found the exact result

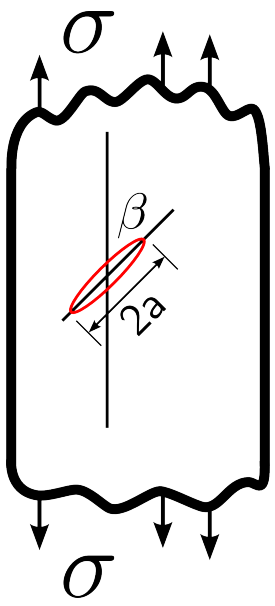

Figure 6-3: Schematic depiction of the sample geometry for the uniaxial tension problem. The flaw has a size of $2a$ and the orientation of the flaw is specified by the angle β.

is

$$F_{\text{exact}}(\sigma) = \frac{\left(\frac{1}{c}\right)^n c^{n-1}\left(c\pi\sigma^2\left[\Gamma(n-1) - \Gamma(n-1, \frac{c\pi\sigma^2}{K_{\text{Ic}}})\right] + K_{\text{Ic}}^2\left[\Gamma(n, \frac{c\pi\sigma^2}{K_{\text{Ic}}}) - \Gamma(n)\right]\right)}{\pi\sigma^2\Gamma(n-1)} \tag{6.3}$$

where $\Gamma(z) = \int_0^\infty t^{z-1}e^{-t}\mathrm{d}t$ is the Euler gamma function and $\Gamma(z,a) = \int_a^\infty t^{z-1}e^{-t}\mathrm{d}t$ is the incomplete gamma function.

Using this single crack failure probability distribution function $F(\sigma)$, the many-crack failure probability $P(\sigma)$ for a body containing N cracks is

$$P(\sigma) = 1 - (1 - F(\sigma))^N \tag{6.4}$$

For any desired value of the flaw-distribution width parameter, n, one may numerically evalute Equation 6.3 to determine the exact single-crack failure probability $F_{\text{exact}}(\sigma)$ and then with a specified flaw density N may determine the exact full-sample failure probability $P_{\text{exact}}(\sigma, N)$. We regard these exact failure probabilities as benchmarks to which all approximate methods are compared.

Empirically, failure probabilities for brittle materials subjected to uniaxial tension are well modeled by a 2-parameter Weibull distribution

$$P(\sigma) = 1 - \exp\left[-\left(\frac{\sigma}{\sigma_0}\right)^m\right] \tag{6.5}$$

where σ_0 is the characteristic strength and m is the Weibull modulus. Here, we have taken the scaling with respect to volume into the definition of the characteristic strength. The many-crack failure probability $P_{\text{exact}}(\sigma, N)$ as defined in Equations 6.3-6.4 converges to the form of a Weibull distribution for large flaw densities (large N). With sufficient number of flaws (*i.e.* sufficiently large flaw densities), the Weibull modulus converges and only the characteristic strength changes as a function of the number of cracks.

The Weibull modulus is often estimated from experimental failure data using a Weibull plot, which yields the Weibull modulus m as the slope of the line

$$\log\left(\log\left(\frac{1}{1-P}\right)\right) = m\log\sigma - m\log\sigma_0 \tag{6.6}$$

We apply this same approach to the exact failure probabilites, fitting the stress-failure data to a Weibull function for flaw distribution width parameters of $n = 3, 5, 7, \text{and } 9$. For each value of n, we compute an associated Weibull modulus m. These benchmark Weibull modulus values are plotted as filled blue points in Figure 6-4. These data points have a line of best fit with the equation $m = 1.36n + 0.12$ and this line is drawn as the solid blue line.

6.3.2 FE+MC Results

To validate the FE+MC procedure, we analyzed the problem of uniaxial tension using the same flaw-distribution width parameter of $n = 3, 5, 7, \text{and } 9$. The results from 100 grain Voronoi microstructures are reported; tests with 250 and 500 grain virtual microstructures did not appreciably change the mean Weibull modulus estimates. The mode flaw size c/n was held constant for all trials. At least 50 samples were tested for each value of the flaw-

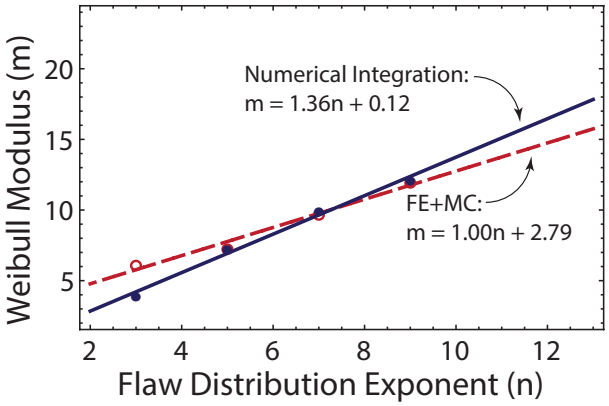

Figure 6-4: Summary of the Weibull modulus results used to validate the FE+MC method. The exact numerical integration results are shown by the filled blue points and the FE+MC results are shown by the open red points. The line of best fit for each method is shown with the equation printed in the Figure.

distribution width parameter n, the reported Weibull modulus is the mean value of pool of samples. For each sample, 300 trials are used to estimate the Weibull modulus.

The Weibull modulus for each sample is estimated using a typical experimental data analysis procedure. For each sample, 300 trials with the same virtual microstructure are performed, each with $N = 1000$ randomly generated and distributed flaws. For this linear problem, the failure strength σ_f of a given trial is determined as the applied stress at which the first crack in the sample obtains a stress-intensity factor equal to the fracture toughness, $K_{\mathrm{I}} = K_{\mathrm{IC}}$. The trials are ranked in order of ascending failiure strength and the failure probability is estimated from this rank order, $p_i = \frac{i-0.5}{M}$ where i is the rank and $M = 300$ (the number of trials). However, this failure probability estimator is not accurate as $p \to 0$ and $p \to 1$; the weighted least squares method due to Bergman [178], which weights trials with intermediate ranks more heavily, is used to extract more accurate Weibull modulii. Each trial is weighted as

$$W = A\left[(1-p)\ln(1-p)\right]^2 \tag{6.7}$$

and A is a sale factor chosen so that W takes a maximum value equal to unity. (A $\simeq 0.14$). This weight function is plotted as the inset in Figure 6-5(A). The maximum weight occurs

at $p \simeq 0.63$.

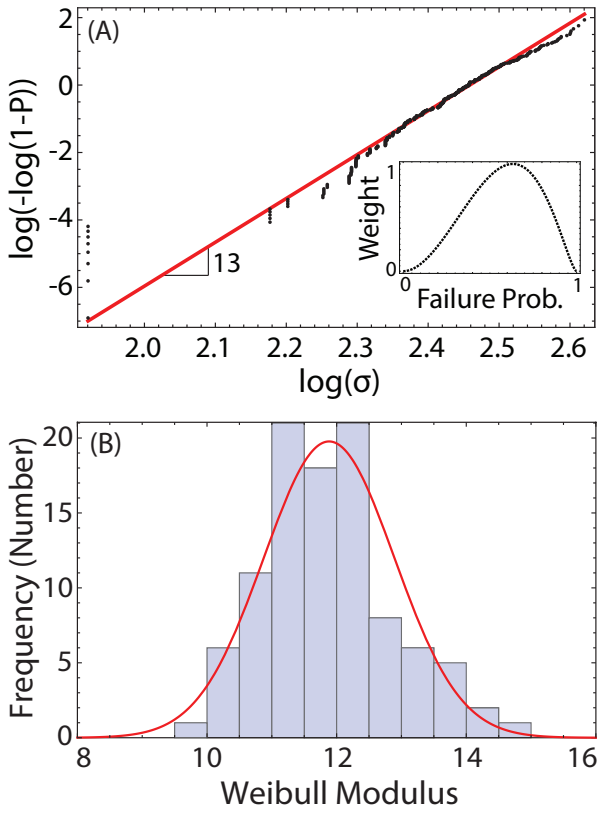

Figure 6-5: (A) An example Weibull plot for a single FE+MC sample with 300 trials and with $n = 9$, $N = 1000$, and 100 grains, showing the Weibull modulus (slope) of 13; (inset) The weight factor used in estimating Weibull modulus; (B) A histogram showing the distribution of the Monte Carlo estimated Weibull modulus for flaw distribution modulus $n = 9$, $N = 1000$ for 100 samples (different virtual microstructures) of the analysis with overlaid normal distribution. The mean Weibull modulus is 11.9 and the standard deviation is 1.0.

Figure 6-5(A) shows a Weibull plot used to extract the Weibull modulus for one sample with a flaw distribution width parameter of $n = 9$, showing the fitted Weibull modulus is $m \approx 13$. Each point in the figure represents one of the 300 trials, each of which used $N = 1000$ flaws. While there are many parameters which must be checked for convergence, the number of flaws in each trial is the most sensitive for convergence; it is necessary to sample adequately from the tail of the flaw size distribution. For all of the values of the flaw distribution width parameter here tested, $N = 1000$ gave converged values of the Weibull

modulus. For larger values of n, a greater number of flaws may be required.

The histogram in Figure 6-5(B) shows the distribution of fitted Weibull modulus for 100 samples with the flaw distribution width parameter of $n = 9$. These data are reasonably approximated by a normal distribution, with a mean of 11.9 and a standard deviation of 1.0. Across the range of n values tested, we found coefficients of variation (standard deviation/mean) in the Weibull modulus of 10-15%.

Figure 6-4 compares the FE+MC results to our benchmark results from the direct numerical integration of the exact failure probabilities. The mean FE+MC Weibull modulii are plotted as the open red data points, and the line of best fit to the FE+MC results is $m = 1.30n + 0.39$; this is plotted as the dashed red line. The FE+MC results are in almost perfect agreement with the exact results for flaw distribution width parameters of $n = 5, 7,$ and 9. For the very wide flaw distribution with $n = 3$, the FE+MC method overestimates the Weibull modulus. However, the exact results show that this very wide flaw distribution yields a very low Weibull modulus of $m \approxeq 3.5$, which is very small for engineered ceramic materials. Thus, the FE+MC method may be confidently applied for most modern ceramic materials with Weibull modulus $m \geq 6$.

6.4 Application to Electrochemical Shock

The FE+MC method is particularly useful for non-structural applications of brittle materials where heterogeneous stress distributions are generated. One such application arises during the electrochemical cycling of lithium-storage materials in lithium-ion batteries. While large composition changes are needed to achieve high storage capacity, these composition changes are often accompanied by large shape changes, which can cause fracture of the lithium-storage materials. Such electrochemical cycling induced fracture—"electrochemical shock"—is an active degradation mechanism in lithium-ion batteries.

There are several mechanisms which can cause electrochemical shock of lithium-storage materials, including concentration gradients during high-rate cycling [1, 179], coherent phase transformations with misfit strains [72, 45] and anisotropic shape changes in polycrystalline materials [45]. We have shown with micromechanical modeling and experimental acoustic emission measurements that polycrystalline Li_XCoO_2 is subject to grain boundary microfracture [45]. Li_XCoO_2 adopts the α-$NaFeO_2$ crystal structure in the $R\bar{3}m$ space group and the lattice parameter changes with varying lithium composition X are dramatically different along the a- and c-axis directions [7]. This is mechanism for electrochemical shock is analagous to thermal shock microfracture in anisotropic refractory materials such as aluminum titantate (Al_2TiO_5).

Previously, we have estimated the grain size below which grain boundary microfracture is impossible for Li_XCoO_2 and several isostructural lithium-stroage compounds [45]. This calculation used an analytical stress analysis of a four-grain ensemble with the grains oriented in a worst-case arrangment, to maximize the driving force for the growth of a pre-existing crack at the quadruple junction. [100]. This worst-case scenario provides a lower bound on the critical grain size, below which it is unfavorable for any pre-existing crack to grow.

While this critical grain size provides a useful design criterion, this model does not offer any information regarding the degradation of polycrystalline lithium storage materials with grain sizes larger than this critical size. Furthermore, it is necessary to develop an understanding of the distribution of likely failure events during electrochemical shock, as it may be more feasible or cost-effective to design lithium-storage materials for a tolerable non-zero level of failure rather than designing for zero failure.

First, it is helpful to review the observations from acoustic emission measurements of damage accumulation due to electrochemical shock in polycrstyalline Li_XCoO_2 electrode materials. Figure 6-6 shows acoustic emission data for a Li_XCoO_2 monolithic electrode cycled at slow rate of C/20. Details of the experimental method are reported elsewhere [45].

The cell voltage is plotted as the blue dashed line, on the left axis and the cumulative acoustic emission counts—a measure of accumulated damage—is plotted as the red solid line on the right axis. There is an initial range of compositions over which almost no damage is accumulated, extending into the two-phase region. Damage begins to accumulate in the two-phase region and accumulates continuously through to the end of the cycle.

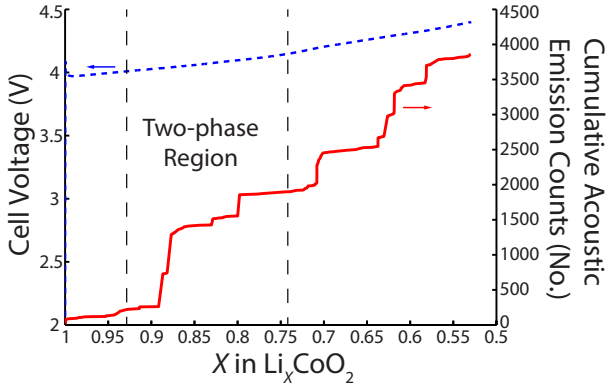

Figure 6-6: Acoustic emission data collected for a Li_XCoO_2 electrode electrochemically cycled in a lithium half-cell. The monolithic polycrystalline Li_XCoO_2 electrode is 760 μm thick and was pressed to 5/8 inch diameter before sintering. The electrode is charged at a C/20 (20h for full charge) rate to a cutoff voltage of 4.4 V vs. Li^+/Li in a 2016 coin cell.

The Li_XCoO_2 used in this experiment has a typical grain size of 3-5 μm, well above the critical grain size for microfracture (for a composition of $X = 0.50$) of 0.42 μm. Therefore, the observed damage accumulation is expected. We seek now to use the FE+MC method to better understand the damage accumulation observed in these experimental measurements.

The elastic boundary value problem is modeled for 100 grain two-dimensional Voronoi microstructures. Each grain is assigned a random crystallographic orientation and a stress-free strain corresponding to its lattice parameter change relative to a composition of $X = 1.0$. The composition-dependent lattice parameters are taken from from X-ray diffraction measurements [7]. The boundaries are assumed to be traction-free and a plane strain condition is applied to simulate the third dimension. We use the available experimentally measured elastic and fracture properties for $LiCoO_2$; Young's modulus of 174 GPa, Poisson ratio of

0.3, and fracture toughness $K_{IC} = 1$ MPa $m^{1/2}$ [79].

Figure 6-7(A) shows filled contour plots of the three in-plane components of elastic stress distribution for a hypothetical microstructure of Li_XCoO_2 with $X = 0.93$ and an average grain size of $\sim$3 μm. In the figures, $\hat{x}$ is horizontal and $\hat{y}$ is vertical. The highly tensile regions are colored in red and highly compressive regions in blue. The figures show that the elastic stresses are singular near grain boundaries and junctions.

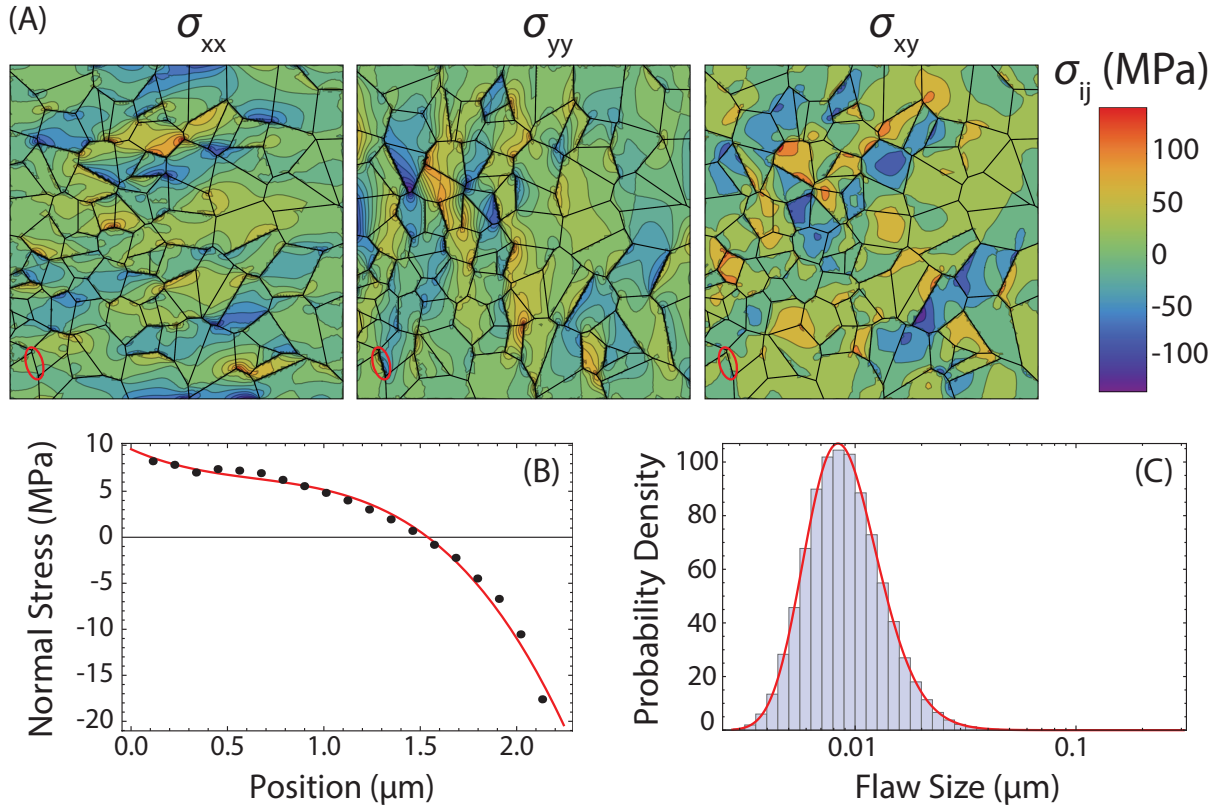

Figure 6-7: (A) Heat maps of the three in-plane stress components for a hypothetical microstructure of Li_XCoO_2 with $X = 0.93$. With $\hat{x}$ horizontal and $\hat{y}$ vertical; (B) Example of a polynomial fit to calculated normal stress along a grain boundary. Line is the third-order polynomial, points are the extracted data; (C) A probability density histogram of 100,000 randomly generated flaws with $c = 0.032$ μm and $n = 7$ with the the theoretical flaw size distribution overlaid. The flaw size axis is logarithmic.

To match the experimental microstructures as closely as possible, the virtual microstructure is assigned an average grain size of $\sim$3 μm. The flaw size distribution used for all of

these trials has $n = 7$ (corresponding to a Weibull modulus of $m \approx 10$, a reasonable value for a modern ceramic) and a characteristic flaw size of $c = 0.032$ μm, approximately one one-hundredth of the grain size. Each trial uses $N = 1000$ hypothetical flaws for the Monte Carlo analysis, the same flaw density as used in validation tests. At each composition, 20,000 trials are performed to estimate the failure probability. The FE+MC analysis is performed on 12 samples to provide some insight on the distribution of composition-dependent failure probabilities.

As Li_XCoO_2 has a miscibility gap for compositions $0.93 \geq X \geq 0.74$, we must develop a strategy to analyze compositions inside the two-phase region [7]. Three compositions inside the two-phase region are tested for each sample. In each two-phase configuration, individual grains are homogenously single-phase, but the phase assigned to that grain is randomly selected. The three composition points are generated by assigning 25, 50, and 75% of the grains to transform to the β-phase with a limiting composition of $X = 0.74$, as shown in Figure 6-8. The actual volume fractions of the two phases are calculated from the area fraction of the grains assigned to that phase. A one-dimensional weighting is applied to the random grain selection to induce a composition gradient in that direction.

Figure 6-9 shows the FE+MC composition-dependent failure probability estimates for each of the twelve unique samples we tested. For some—but not all—of these samples, there is a non-zero failure probability starting in the two-phase region, from a composition around $X \sim 0.88$. This incubation period and the composition of initial damage accumulation is in excellent agreement with the experimental observations of Figure 6-6. The experimental data shows a jump in damage for compositions $X \leq 0.90$. For all samples, the failure probability becomes non-zero, and grows monotonically with decreasing lithium composiiton for compositions $0.74 \leq X \leq 0.50$.

Using the sample with the greatest failure probability at a composition of $X = 0.50$ tested here, it is possible to determine the grain size below which no microfracture would

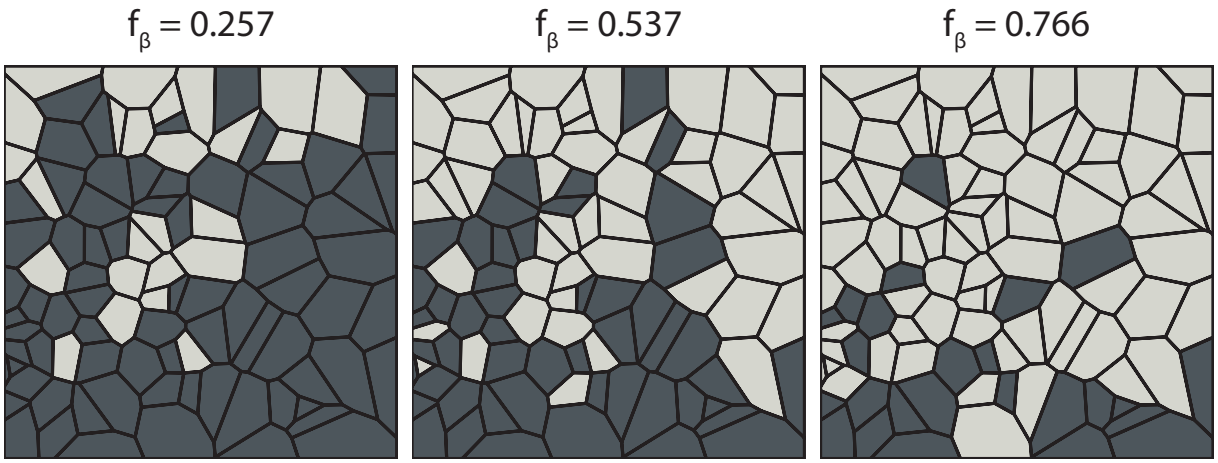

Figure 6-8: Our approximate method to handling the two-phase region. Assign each grain to be homogeneously single phase, but randomly select which grains are in each phase. For each sample, choose three points in the two-phase region, with 25, 50, and 75 % of grains assigned to the β (Li-poor, $X = 0.74$) phase. Weight the random selection of grains by the y position of the seed point to induce a composition gradient. Calculate the actual phase fraction from the area fraction. Li-rich phase is darker, Li-poor phase is lighter.

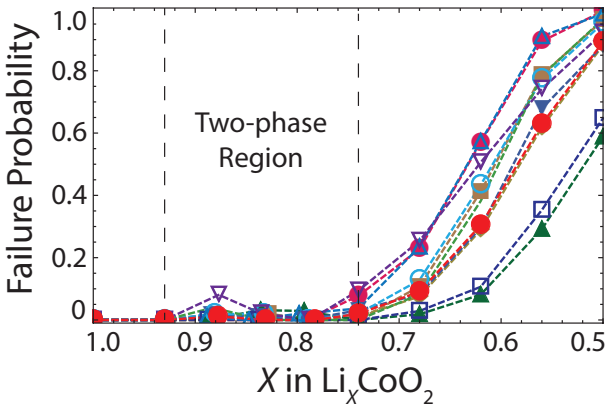

Figure 6-9: Summary of the composition-dependent FE+MC failure probability estimates for delithiation of polycrystalline Li_XCoO_2. Results for twelve different samples (virtual microstructures) are shown. Points are the calculations and lines connect the calculations for the same microstructure. The flaw distribution had a width parameter of $n = 7$ and a characteristic flaw size of $c = 0.032$ μm. Each trial used $N = 1000$ flaws and the failure probability at each point is estimated from 20,000 trials.

be observed. That is, we ask the question: what grain size is necessary to make the failure probability at $X = 0.50$ go to zero for all of the samples? This grain size is found to be 0.68 μm, in very good agreement with the conservative estimate of 0.42 μm from the four-grain, worst-case scenario model [45].

Insights gained from the analytical modeling show that the anisotropy of the shape change is the principal factor in driving this grain boundary microfracture of Li_XCoO_2. To test the role of anisotropy, we performed FE+MC calculations on three samples with the same virtual microstructures, elastic properties, and boundary conditions, but with the shape change set to isotropic and equal to the volume change for Li_XCoO_2 at the same composition. In these three samples, we found failure probabilities identically zero at all compositions, validating the conclusion anisotropy is the key driver of fracture. These results further suggest that even in the two-phase region, the anisotropy of the coherency strain drives electrochemical shock.

6.5 Discussion

In summary, we have developed a Finite Element + Monte Carlo (FE+MC) method to quantify reliability statistics of brittle materials. This method is particularly useful for studying non-structural applications which induce heterogeneous stress distributions. The FE+MC method allows reliability statistics to be formulated in terms of variables that are natural for the material and application of interest. This method is stochastic, microstructurally resolved, and explicitly considers pre-existing flaw distributions.

We have validated the FE+MC method using exact results for uniaxial tensile loading, reproducing the expected scaling of Weibull modulus with respect to flaw distribution parameters. As an initial demonstration of the FE+MC method, we apply it to study electrochemical shock of polycrystalline Li_XCoO_2. Failure probabilities predicted by the FE+MC

method are in excellent agreement with observations from experimental acoustic emission measurements.

The FE+MC method can be applied to study reliability statistics of brittle materials in many other technologically important applications. For example, heterogeneous stress distributions are also commonly encountered in thermal shock of refractory materials and in piezoelectric ceramics. One might apply the FE+MC method to study reliability statistics in these and other non-structural applications. This would enable quantitative estimation of reliability statistics in terms of variable which are natural to that problem, such as temperature or electric field.

Our implementation of the FE+MC method could be extended in many directions. Instead of computer-generated virtual microstructures, one could implement the method using experimentally determined microstructures (for example scanning electron microscope images with or without orientation information from electron backscatter diffraction). With experimental microstructures, it will be important to identify co-existing phases and the interfaces between them. One might wish to study the effect of crystallographic texture on reliability statistics, and this could be incorporated by correlating the orientations between adjacent grains. For the specific application of electrochemical shock, it may be desirable to incorporate electrochemical kinetics in the finite element model, which would enable simultaneous treatment of all electrochemical shock mechanisms.

As the FE+MC method may be applied to arbitrary loading conditions, it could be used to enable mechanical proof-testing for non-structural applications. For example, one might combine mechanical reliability tests with a FE+MC analysis to determine the flaw size distribution parameters (n, c, and N) for the material of interest. Then, the fitted flaw distribution information can be used in a FE+MC model that specifies the intended duty cycle. Thus, an acceptable level of failure in the actual duty cycle can be linked to a specified mechanical strength.

6.6 Conclusions

Coupling of finite element elastic analysis with a Monte Carlo fracture analysis—using experimental flaw-size distributions and fracture mechanics failure criteria—enables a general method for quantification of reliability statistics of brittle materials. Further, this methodology allows reliability statistics to be developed in terms of independent variables which are natural to the application, rather than in terms of mechanical variables which may not be externally applied. The initial application of this methodology to electrochemical shock in polycrystalline Li_XCoO_2 gives excellent agreement with damage accumulation as determined from acoustic emission measurements.

Chapter 7

Conclusions: Designing Electrochemical-Shock-Resistant Ion-Intercalation Materials

The mechanisms of electrochemical shock in ion-intercalation materials have been identified, classified, and modeled. In a given material, the active electrochemical shock mechanisms depend on many factors, including phase-behavior, crystal symmetry, microstructure, electrochemical cycling rate (C-Rate), and composition (state-of-charge).

In this concluding chapter, microstructure design criteria and materials selection criteria to mitigate electrochemical shock are provided, based on insights gained from the detailed study of electrochemical shock mechanisms. Most existing ion-intercalation materials are subject to C-Rate-independent electrochemical shock mechanisms, and therefore electrode microstructures must be engineered to avert electrochemical shock. When selecting and engineering new ion-intercalation materials (*i.e.* compositions), materials which are sensitive only to C-Rate-dependent electrochemical shock should be preferred. Finally, avenues of future work, including *fatigue* effects in electrochemical shock are described.

7.1 Microstructure Design Criteria for Existing Materials

Most known ion-intercalation compounds, including Li- and Na-storage compounds have anisotropic shape changes and/or first-order phase-transformations with non-zero transformation strains. In such materials, it is essential to engineer microstructures to avoid the C-Rate-independent electrochemical shock mechanisms.

To design electrochemical shock resistant electrodes, all active electrochemical shock mechanisms in a given material system must be considered, including C-Rate-dependent and C-Rate-independent mechanisms. In Chapter 2, the electrochemical shock map—a graphical tool that shows regimes of failure depending on C-Rate, particle size, and the materials inherent fracture toughness K_{IC}—was introduced. However, as described in Chapters 3 and 4, anisotropic polycrsytalline materials, and materials with first-order phase-transformations are subject to C-Rate-independent electrochemical shock.

The electrochemical shock map construction can be directly extended to incorporate all possible C-Rate-independent fracture mechanisms, as we show schematically in Figure 7-1. Each panel shows a hypothetical electrochemical shock map, presented as a log-log plot of C-Rate against primary crystallite size, for selected combinations of phase behavior and particle microstructure. In each electrochemical shock map, the solid line represents the border between "safe" (no fracture) conditions and conditions where fracture becomes possible and the dotted lines represent metastable extensions of active, but not limiting, electrochemical shock mechanisms. We start with the previously described single particle, solid solution case—detailed in Chapter 2—which is shown here in panel (a). For an equiaxed single crystal particle, the primary crystallite size is equal to the particle size and the electrochemical shock map contains a single downward sloping line quantified by the materials fracture toughness K_{IC}. In single crystal particles of materials with first-order phase-transformations, such as

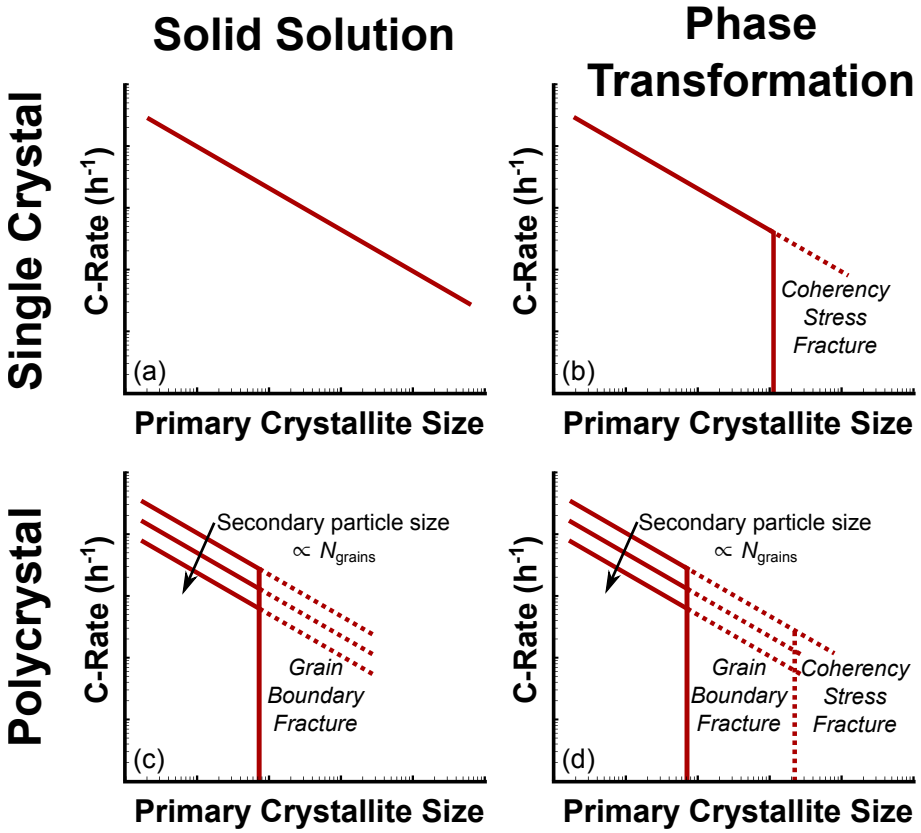

Figure 7-1: Schematic electrochemical shock maps for different combinations of phase behavior (solid solution vs. phase transformation) and particle microstructure (single crystal vs. polycrystalline). Operating conditions that will avoid electrochemical shock degradation are bounded to the top and left by the solid red lines, which is determined by materials properties including Vegard coefficients, ionic diffusivity, elastic and fracture properties.

$Li_XMn_2O_4$, misfit coherency stresses may cause fracture above a material-specific critical crystallite size, as described in Chapter 4. This critical crystallite size is shown as a vertical (C-Rate-independent) line on the electrochemical shock map, as shown in panel (b). For materials with partial miscibility gaps, there is a knee in the failure curve of panel (b) is determined by the competition between C-Rate-dependent concentration-gradient stresses and C-Rate-independent coherency stresses. In a given material, this can be determined using the model presented in Chapter 5; for $Li_XMn_2O_4$, C-Rate-independent coherency stresses dominate for particles greater than $\sim$1 μm and up to C-Rates of $\sim$1000C. For bulk Li_XFePO_4, Li-composition changes are taken up almost entirely by a first-order phase-transformation,

and coherency stresses are the dominant electrochemical shock mechanism. In single crystalline particles of layered materials such as Li_XCoO_2, there are misfitting first-order phase-transformations which can cause fracture of individual crystallites. In the case of dense polycrystalline particles, the secondary (overall) particle size determines the C-Rate dependence of electrochemical shock for the particle. We represent this secondary particle size dependence on the electrochemical shock maps with a family of C-Rate-dependent failure lines, each for a specific secondary particle size, as shown in panels (c) and (d). Equivalently, this family of curves corresponds to secondary particles with equal primary crystallite size, but different numbers of grains (N_{grains}); secondary particles comprised of more grains are susceptible to fracture at lower C-Rates. As documented in Chapter 3, materials with anisotropic Vegard coefficients and polycrystalline microstructures are subject to a different C-Rate-independent electrochemical shock mechanism when the primary crystallite size exceeds a material-specific critical size; this case is shown in panel (c). Using the analytical model presented in Chapter 3, this size can be determined from the composition-dependent lattice parameters and the elastic and fracture properties of the material. Finally, materials with both first-order phase-transformation and polycrystalline microstructure—such as the Li_XCoO_2 considered in Chapter 6—are subject to both C-Rate-independent electrochemical shock mechanisms, as shown in panel (d). In this final case, the degradation mechanism with the smaller critical primary crystallite size limits the available design space. While we have drawn panel (d) for a particular case where grain boundary microfracture dominates (based on our understanding of $LiCoO_2$, NCA, and NMC), it is possible that coherency stress fracture will dominate in other materials systems. These C-Rate-independent electrochemical shock mechanisms provide new critical microstructural length scales that must be considered to rationally design electrochemical shock resistant battery electrodes.

7.2 Materials Selection Criteria for Electrochemical-Shock-Resistance

Insights gained from this thesis provide new materials selection criteria for electrochemical-shock-resistant ion-intercalation materials

In non-cubic materials, it is more important to minimize the principal shear strain (*i.e.* the anisotropy) than to minimize the net volume change. The benefits of such compositional engineering have been realized in Mg-doping in NCA. In phase-transforming materials, the misfit strains drive coherency stresses; therefore, the misfit strains should be minimized. This may be achieved by selecting materials which reduce the transformation strain, or which shrink the miscibility gap. This may be achieved through engineering the size and composition of electrode materials, as has been done in $\mathrm{Li}_X\mathrm{FePO}_4$.

To avoid both of the C-Rate-independent electrochemical shock mechanisms, materials which are cubic and single-phase over the entire composition region in which electrochemical cycling is performed are preferred, such as $\mathrm{Li}_X\mathrm{Fe}_{0.08}\mathrm{Mn}_{1.5}\mathrm{Ni}_{0.42}\mathrm{O}_4$. In this case alone, it is desirable to minimize the total volume change, to reduce the sensitivity to C-Rate-dependent concentration-gradient stresses.

7.3 Future Work

7.3.1 New Materials

One direction for future work is to explore the pseudo-ternary $\mathrm{LiMn}_x\mathrm{Ni}_y\mathrm{Fe}_z\mathrm{O}_4$ ($x+y+z=2$) system to identify the compositions which support single-phase solid-solution electrode materials. In this model system, compositions which optimize energy density while retaining the desired phase-behavior may be identified. Further, the identification of a stable single-phase ion-intercalation material enables experimental testing of the concentration-gradient

mechanism described in Chapter 2.

Many of the design criteria for electrochemical-shock-resistant materials are consonant with existing materials selection criteria for high-performance ion-intercalation materials. The spinel systems, where misfit strains may be compositionally tuned, can connect with previous obversations in olivine materials that strain accomodation promotes facile phase transformation kinetics. A similar effect may be anticipated in the cubic spinel materials, and this can be studied by Potentiostatic Intermittent Tittration Test (PITT) experiments.

7.3.2 Electrochemical Shock Fatigue

This thesis has focused on electrochemical shock during the first electrochemical cycle, using *fracture* analyses. Fatigue may promote mechanical failure if sub-critical cracks (i.e., those having stress-intensity factor less than than the fracture toughness) are present. Cyclic charging and discharging cycles induce cyclic tension and compression, which is known to promote sub-critical crack growth. The rate of sub-critical crack growth is characterized by the empirical relationship known as Paris' Law, expressed as

$$\frac{\mathrm{d}a}{\mathrm{d}N} = C_{\mathrm{Paris}} \cdot \Delta K^{p} \tag{7.1}$$

where C_{Paris} and p are empirical parameters. Repeated cycling causes the initially small crack to grow until its stress-intensity factor reaches the fracture toughness and unstable crack growth—and potentially, terminal failure as was discussed previously—occurs. The method developed in this study can be used to calculate ΔK for different charge-discharge cycles to predict fracture events throughout the life of an intercalation electrode. Experience in fatigue crack growth in brittle materials shows that C_{Paris} and p are sensitive to small changes in environmental conditions. Because the crack tip is an electrochemically active environment, such sensitivity should be expected in the case of electrochemical shock.

Further, the observations of high dislocation densities in certain ion-intercalation materials after cycling suggests that dislocation-mediated deformation may be possible. Analysis of this *electrochemical shock fatigue* problem may help explain observations of continual mechanical degradation—and impedance growth—accumulating over extended cycling.

THIS PAGE INTENTIONALLY LEFT BLANK

References

[1] William H Woodford, Yet-Ming Chiang, and W. Craig Carter. "Electrochemical Shock" of Intercalation Electrodes: A Fracture Mechanics Analysis. *J Electrochem Soc*, 157(10):A1052–A1059, 2010. 26, 33, 46, 54, 131, 139, 157

[2] V A Sethuraman, V Srinivasan, A F Bower, and P R Guduru. *In Situ* Measurements of Stress-Potential Coupling in Lithiated Silicon. *J Electrochem Soc*, 157(11):A1253–A1261, 2010. 29

[3] D W Hoffman. Concerning The Elastic Free Energy of Dilute Interstitial Alloys. *Acta Metallurgica*, 18(7):819, 1970. 29

[4] S Sinha and D W Murphy. Lithium Intercalation in Cubic TiS_2. *Solid State Ionics*, 20(1):81–84, 1986. 11, 31, 32

[5] Atsuo Yamada, Hiroshi Koizumi, Noriyuki Sonoyama, and Ryoji Kanno. Phase change in Li_XFePO_4. *Electrochem. Solid-State Lett.*, 8(8):A409–A413, 2005. 11, 31, 32

[6] T Ohzuku, M Kitagawa, and T Hirai. Electrochemistry of Manganese-Dioxide in Lithium Nonaqueous Cell. III. X-Ray Diffractional Study on the Reduction of Spinel-Related Manganese-Dioxide. *J Electrochem Soc*, 137(3):769–775, 1990. 11, 31, 32, 34, 125

[7] Jan N Reimers and J R Dahn. Electrochemical and *in situ* X-Ray Diffraction Studies of Lithium Intercalation in Li_XCoO_2. *J Electrochem Soc*, 139(8):2091, 1992. 11, 31, 32, 34, 49, 86, 109, 125, 157, 158, 160

[8] I Saadoune and C Delmas. On the $Li_XNi_{0.8}Co_{0.2}O_2$ system. *Journal of Solid State Chemistry*, 136(1):8–15, 1998. 34

[9] J Shim, R Kostecki, T Richardson, X Song, and KA Striebel. Electrochemical analysis for cycle performance and capacity fading of a lithium-ion battery cycled at elevated temperature. *Journal of Power Sources*, 112(1):222–230, 2002. 34, 36

[10] T Ohzuku, Atsushi Ueda, and M Nagayama. Electrochemistry and Structural Chemistry of $LiNiO_2$ ($R\bar{3}m$) for 4 Volt Secondary Lithium Cells. *J Electrochem Soc*, 140(7):1862–1870, 1993. 34

[11] Won-Sub Yoon, Kyung-Yoon Chung, James McBreen, and Xiao-Qing Yang. A comparative study on structural changes of $LiCo_{1/3}Ni_{1/3}Mn_{1/3}O_2$ and $LiNi_{0.8}Co_{0.15}Al_{0.05}O_2$ during first charge using *in situ* XRD. *Electrochemistry Communications*, 8(8):1257–1262, August 2006. 34, 99, 125

[12] Nonglak Meethong, Hsiao-Ying Shadow Huang, Scott A Speakman, W. Craig Carter, and Yet-Ming Chiang. Strain Accomodation during Phase Transformations in Olivine-Based Cathodes as a Materials Selection Criterion for High-Power Rechargeable Batteries. *Advanced Functional Materials*, 17:1115–1123, 2007. 34, 49, 124, 141

[13] Atsuo Yamada and Sai-Cheong Chung. Crystal Chemistry of the Olivine-Type $Li(Mn_yFe_{1-y})PO_4$ and $Mn_yFe_{1-y}PO_4$ as Possible 4 V Cathode Materials for Lithium Batteries. *J Electrochem Soc*, 2001. 34, 125

[14] J.C. Hunter. Preparation of a new crystal form of manganese dioxide: λ-MnO_2. *Journal of Solid State Chemistry*, 39(2):142–147, 1981. 34, 49, 56, 133

[15] K Ariyoshi, Y Iwakoshi, N Nakayama, and T Ohzuku. Topotactic Two-Phase Reactions of $Li[Ni_{1/2}Mn_{3/2}]O_4$ ($P4_332$) in Nonaqueous Lithium Cells. *J Electrochem Soc*, 151(2):A296–A303, 2004. 34, 125

[16] Rajesh Tripathi, T N Ramesh, Brian L Ellis, and Linda F Nazar. Scalable Synthesis of Tavorite $LiFeSO_4F$ and $NaFeSO_4F$ Cathode Materials. *Angew. Chem. Int. Ed.*, 49(46):8738–8742, October 2010. 34, 35

[17] B L Ellis, TN Ramesh, L.J.M. Davis, G.R. Goward, and Linda F Nazar. Structure and Electrochemistry of Two-Electron Redox Couples in Lithium Metal Fluorophosphates Based on the Tavorite Structure. *Chemistry of Materials*, 2011. 34

[18] T Ohzuku, Y Iwakoshi, and K Sawai. Formation of Lithium-Graphite Intercalation Compounds in Nonaqueous Electrolytes and Their Application as a Negative Electrode for a Lithium Ion (Shuttlecock) Cell. *J Electrochem Soc*, 140(9):2490–2498, 1993. 34, 125

[19] Tsutomu Ohzuku, Atsushi Ueda, and Norihiro Yamamoto. Zero-Strain Insertion Material of $Li[Li_{1/3}Ti_{5/3}]O_4$ for Rechargeable Lithium Cells. *J Electrochem Soc*, 142(5):1431–1435, 1995. 34

[20] LY Beaulieu, KW Eberman, RL Turner, LJ Krause, and J R Dahn. Colossal reversible volume changes in lithium alloys. *Electrochem. Solid-State Lett.*, 4(9):A137–A140, 2001. 34

[21] Kyu Tae Lee, T N Ramesh, F Nan, G Botton, and Linda F Nazar. Topochemical Synthesis of Sodium Metal Phosphate Olivines for Sodium-Ion Batteries. *Chem. Mater.*, 23(16):3593–3600, August 2011. 35

[22] F Sauvage, L Laffont, J M Tarascon, and E. Baudrin. Study of the Insertion/Deinsertion Mechanism of Sodium into $Na_{0.44}MnO_2$. *Inorg. Chem.*, 46(8):3289–3294, April 2007. 35

[23] Brian L Ellis, W R Michael Makahnouk, W N Rowan-Weetaluktuk, D H Ryan, and Linda F Nazar. Crystal Structure and Electrochemical Properties of A_2MPO_4F Fluorophosphates (A = Na, Li; M = Fe, Mn, Co, Ni). *Chem. Mater.*, 22(3):1059–1070, February 2010. 35

[24] Q Huang, M Foo, R Pascal, J Lynn, B Toby, Tao He, H Zandbergen, and R Cava. Coupling between electronic and structural degrees of freedom in the triangular lattice conductor Na_XCoO_2. *Physical Review B*, 70(18), November 2004. 35

[25] Donghan Kim, Sun-Ho Kang, Michael Slater, Shawn Rood, John T Vaughey, Naba Karan, Mahalingam Balasubramanian, and Christopher S Johnson. Enabling Sodium Batteries Using Lithium-Substituted Sodium Layered Transition Metal Oxide Cathodes. *Advanced Energy Materials*, 1(3):333–336, February 2011. 35, 102

[26] C Didier, M Guignard, C Denage, O Szajwaj, S Ito, I Saadoune, J Darriet, and C Delmas. Electrochemical Na-Deintercalation from $NaVO_2$. *Electrochem. Solid-State Lett.*, 14(5):A75, 2011. 35

[27] Haifeng Wang, Young-Il Jang, Biying Huang, Donald R Sadoway, and Yet-Ming Chiang. TEM Study of Electrochemical Cycling-Induced Damage and Disorder in $LiCoO_2$ Cathodes for Rechargeable Lithium Batteries. *J Electrochem Soc*, 146(2):473–480, 1999. 11, 33, 36

[28] GY Chen, XY Song, and TJ Richardson. Electron microscopy study of the $LiFePO_4$ to $FePO_4$ phase transition. *Electrochem. Solid-State Lett.*, 9(6):A295–A298, 2006. 11, 33, 36

[29] Yuichi Itou and Yoshio Ukyo. Performance of $LiNiCoO_2$ materials for advanced lithium-ion batteries. *Journal of Power Sources*, 146(1-2):39–44, August 2005. 11, 33, 36, 79, 80, 99, 101

[30] Young-Il Jang, Biying Huang, Haifeng Wang, Donald R Sadoway, Gerbrand Ceder, Yet-Ming Chiang, Hui Liu, and Hirokazu Tamura. $LiAl_yCo_{1-y}O_2$ ($R\bar{3}m$) Intercalation Cathode for Rechargeable Lithium Batteries. *J Electrochem Soc*, 146(3):862–868, 1999. 33

[31] H Gabrisch, J Wilcox, and M M Doeff. TEM Study of Fracturing in Spherical and Plate-like $LiFePO_4$ Particles. *Electrochem. Solid-State Lett.*, 11(3):A25–A29, 2008. 33

[32] Quinn C Horn and K C White. Understanding Lithium-Ion Degradation and Failure Mechanisms by Cross-Section Analysis. In *211th Meeting of The Electrochemical Socity*, 2007. 33, 36

[33] T Ohzuku, H Tomura, and K Sawai. Monitoring of particle fracture by acoustic emission during charge and discharge of Li/MnO_2 cells. *J Electrochem Soc*, 144(10):3496–3500, October 1997. 33, 94

[34] K Sawai, H Tomura, and T Ohzuku. Acoustic emission histometry for battery material research. *Denki Kagaku*, 66(3):301–307, March 1998. 33, 94

[35] D P H Hasselman. Unified Theory of Thermal Shock Fracture Initiation and Crack Propagation in Brittle Ceramics. *Journal of the American Ceramic Society*, 52(11):600–604, 1969. 33

[36] H A Bahr and H J Weiss. Heuristic approach to thermal shock damage due to single and multiple crack growth. *Theoretical and Applied Fracture Mechanics*, 6(1):57–62, 1986. 33

[37] H A Bahr, G Fischer, and H J Weiss. Thermal-shock crack patterns explained by single and multiple crack propagation. *Journal of Materials Science*, 21:2716–2720, 1986. 33

[38] H A Bahr, H Balke, M Kuna, and H Liesk. Fracture Analysis of a Single Edge Cracked Strip Under Thermal Shock. *Theoretical and Applied Fracture Mechanics*, 8:33–39, 1987. 33

[39] H A Bahr, H J Weiss, H G Maschke, and F Meissner. Multiple Crack Propagation in a Strip Caused by Thermal Shock. *Theoretical and Applied Fracture Mechanics*, 10:219–226, 1988. 33

[40] P Arora, Ralph E White, and M Doyle. Capacity fade mechanisms and side reactions in lithium-ion batteries. *J Electrochem Soc*, 145(10):3647–3667, 1998. 36, 38

[41] Youngjoon Shin and Arumugam Manthiram. Factors Influencing the Capacity Fade of Spinel Lithium Manganese Oxides. *J Electrochem Soc*, 151(2):A204, 2004. 36, 141

[42] Marie Kerlau, Jeffrey A Reimer, and Elton J Cairns. Investigation of particle isolation in Li-ion battery electrodes using ^{7}Li NMR spectroscopy. *Electrochemistry Communications*, 7(12):1249–1251, December 2005. 36

[43] W Choi and Arumugam Manthiram. Superior Capacity Retention Spinel Oxyfluoride Cathodes for Lithium-Ion Batteries. *Electrochem. Solid-State Lett.*, 9(5):A245, 2006. 36, 141

[44] Sandeep Bhattacharya, A Reza Riahi, and Ahmet T Alpas. In-situ observations of lithiation/de-lithiation induced graphite damage during electrochemical cycling. *Scripta Materialia*, 64(2):165–168, January 2011. 36

[45] William H Woodford, W. Craig Carter, and Yet-Ming Chiang. Design criteria for electrochemical shock resistant battery electrodes. *Energy & Environmental Science*, 5:8014–8024, 2012. 37, 89, 157, 162

[46] J Vetter, P Novak, M R Wagner, C Veit, K C Moller, J. O. Besenhard, M Winter, M Wohlfahrt-Mehrens, C Vogler, and A Hammouche. Ageing mechanisms in lithium-ion batteries. *Journal of Power Sources*, 147:269–281, 2005. 38

[47] J Christensen and John C Newman. A Mathematical Model of Stress Generation and Fracture in Lithium Manganese Oxide. *J Electrochem Soc*, 153(6):A1019–A1030, 2006. 38, 39, 41, 75, 125, 131

[48] J Christensen and John C Newman. Stress generation and fracture in lithium insertion materials. *Journal of Sold State Electrochemistry*, 10:293–319, 2006. 38, 39, 75

[49] Yang-Tse Cheng and Mark W Verbrugge. Evolution of stress within a spherical insertion electrode particle under potentiostatic and galvanostatic operation. *Journal of Power Sources*, 190:453–460, 2009. 38, 39, 75

[50] Yang-Tse Cheng and Mark W Verbrugge. Diffusion-Induced Stress, Interfacial Charge Transfer, and Criteria for Avoiding Crack Initiation of Electrode Particles. *J Electrochem Soc*, 157(4):A508–A516, 2010. 38, 40

[51] Yang-Tse Cheng and Mark W Verbrugge. Application of Hasselman's Crack Propagation Model to Insertion Electrodes. *Electrochem. Solid-State Lett.*, 13(9):A128–A131, 2010. 38

[52] A F Bower, P R Guduru, and V A Sethuraman. A finite strain model of stress, diffusion, plastic flow, and electrochemical reactions in a lithium-ion half-cell. *Journal of the Mechanics and Physics of Solids*, 59(4):804–828, April 2011. 38

[53] T K Bhandakkar and Huajian Gao. Cohesive modeling of crack nucleation under diffusion induced stresses in a thin strip: Implications on the critical size for flaw tolerant battery electrodes. *International Journal of Solids and Structures*, 47:1424–1434, 2010. 38

[54] Tanmay K Bhandakkar and Huajian Gao. Cohesive modeling of crack nucleation in a cylindrical electrode under axisymmetric diffusion induced stresses. *International Journal of Solids and Structures*, 48(16-17):2304–2309, August 2011. 38

[55] S Golmon, K Maute, and M L Dunn. Numerical modeling of electrochemical-mechanical interactions in lithium polymer batteries. *Computers and Structures*, 87:1567–1579, 2009. 38, 39

[56] S Golmon, K Maute, S H Lee, and M L Dunn. Stress generation in silicon particles during lithium insertion. *Applied Physics Letters*, 97:033111, 2010. 38

[57] Stephen J Harris, Rutooj D Deshpande, Yue Qi, Indrajit Dutta, and Yang-Tse Cheng. Mesopores inside electrode particles can change the Li-ion transport mechanism and diffusion-induced stress. *J. Mater. Res.*, 25(8):1433–1440, 2010. 38

[58] X Zhang, W Shyy, and A M Sastry. Numerical Simulation of Intercalation-Induced Stress in Li-ion Battery Electrode Particles. *J Electrochem Soc*, 154(10):A910–A916, 2007. 38, 40, 49, 131, 211

[59] X Zhang, A M Sastry, and W Shyy. Intercalation-Induced Stress and Heat Generation within Single Lithium-Ion Battery Cathode Particles. *J Electrochem Soc*, 155(7):A542–A552, 2008. 38, 40, 131

[60] S Kalnaus, K Rhodes, and C Daniel. A study of lithium ion intercalation induced fracture of silicon particles used as anode material in Li-ion battery. *Journal of Power Sources*, pages 1–9, June 2011. 38

[61] R Edwin Garcia, Yet-Ming Chiang, W. Craig Carter, Pimpa Limthongkul, and Catherine M Bishop. Microstructrual Modeling and Design of Rechargeable Lithium-Ion Batteries. *J Electrochem Soc*, 152(1):A255–A263, 2005. 39, 75

[62] Yang-Tse Cheng and Mark W Verbrugge. The influence of surface mechanics on diffusion induced stresses within spherical nanoparticles. *Journal of Applied Physics*, 104:083521, 2008. 39, 75

[63] Mark W Verbrugge and Yang-Tse Cheng. Stress Distribution within Spherical Particles Undergoing Electrochemical Insertion and Extraction. *ECS Transactions*, 16(13):127–139, 2008. 39

[64] S Renganathan, G Sikha, S Santhanagopalan, and Ralph E White. Theoretical Analysis of Stresses in a Lithium Ion Cell. *J Electrochem Soc*, 157(2):A155–A163, 2010. 39, 41, 76, 125

[65] J Christensen. Modeling Diffusion-Induced Stress in Li-Ion Cells with Porous Electrodes. *J Electrochem Soc*, 157(3):A366–A380, 2010. 40, 76

[66] R A Huggins and W D Nix. Decrepitation Model for Capacity Loss During Cycling of Alloys in Rechargeable Electrochemical Systems. *Ionics*, 6:57, 2000. 40, 41

[67] J Wolfenstine. Critical grain size for microcracking during lithium insertion. *Journal of Power Sources*, 79:111–113, 1999. 40, 41

[68] J Wolfenstine, D Foster, J Read, W K Behl, and W Luecke. Experimental confirmation of the model for microcracking duering lithium charging in single-phase alloys. *Journal of Power Sources*, 87:1–3, 2000. 40, 41

[69] K E Aifantis and J P Dempsey. Stable crack growth in nanostructured Li-batteries. *Journal of Power Sources*, 143:203–211, 2005. 40

[70] K E Aifantis, S A Hackney, and J P Dempsey. Design criteria for nanostructured Li-ion batteries. *Journal of Power Sources*, 165:874–879, 2007. 40

[71] Katerina E Aifantis and Stephen A Hackney. Nanoscale Engineering for the Mechanical Integrity of Li-ion Electrode Materials. In Ali Eftekhari, editor, *Nanostructured Materials in Electrochemistry*, pages 319–347. Wiley-VCH, 2008. 40

[72] Yuhuang Hu, Xuanhe Zhao, and Zhigang Suo. Averting cracks caused by insertion reaction in lithium-ion batteries. *J. Mater. Res.*, 25(6):1007–1010, 2010. 40, 41, 42, 105, 107, 112, 141, 157

[73] Rassin Grantab and Vivek B Shenoy. Location- and Orientation-Dependent Progressive Crack Propagation in Cylindrical Graphite Electrode Particles. *J Electrochem Soc*, 158(8):A948, 2011. 40

[74] Rutooj Deshpande, Yang-Tse Cheng, Mark W Verbrugge, and Adam Timmons. Diffusion Induced Stresses and Strain Energy in a Phase-Transforming Spherical Electrode Particle. *J Electrochem Soc*, 158(6):A718, 2011. 41, 125

[75] J Park, W Lu, and A M Sastry. Numerical Simulation of Stress Evolution in Lithium Manganese Dioxide Particles due to Coupled Phase Transition and Intercalation. *J Electrochem Soc*, 158(2):A201–A206, 2011. 41, 125

[76] Robert W. Baluffi, Samuel M Allen, and W. Craig Carter. *Kinetics of Materials*. John Wiley & Sons, Inc., 2005. 48, 210

[77] F Yang. Interaction between diffusion and chemical stresses. *Materials Science and Engineering A*, 409:153–159, 2005. 49, 211

[78] Yu Lin, Yuan Yang, Hongwei Ma, Yi Cui, and Wendy L Mao. Compressional Behavior of Bulk and Nanorod $LiMn_2O_4$ under Nonhydrostatic Stress. *J. Phys. Chem. C*, 115(20):9844–9849, May 2011. 49, 56, 109, 123, 133

[79] Meng Qu, William H Woodford, John M. Maloney, W. Craig Carter, Yet-Ming Chiang, and Krystyn J. Van Vliet. Nanomechanical Quantification of Elastic, Plastic, and Fracture Properties of $LiCoO_2$. *Advanced Energy Materials*, 2(8):940–944, August 2012. 49, 86, 111, 131, 139, 159

[80] T Maxisch and G Ceder. Elastic properties of olivine Li_XFePO_4 from first principles. *Physical Review B*, 73:174112, 2006. 49

[81] M M Thackeray, PJ Johnson, LA de Picciotto, PG Bruce, and J B Goodenough. Electrochemical Extraction of Lithium From $LiMn_2O_4$. *Materials Research Bulletin*, 19(2):179–187, 1984. 49, 56, 133

[82] K Mizushima, P C Jones, P J Wiseman, and J B Goodenough. Li_XCoO_2 ($0 \leq X \leq 1$): A New Cathode Material for Batteries of High Energy Density. *Materials Research Bulletin*, 15:783–789, 1980. 49

[83] AK Padhi, KS Nanjundaswamy, and J B Goodenough. Phospho-olivines as positive-electrode materials for rechargeable lithium batteries. *J Electrochem Soc*, 144(4):1188–1194, 1997. 49

[84] Indrajeet V Thorat, Tapesh Joshi, Karim Zaghib, John N Harb, and Dean R Wheeler. Understanding Rate-Limiting Mechanisms in $LiFePO_4$ Cathodes for Li-Ion Batteries. *J Electrochem Soc*, 158(11):A1185, 2011. 49, 59

[85] M Farkhondeh and C Delacourt. Mathematical Modeling of Commercial $LiFePO_4$ Electrodes Based on Variable Solid-State Diffusivity. *J Electrochem Soc*, 159(2):A177, 2012. 49, 59

[86] S P Timoshenko and J N Goodier. *Theory of Elasticity*. McGraw-Hill, 1970. 50, 84, 129

[87] Brian Lawn. *Fracture of Brittle Solids*. Cambridge University Press, 1993. 50, 83, 91, 125

[88] C Mattheck, D Munz, and H Stamm. Stress Intensity Factor For Semi-Elliptical Surface Cracks Loaded By Stress Gradients. *Engineering Fracture Mechanics*, 18(3):633–641, 1983. 52, 53, 130, 203

[89] H J Petroski and J D Achenbach. Computation of the weight function from a stress intensity factor. *Engineering Fracture Mechanics*, 10:257–266, 1978. 53, 204

[90] John C Newman and I S Raju. An Empirical Stress-Intensity Factor Equation For The Surface Crack. *Engineering Fracture Mechanics*, 15(1-2):185–192, 1981. 53, 204

[91] J. Barker, K West, Y Saidi, R. Pynenburg, B Zachau-Christiansen, and R. Koksbang. Kinetics and thermodynamics of the lithium insertion reaction in spinel phase $Li_XMn_2O_4$. *Journal of Power Sources*, 54:475–478, 1995. 56, 60, 133

[92] M Doyle, John C Newman, AS Gozdz, CN Schmutz, and JM Tarascon. Comparison of modeling predictions with experimental data from plastic lithium ion cells. *J Electrochem Soc*, 143(6):1890–1903, 1996. 12, 18, 58, 59, 131, 132, 213

[93] R L Stewart and R C Bradt. Fracture of single crystal $MgAl_2O_4$. *Journal of Materials Science*, 15:67–72, 1980. 71

[94] M Iwasa and R C Bradt. Fracture Toughness of Single-Crystal Alumina. In W D Kingery, editor, *Structure and Properties of MgO and Al_2O_3 Ceramics*, pages 767–779, 1984. 71

[95] J R Wilson, J S Cronin, S A Barnett, and S J Harris. Measurement of three-dimensional microstructure in a $LiCoO_2$ positive electrode. *Journal of Power Sources*, in press, 2010. 79

[96] Y Shao-Horn, S A Hackney, A J Khaian, K D Kepler, E Skinner, J T Vaughey, and M M Thackeray. Structural fatigue in spinel electrodes in $Li/Li_X[Mn_2]O_4$ cells. *Journal of Power Sources*, 81-82:496–499, 1999. 79, 98

[97] K Dokko, M Nishizawa, S Horikoshi, T Itoh, M Mohamedi, and I Uchida. *In situ* observation of $LiNiO_2$ single-particle fracture during Li-ion extraction and insertion. *Electrochem. Solid-State Lett.*, 3(3):125–127, 2000. 79

[98] Y Ohya, Z E Nakagawa, and K Hamano. Grain-Boundary Microcracking Due to Thermal Expansion Anisotropy in Aluminum Titanate Ceramics. *Journal of the American Ceramic Society*, 70(8):C184–C186, 1987. 80, 82

[99] S W Paulik, M H Zimmerman, K T Faber, and E R Fuller, Jr. Residual stress in ceramics with large thermal expansion anisotropy. *J. Mater. Res.*, 11(11):2795–2803, 1996. 80, 144

[100] D R Clarke. Microfracture In Brittle Solids Resulting From Anisotropic Shape Changes. *Acta Metallurgica*, 28:913–924, 1980. 81, 82, 157

[101] J A Kuszyk and R C Bradt. Influence of Grain Size on Effects of Thermal Expansion Anisotropy in $MgTi_2O_5$. *Journal of the American Ceramic Society*, 56(8):420–423, 1973. 82

[102] A G Evans. Microfracture from Thermal Expansion Anisotropy - I. Single Phase Systems. *Acta Metallurgica*, 26:1845–1853, 1978. 82

[103] E.D. Case, JR Smyth, and O. Hunter. Grain-size dependence of microcrack initiation in brittle materials. *Journal of Materials Science*, 15(1):149–153, 1980. 82

[104] R W Davidge. Cracking at Grain Boundaries in Polycrystalline Brittle Materials. *Acta Metallurgica*, 29:1695–1702, 1981. 82

[105] J T Fredrich and T F Wong. Micromechanics of Thermally Induced Cracking in Three Crustal Rocks. *Journal of Geophysical Research*, 91(B12):12743–12764, 1986. 82

[106] V. Tvergaard and John W Hutchinson. Microcracking in ceramics induced by thermal expansion or elastic anisotropy. *Journal of the American Ceramic Society*, 71(3):157–166, 1988. 82

[107] N Laws and J C Lee. Microcracking in Polycrystalline Ceramics: Elastic Isotropy and Thermal Anisotropy. *J. Mech. Phys. Solids*, 37(5):603–618, 1989. 82

[108] S R Carlson, M Wu, and H F Wang. Micromechanical Modeling of Thermal Cracking in Granite. *Geophysical Monograph*, 56:37–48, 1990. 82

[109] J D Eshelby. The Determination of the Elastic Field of an Ellipsoidal Inclusion, and Related Problems. *Proc R Soc Lon Ser-A*, 241(1226):376–396, 1957. 84

[110] X Wang, I Loa, K Kunc, K Syassen, and M Amboage. Effect of pressure on the structural properties and Raman modes of $LiCoO_2$. *Physical Review B*, 72:224102, 2005. 86, 111

[111] F X Hart and J B Bates. Lattice model calculation of the strain energy density and other properties of crystalline $LiCoO_2$. *Journal of Applied Physics*, 83(12):7560–7566, 1998. 86, 111, 120

[112] C Villevieille, M Boinet, and L Monconduit. Direct evidence of morphological changes in conversion type electrodes in Li-ion battery by acoustic emission. *Electrochemistry Communications*, 12(10):1336–1339, October 2010. 94

[113] K Rhodes, N Dudney, E Lara-Curzio, and C Daniel. Understanding the Degradation of Silicon Electrodes for Lithium-Ion Batteries Using Acoustic Emission. *J Electrochem Soc*, 157(12):A1354–A1360, 2010. 94

[114] K Sawai, K Yoshikawa, H Tomura, and T Ohzuku. Characterization of Materials by Acoustic Emission Histometry for Advanced Lithium Batteries. *Progress in Batteries and Battery Materials*, 17:201–207, 1998. 94

[115] S Didier-Laurent, H Idrissi, and L Roue. *In-situ* study of the cracking of metal hydride electrodes by acoustic emission technique. *Journal of Power Sources*, 179(1):412–416, 2007. 94

[116] W Lai, C K Erdonmez, T F Marinis, C K Bjune, N J Dudney, F Xu, R Wartena, and Yet-Ming Chiang. Ultrahigh-Energy-Density Microbatteries Enabled by New Electrode Architecture and Micropackaging Design. *Advanced Materials*, 22:E1–E6, 2010. 95, 102

[117] J Molenda, A Stoklosa, and T Bak. Modification in the Electronic Structure of Cobalt Bronze Li_XCoO_2 and the Resulting Electrochemical Properties. *Solid State Ionics*, 36:53–58, 1989. 95

[118] A Clemencon, A T Appapillai, S Kumar, and Y Shao-Horn. Atomic force microscopy studies of surface and dimensional changes in Li_XCoO_2 crystals during lithium de-intercalation. *Electrochemica Acta*, 52:4572–4580, 2007. 98

[119] HF Wang, YI Jang, and Yet-Ming Chiang. Origin of cycling stability in monoclinic- and orthorhombic-phase lithium manganese oxide cathodes. *Electrochem. Solid-State Lett.*, 2(10):490–493, 1999. 99

[120] Yet-Ming Chiang, Haifeng Wang, and Young-Il Jang. Electrochemically Induced Cation Disorder and Phase Transformations in Lithium Intercalation Oxides. *Chemistry of Materials*, 13:53–63, 2001. 99

[121] TA Arunkumar and Arumugam Manthiram. Influence of chromium doping on the electrochemical performance of the 5 V spinel cathode $LiMn_{1.5}Ni_{0.5}O_4$. *Electrochimica Acta*, 50(28):5568–5572, 2005. 106

[122] TA Arunkumar and Arumugam Manthiram. Influence of lattice parameter differences on the electrochemical performance of the 5 V spinel $LiMn_{1.5-y}Ni_{0.5-z}M_{y+z}O_4$ (M = Li, Mg, Fe, Co, and Zn). *Electrochem. Solid-State Lett.*, 8(8):A403–A405, 2005. 106, 141

[123] Jun Liu and Arumugam Manthiram. Understanding the Improved Electrochemical Performances of Fe-Substituted 5 V Spinel Cathode $LiMn_{1.5}Ni_{0.5}O_4$. *J. Phys. Chem. C*, 113(33):15073–15079, 2009. 106, 117, 141

[124] S A Langer, W. Craig Carter, and E R Fuller. OOF: Finite Element Analysis of Microstructures, 2009. 108, 148

[125] S Langer, E Fuller, and W. Craig Carter. OOF: An Image-Based Finite-Element Analysis of Material Microstructures. *Comput. Sci. Eng.*, 3(3):15–23, 2001. 108, 148

[126] A C E Reid, S A Langer, R C Lua, V R Coffman, S I Haan, and R E Garcia. Image-based finite element mesh construction for material microstructures. *Computational Materials Science*, 43(4):989–999, 2008. 108, 148

[127] Andrew C. E. Reid, Rhonald C. Lua, R Edwin Garcia, Valerie R. Coffman, and Stephen A. Langer. Modelling Microstructures with OOF2. *Int J Mater Prod Tec*, 35:361–373, 2009. 108, 148

[128] Eunseok Lee and Kristin Persson. Revealing the coupled cation interactions behind the electrochemical profile of $Li_XNi_{0.5}Mn_{1.5}O_4$. *Energy & Environmental Science*, 2012. 108, 118

[129] R Benedek and M M Thackeray. Simulation of the surface structure of lithium manganese oxide spinel. *Physical Review B*, 83(19):195439, May 2011. 23, 109, 111

[130] D Kramer and G Ceder. Tailoring the Morphology of $LiCoO_2$: A First Principles Study. *Chem. Mater.*, 21:3799–3809, 2009. 23, 111, 112, 113

[131] Daniel A Cogswell and Martin Z Bazant. Coherency Strain and the Kinetics of Phase Separation in $LiFePO_4$ Nanoparticles. *ACS Nano*, 6(3):2215–2225, February 2012. 113

[132] Ming Tang, James F Belak, and Milo R Dorr. Anisotropic Phase Boundary Morphology in Nanoscale Olivine Electrode Particles. *J. Phys. Chem. C*, 115(11):4922–4926, March 2011. 113, 127

[133] Dong Wook Shin, Craig A Bridges, Ashfia Huq, M Parans Paranthaman, and Arumugam Manthiram. Role of Cation Ordering and Surface Segregation in High-Voltage Spinel $LiMn_{1.5}Ni_{0.5-x}M_xO_4$ (M = Cr, Fe, and Ga) Cathodes for Lithium-Ion Batteries. *Chem. Mater.*, 24(19):3720–3731, October 2012. 117, 118

[134] M Kunduraci and G G Amatucci. Synthesis and Characterization of Nanostructured 4.7V $Li_XMn_{1.5}Ni_{0.5}O_4$ Spinels for High-Power Lithium-Ion Batteries. *J Electrochem Soc*, 153(7):A1345, 2006. 118

[135] A G Khachaturyan. Some Questions Concerning the Theory of Phase Transformations in Solids. *Sov. Phys. Solid State*, 8:2163–2168, 1967. 120

[136] A G Khachaturyan. *Theory of Structural Transformations in Solids*. Dover, 2008. 120

[137] J Recio, R Franco, A Martín Pendás, M Blanco, L Pueyo, and Ravindra Pandey. Theoretical explanation of the uniform compressibility behavior observed in oxide spinels. *Physical Review B*, 63(18):184101, April 2001. 122

[138] Jolanta Darul, Waldemar Nowicki, and Paweł Piszora. Unusual Compressional Behavior of Lithium–Manganese Oxides: A Case Study of $Li_4Mn_5O_{12}$. *J. Phys. Chem. C*, 116(33):17872–17879, August 2012. 122, 123

[139] Jay D Bass, Donald J Weidner, N Hamaya, M Ozima, and S Akimoto. Elasticity of the olivine and spinel polymorphs of Ni_2SiO_4. *Phys Chem Minerals*, 10(6):261–272, 1984. 122, 123

[140] M F Lewis. Elastic constants of magnesium aluminate spinel. *The Journal of the Acoustical Society of America*, 40:728, 1966. 123

[141] Donald J Weidner and Nozomu Hamaya. Elastic properties of the olivine and spinel polymorphs of Mg_2GeO_4, and evaluation of elastic analogues. *Physics of the earth and planetary interiors*, 33(4):275–283, 1983. 123

[142] R B Von Dreele, A Navrotsky, and A L Bowman. Refinement of the crystal structure of Mg_2GeO_4 spinel. *Acta Crystallographica Section B: Structural Crystallography and Crystal Chemistry*, 33(7):2287–2288, 1977. 123

[143] Z Li and E S Fisher. Single crystal elastic constants of zinc ferrite ($ZnFe_2O_4$). *J Mater Sci Lett*, 9(7):759–760, 1990. 123

[144] D Levy, A Pavese, and M Hanfland. Phase transition of synthetic zinc ferrite spinel ($ZnFe_2O_4$) at high pressure, from synchrotron X-ray powder diffraction. *Phys Chem Minerals*, 27(9):638–644, 2000. 123

[145] Z Li, E S Fisher, J Z Liu, and M V Nevitt. Single-crystal elastic constants of Co-Al and Co-Fe spinels. *Journal of Materials Science*, 26(10):2621–2624, 1991. 123

[146] H Furuhashi, M Inagaki, and S Naka. Determination of cation distribution in spinels by X-ray diffraction method. *Journal of Inorganic and Nuclear Chemistry*, 35(8):3009–3014, 1973. 123

[147] A W England. *Equations of state of oxides and silicates and new data on the elastic properties of spinel, magnetite, and cadmium oxide*. PhD thesis, Massachusetts Institute of Technology, Cambridge, MA, 1970. 123

[148] Donald J Weidner, Hiroshi Sawamoto, Satoshi Sasaki, and Mineo Kumazawa. Singlecrystal elastic properties of the spinel phase of Mg_2SiO_4. *Journal of Geophysical Research: Solid Earth (1978–2012)*, 89(B9):7852–7860, 1984. 123

[149] Y Syono, Y Fukai, and Y Ishikawa. Anomalous Elastic Properties of Fe_2TiO_4. *Journal of the Physical Society of Japan*, 31(2):471–476, 1971. 123

[150] Herbert Wang and Gene Simmons. Elasticity of some mantle crystal structures: 1. Pleonaste and hercynite spinel. *Journal of Geophysical Research: Solid Earth (1978–2012)*, 77(23):4379–4392, 1972. 123

[151] H J Reichmann. Sound velocities and elastic constants of $ZnAl_2O_4$ spinel and implications for spinel-elasticity systematics. *Am Mineral*, 91(7):1049–1054, July 2006. 123

[152] Richard F Cooley and James S Reed. Equilibrium cation distribution in $NiAl_2O_4$, $CuAl_2O_4$, and $ZnAl_2O_4$ spinels. *Journal of the American Ceramic Society*, 55(8):395–398, 1972. 123

[153] Jordi Cabana, Montserrat Casas-Cabanas, Fredrick O Omenya, Natasha A Chernova, Dongli Zeng, M S Whittingham, and Clare P Grey. Composition-Structure Relationships in the Li-ion Battery Electrode Material $LiNi_{0.5}Mn_{1.5}O_4$. *Chem. Mater.*, 24(15):2952–2964, August 2012. 123

[154] Nonglak Meethong, Yu-Hua Kao, Ming Tang, Hsiao-Ying Huang, W. Craig Carter, and Yet-Ming Chiang. Electrochemically Induced Phase Transformation in Nanoscale Olivines $Li_{1-x}MPO_4$ (M = Fe, Mn). *Chem. Mater.*, 20(19):6189–6198, October 2008. 124

[155] M Tang, H Y Huang, N Meethong, Y H Kao, W. Craig Carter, and Yet-Ming Chiang. Model for the Particle Size, Overpotential, and Strain Dependence of Phase Transition Pathways in Storage Electrodes: Application to Nanoscale Olivines. *Chem. Mater.*, 21(8):1557–1571, April 2009. 124

[156] Y H Kao, M Tang, N Meethong, J Bai, W. Craig Carter, and Yet-Ming Chiang. Overpotential-Dependent Phase Transformation Pathways in Lithium Iron Phosphate Battery Electrodes. *Chemistry of Materials*, 2010. 124

[157] Rahul Malik, F Zhou, and G Ceder. Kinetics of non-equilibrium lithium incorporation in $LiFePO_4$. *Nature Materials*, 2011. 124

[158] D A Porter and K E Easterling. *Phase transformations in metals and alloys.* 1992. 129

[159] Y Zhou and T H North. Kinetic modelling of diffusion-controlled, two-phase moving interface problems. *Modelling Simul. Mater. Sci. Eng.*, 1:505, 1993. 129, 203

[160] Youngjoon Shin and Arumugam Manthiram. Influence of the Lattice Parameter Difference between the Two Cubic Phases Formed in the 4 V Region on the Capacity Fading of Spinel Manganese Oxides. *Chem. Mater.*, 15(15):2954–2961, July 2003. 141

[161] S J Harris, E K Rahani, and V B Shenoy. Direct *In Situ* Observation and Numerical Simulations of Non-Shrinking-Core Behavior in an MCMB Graphite Composite Electrode. *J Electrochem Soc*, 159(9):A1501–A1507, January 2012. 141

[162] M Ortiz and S Suresh. Statistical Properties of Residual-Stresses and Intergranular Fracture in Ceramic Materials. *J Appl Mech-T Asme*, 60(1):77–84, 1993. 144

[163] W.S. Kreher. Modeling of random microstructural stresses and grain boundary damage in polycrystals. *Computational Materials Science*, 7(1-2):147–153, 1996. 144

[164] Venkata R. Vedula, S. Jill Glass, David M. Saylor, Gregory S Rohrer, W. Craig Carter, Stephen A. Langer, and Edwin R Fuller Jr. Residual-Stress Predictions in Polycrystalline Alumina. *J. Am. Ceram. Soc.*, 84(12):2947–2954, 2001. 144

[165] SB Biner. A Fem Analysis of Crack-Growth in Microcracking Brittle Solids. *Engineering Fracture Mechanics*, 51(4):555–573, 1995. 144

[166] R Edwin Garcia and Yet-Ming Chiang. Spatially resolved modeling of microstructurally complex battery architectures. *J Electrochem Soc*, 154(9):A856–A864, 2007. 144

[167] S Galal Yousef, J Rödel, E R Fuller, A Zimmermann, and B S El-Dasher. Microcrack Evolution in Alumina Ceramics: Experiment and Simulation. *Journal of the American Ceramic Society*, 88(10):2809–2816, October 2005. 144

[168] A Zimmermann, W. Craig Carter, and ER Fuller. Damage evolution during microcracking of brittle solids. *Acta Materialia*, 49(1):127–137, 2001. 144

[169] MH Zimmerman, DM Baskin, KT Faber, ER Fuller, AJ Allen, and DT Keane. Fracture of a textured anisotropic ceramic. *Acta Materialia*, 49(16):3231–3242, 2001. 144

[170] V Cannillo and W. Craig Carter. Computation and Simulation of Reliability Parameters and their Variations in Heterogeneous Materials. *Acta Materialia*, pages 3593–3605, 2000. 144

[171] Valeria Cannillo and W. Craig Carter. A stochastic model of damage accumulation in complex microstructures. *Journal of Materials Science*, 40:3993–4004, 2005. 144

[172] SB Batdorf and JG Crose. Statistical-Theory for Fracture of Brittle Structures Subjected to Nonuniform Polyaxial Stresses. *J Appl Mech-T Asme*, 41(2):459–464, 1974. 144

[173] P Kittl and G Diaz. Weibull's Fracture Statistics, or Probabilistic Strength of Materials: State of the Art. *Res Mechanica*, 24:99–207, 1988. 144

[174] R Danzer, T Lube, P Supancic, and R Damani. Fracture of Ceramics. *Adv. Eng. Mater.*, 10(4):275–298, April 2008. 144

[175] J D Poloniecki and T R Wilshaw. Determination of Surface Crack Size Densities in Glass. *Nature*, 229(8):226–227, 1971. 149

[176] A De S Jayatilaka and K Trustrum. Statistical approach to brittle fracture. *Journal of Materials Science*, 12:1426–1430, 1977. 151

[177] D G Rickerby. Theoretical Aspects of the Statistical Variation of Strength. *Journal of Materials Science*, 15(10):2466–2470, 1980. 151

[178] B Bergman. Estimation of Weibull Parameters Using a Weight Function. *J Mater Sci Lett*, 5(6):611–614, 1986. 154

[179] K Zhao, M Pharr, J J Vlassak, and Z Suo. Fracture of electrodes in lithium-ion batteries caused by fast charging. *Journal of Applied Physics*, 108:073517, 2010. 157

[180] Young-Il Jang, Bernd J Neudecker, and Nancy J Dudney. Lithium Diffusion in Li_XCoO_2 ($0.45 \leq X \leq 0.7$) Intercalation Cathodes. *Electrochemical and Solid-State Letters*, 4(6):A74–A77, 2001. 22, 214, 215

[181] Deepak K Karthikeyan, Godfrey Sikha, and Ralph E White. Thermodynamic model development for lithium intercalation electrodes. *Journal of Power Sources*, 185(2):1398–1407, December 2008. 22, 214, 215

Appendices

Appendix A

Methods

A.1 Experimental Methods

A.1.1 Materials

$LiCoO_2$ powder was sourced from AGC Seimi Chemical Co. Ltd. (Kanagawa, Japan). $LiMn_{1.5}Ni_{0.5}O_4$ powder was sourced from NEI Corporation (Somerset, NJ). $LiFe_{0.08}Mn_{1.5}Ni_{0.42}O_4$ was synthesized by solid state reaction from stoichiometric amounts of Li_2CO_3, Fe_3O_4, Mn_2O_3, and NiO sourced from Sigma-Aldrich. The precursors were ball-milled in acetone for 24h and then calcined in air at 900°C for 24h with heating and cooling rates of 5°C min^{-1}.

Sintered electrodes were prepared by uniaxial pressing at 140 MPa in either 1/2 or 5/8 inches die and held for 2 minutes. Green body electrodes were then sintered at 950°C for 1.5h (for $LiCoO_2$) and 12h (for $LiMn_2O_4$ and $LiMn_{1.5}Ni_{0.5}O_4$) with a heating rate of 9°C min^{-1} and a furnace cool. Coarsened powders of $LiMn_2O_4$, $LiMn_{1.5}Ni_{0.5}O_4$, and $LiFe_{0.08}Mn_{1.5}Ni_{0.42}O_4$ are prepared by grinding sintered electrodes by hand in an agate mortar and pestle until a free-flowing powder is obtained.

A.1.2 Electrochemical Measurements

The composite electrodes used for acoustic emission measurements are formulated with 90/5/5 (wt. %) of active / Super P / Kynar 2101 binder and the composite was prepared by mixing in 1-methyl-2-pyrrolidinone (NMP), drying on a hot plate overnight, then grinding by hand in an agate mortar and pestle. The resulting composite powder was then uniaxially pressed into pellets at 140 MPa in a 1/2 inch die and held for 1 minute to obtain 0.5 mm thick electrodes. All electrodes (sintered and composite) were held in place on the positive coin cell can with a conductive binder that is a mixture of PVDF, Ketjen black ECP and vapor grown carbon fiber (VGCF) in NMP. This binder was cured overnight at 120°C in a vacuum oven before transferring the electrodes to the glovebox.

The composite electrodes used for composition-dependent lattice parameter measurements are prepared in an identical manner, but with a formulation of 80/10/10 (wt. %) of active / Super P / Kynar 2101 binder. Sintered and composite electrodes were prepared were mounted in 2016 coin cells (MTI Corporation, Richmond, CA).

For $LiCoO_2$ and $LiMn_2O_4$, the electrolyte was a blend of alkyl carbonates with 1.2 M $LiPF_6$ salt; a 1:1 mixture of ethylene carbonate and diethyl carbonate with 1 M $LiPF_6$ was used for $LiMn_{1.5}Ni_{0.5}O_4$ and $LiFe_{0.08}Mn_{1.5}Ni_{0.42}O_4$. All cells used 2 pieces of Tonen E20MMS separator and a Li metal (Alfa Aesar) negative electrode. Electrodes were cycled on a MACCOR 4000 tester at constant current to a materials-specific cutoff voltage.

A.1.3 Acoustic Emission

Acoustic emission measurements are collected with a Physical Acoustics Corp μDISP instrument controlled by AEWin software on a laptop PC. A micro-30 sensor was attached to the positive electrode side of coin cell, using vacuum grease as a couplant and held in place with rubber bands. Between the sensor and controller, a 2/4/6 voltage pre-amplifier was set to

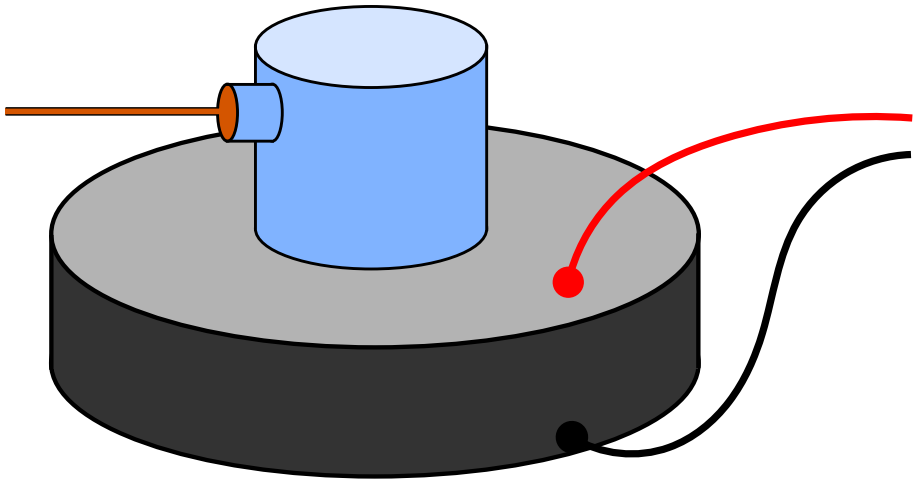

Figure A-1: Schematic experimental set-up for acoustic emission measurements.

40 dB gain; no software gain was used. The raw data are collected with an analog frequency filter with a bandpass of 100 kHz to 2 MHz and analog to digital conversion is done at 1 MHz. The event threshold was set at 24 dB with a front-end filter that excludes events that register less than 3 counts; these test parameters were chosen to give minimal background, as measured on an identically prepared cell that is not electrochemically cycled.

A.1.4 Scanning Electron Microscopy

Scanning electron microscopy is performed using a JEOL 5910 instrument. Typical accelerating voltages and working distances are 15 kV and 10-15 mm, respectively. Unless otherwise indicated, the micrographs are secondary electron images.

A.1.5 X-Ray Diffraction

X-Ray diffraction measurements are taken on a PANalytical X'Pert Pro instrument using copper K_α tube-source radiation. Measurements are collected with the high-speed optics in a Bragg-Brentano $\theta - 2\theta$ geometry. Powder samples are mounted in 16 mm diameter wells centered on the open Eulerian cradle. Fixed $\frac{1}{2}^\circ$ slits are used for both the incident and

diffracted beams. A 10 mm width limiting mask, 1° anti-scatter slit and 0.02 radian Soller slits are also used for all measurements.

Lattice parameters are determined from the measured patterns by profile fitting. Peaks are fit with asymmetric shape and width. Lattice parameters are refined by first refining without sample displacement and then turning it on in the refinement. Fe-containing samples most reliabily refined by starting from a reference pattern for $LiMn_{1.5}Fe_{0.5}O_4$.

A.2 Finite Element Strain-Energy-Release Rate Calculations

The strain-energy-release rates computed from two-dimensional finite element calculations. Build an initial mesh which includes the crack of desired length, and then use the tools in OOF2to refine it. Refinement driven by automated set of Python scripts. Figure A-2a shows an example initial mesh overlaid on the two-phase slab-like particle with a crack with fractional length $\frac{a}{L} = 0.3$ and Figure A-2b shows the refined mesh. Figure A-3 shows the refined mesh near the crack tip, where the smallest elements have a size of $\simeq 5 \times 10^{-3}$ of the crack length An analogous method was used to refine meshes for strain-energy-release rate estimates for four-grain ensemble of Chapter 3.

A.3 Numerical Methods for Single Particle Model

The thermodynamic solution cases in Chapter 2 with Nernstian open-circuit voltage profiles are solved numerically by the method of lines with spatial discretization using centered finite differences, using 400 spatial grid points. Time integration is performed using MATLAB's *ode15s* solver. The "$Li_XMn_2O_4$-like" case is solved with the built-in *pdepe* solver in MATLAB®. The spherical particle is discretized into 1,000 spatial points and time stepping

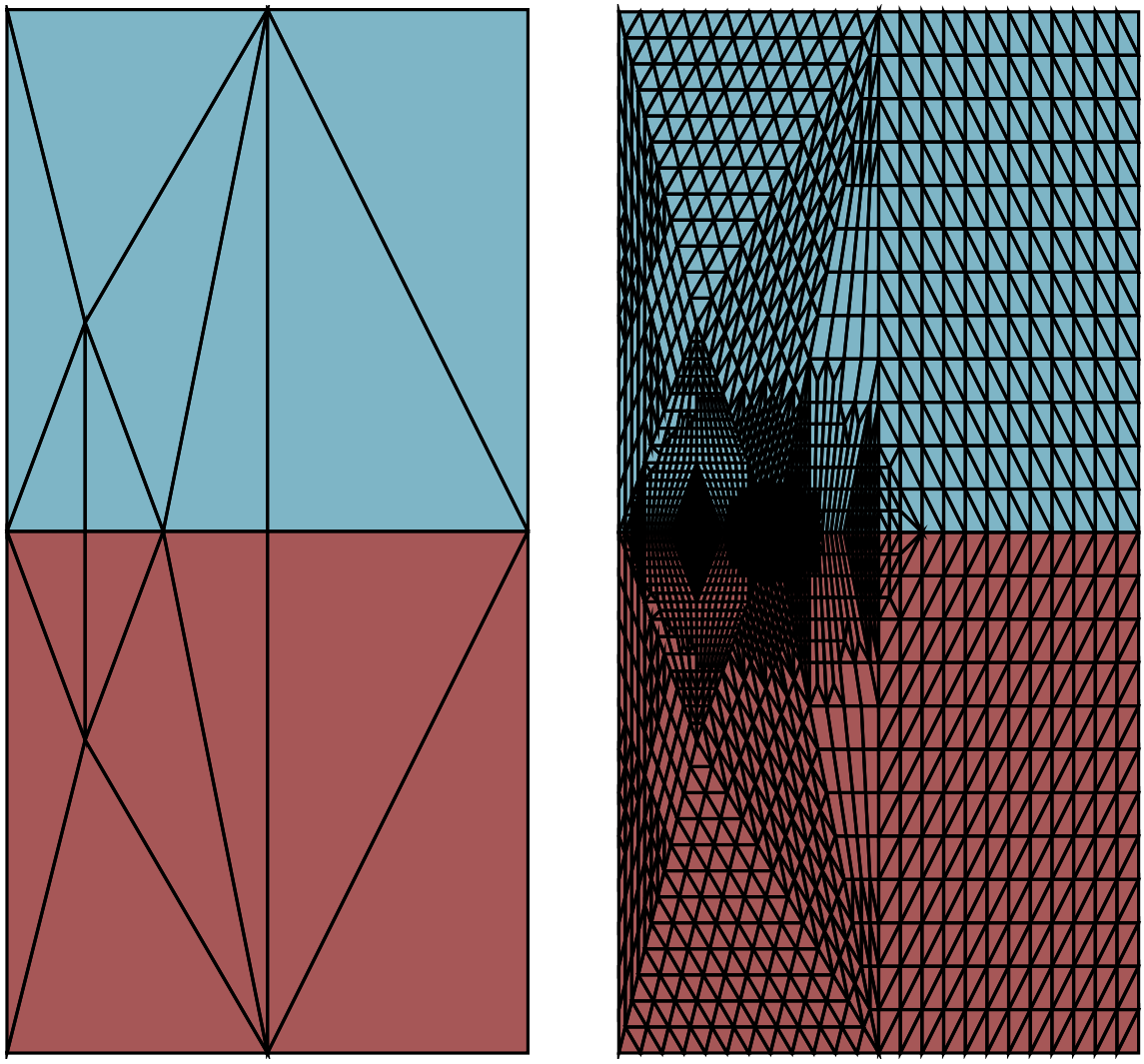

(a) Starting mesh built by hand in Mathematica.

(b) Final mesh used for computation, after refinement steps in OOF2.

Figure A-2: Finite element meshes used for strain-energy-release rate estimates in OOF2. Example shown has $\frac{a}{L} = 0.3$.

is handled by the *ode15s* adaptive integrator.

A.4 Moving Boundary (Stefan) Problem

The moving boundary problem of Chapter 5 is solved numerically by the method of lines with spatial discretization using centered finite differences. In the single phase regions, time

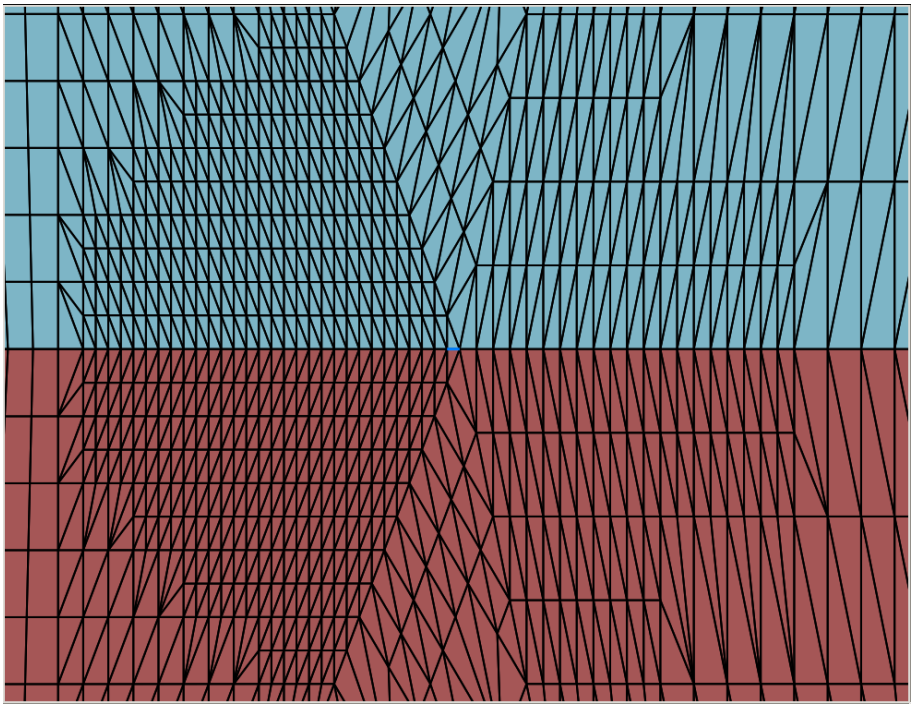

Figure A-3: Zoomed in view of the crack tip area of the refined mesh used to compute the strain-energy-release rate. Example shown has $\frac{a}{L} = 0.3$. The highlighted segment adjacent to the crack tip has a length which is $\simeq 5 \times 10^{-3}$ of the crack length.

integration is performed using MATLAB's *ode15s* solver. In the two-phase regions, we solve using explicit finite differences (Forward Euler). We have performed numerical calculations for dimensionless currents $0.01 \leq \hat{I} \leq 1$. We use 300 spatial grid points and a fixed time step in the two-phase region of $\Delta\hat{t} = 2.8 \times 10^{-8}$ for calculations with dimensionless currents $0.05 \leq \hat{I} \leq 1$ and 150 spatial grid points and a fixed-time step in the two-phase region of $\Delta\hat{t} = 1.3 \times 10^{-6}$ for $\hat{I} = 0.01$. The interface is tracked between grid points by assuming that the concentration profile on each side of the interface is described by a quadratic polynomial, a strategy introduced by Zhou and North [159].

A.5 Method of Weight Functions

The method of weight functions uses an integral transform to calculate stress intensity factors under arbitrary loads. First, this method requires a reference case where the crack geometry, stress profile, and corresponding stress intensity factor are all known. Then, the the method of weight functions can be applied to calculate the stress intensity factor for arbitrary loading of the same crack geometry. The non-uniform diffusion-induced stress profiles due to galvanostatic cycling beg for the method of weight functions, but a satisfactory reference load for the crack geometry shown in Figure 2-1 does not exist, so we use the approximate geometry shown in Figure 2-2. This type of geometric approximations typically affects the numerical value of the calculated stress intensity factor by less than one order of magnitude, usually on the order of $\sqrt{\pi}$.

We apply the method of weight functions to calculate the stress intensity factor, following the approach of Mattheck, *et al.* [88]. The desired stress intensity factor is calculated from the reference case as

$$K_{\mathrm{I}} = \frac{E'}{K_{ref}} \int_0^a \sigma_\theta(x) \frac{\partial u_r(x,a)}{\partial a} \mathrm{d}x \tag{A.1}$$

where for plane strain, $E' = E/(1-\nu^2)$ and for plane stress $E' = E$. The weight function

$m(x,a)$ has been defined in terms of the displacement field near the crack tip

$$m(x,a) = \frac{\partial u_r(x,a)}{\partial a} \tag{A.2}$$

The displacement field, $u_r(x,a)$ is calculated from the reference stress intensity factor by the method of Petroski and Achenbach [89]

$$u_r(x,a) = \frac{\sigma_0}{E'\sqrt{2}}\left[4F\left(\frac{a}{l}\right)\sqrt{a}\sqrt{a-x} + G\left(\frac{a}{l}\right)\frac{(a-x)^{3/2}}{\sqrt{a}}\right] \tag{A.3}$$

where the function F is defined by the relationship

$$K_{ref} = \sigma_0\sqrt{\pi a}F\left(\frac{a}{l}\right) \tag{A.4}$$

and the function G is determined from self-consistency of the method

$$G\left(\frac{a}{l}\right) = \left[S_1(a) - 4F\left(\frac{a}{l}\right)\sqrt{a}S_2(a)\right]\frac{\sqrt{a}}{S_3(a)} \tag{A.5}$$

$$S_1(a) = \pi\sqrt{2}\sigma_0\int_0^a\left[F\left(\frac{a}{l}\right)\right]^2 a\mathrm{d}a \tag{A.6}$$

$$S_2 = \frac{2}{3}\sigma_0 a^{3/2} \tag{A.7}$$

$$S_3 = \frac{2}{5}\sigma_0 a^{5/2} \tag{A.8}$$

σ_0 is a characteristic load of the reference case, which we have taken as uniform tensile stress. Newman and Raju [90] give analytical expressions for the stress intensity factor of the semi-elliptical surface cracked plate under pure tension and bending loads as polynomial functions

$$K = \sigma\sqrt{\pi\frac{a}{Q}}F\left(\frac{a}{l},\frac{a}{w},\frac{w}{b},\phi\right) \tag{A.9}$$

where Q is the elliptic integral

$$\sqrt{Q} = \int_0^{\pi/2}\left[1-\left(1-\frac{a^2}{w^2}\right)\sin^2\phi\right]^{1/2}\mathrm{d}\phi \tag{A.10}$$

which for $a/w \leq 1$ is approximated by the polynomial expression

$$Q = 1.464 \left(\frac{a}{w}\right)^{1.65} \tag{A.11}$$

For uniform tension, which was used as the reference case for the present study,

$$F = \left[M_1 + M_2 \left(\frac{a}{l}\right)^2 + M_3 \left(\frac{a}{l}\right)^4\right] f_\phi g f_w \tag{A.12}$$

$$M_1 = 1.13 - 0.09 \left(\frac{a}{w}\right) \tag{A.13}$$

$$M_2 = -0.54 + \frac{0.89}{0.2 + (a/w)} \tag{A.14}$$

$$M_3 = 0.5 - \frac{1.0}{0.65 + (a/w)} + 14 \left(1.0 - \frac{a}{w}\right)^{24} \tag{A.15}$$

$$f_\phi = \left[\left(\frac{a}{w}\right)^2 \cos^2 \phi + \sin^2 \phi\right]^{1/4} \tag{A.16}$$

$$g = 1 + \left[0.1 + 0.35 \left(\frac{a}{l}\right)^2\right] (1 - \sin \phi)^2 \tag{A.17}$$

$$f_w = \sqrt{\sec \left(\frac{\pi w}{2b} \sqrt{\frac{a}{l}}\right)} \tag{A.18}$$

Under the conditions $w = a$, $b = \pi r_{\max}$, $l = r_{\max}$ this reduces to

$$f_w = \sqrt{\sec \left(\frac{1}{2} \left(\frac{a}{r_{\max}}\right)^{3/2}\right)} \tag{A.19}$$

and is approximated by

$$f_w = 1 + \frac{1}{16} \left(\frac{a}{r_{\max}}\right)^3 + \frac{7}{1536} \left(\frac{a}{r_{\max}}\right)^6 \tag{A.20}$$

THIS PAGE INTENTIONALLY LEFT BLANK

Appendix B

Derivations

B.1 Derivation of Compositional Stress Distributions

Following Timoshenko and Goodier.

In spherically symmetric system, mechanical equilibrium equation reduces to

$$\frac{\partial \sigma_r}{\partial r} + \frac{2}{r}(\sigma_r - \sigma_\theta) = 0 \tag{B.1}$$

The relevant stress-strain relations are

$$\epsilon_r - \Omega c_{\max} X = \frac{1}{E}(\sigma_r - 2\nu\sigma_\theta) \tag{B.2}$$

$$\epsilon_\theta - \Omega c_{\max} X = \frac{1}{E}\left(\sigma_\theta - \nu\left[\sigma_r + \sigma_\theta\right]\right) \tag{B.3}$$

The strain-displacement equations are

$$\epsilon_r = \frac{\partial u}{\partial r} \qquad\qquad \epsilon_\theta = \frac{u}{r} \tag{B.4}$$

Solving the strain equations for the stresses gives

$$\sigma_r = \frac{E}{(1+\nu)(1-2\nu)}\left[(1-\nu)\epsilon_r + 2\nu\epsilon_\theta - (1+\nu)\Omega c_{\max} X\right] \tag{B.5}$$

$$\sigma_\theta = \frac{E}{(1+\nu)(1-2\nu)}\left[\epsilon_\theta + \nu\epsilon_r - (1+\nu)\Omega c_{\max} X\right] \tag{B.6}$$

Substiting these into the equilibrium equation, and then substitution for the strains in terms of the displacement—and assuming the partial molar volume is independent of composition—gives the second order ordindary differential equation for the displacement field

$$\frac{\partial^2 u}{\partial r^2} + \frac{2}{r}\frac{\partial u}{\partial r} - \frac{2u}{r^2} = \frac{1+\nu}{1-\nu}\Omega c_{\max}\frac{dX}{dr} \tag{B.7}$$

The solution of this is

$$u = \frac{1+\nu}{1-\nu}\frac{\Omega c_{\max}}{3}\frac{1}{r^2}\int_a^r X r^2 dr + C_1 r + \frac{C_2}{r^2} \tag{B.8}$$

In terms of this general solution, the stresses are

$$\sigma_r = -\frac{2\Omega c_{\max} E}{3(1-\nu)}\frac{1}{r^3}\int_a^r X r^2 dr + \frac{EC_1}{1-2\nu} - \frac{2EC_2}{1+\nu}\frac{1}{r^3} \tag{B.9}$$

$$\sigma_\theta = \frac{\Omega c_{\max} E}{3(1-\nu)}\frac{1}{r^3}\int_a^r X r^2 dr + \frac{EC_1}{1-2\nu} - \frac{EC_2}{1+\nu}\frac{1}{r^3} - \frac{\Omega c_{\max} X}{3(1-\nu)} \tag{B.10}$$

Now enforce boundary conditions to find C_1 and C_2. For a solid sphere, take $a = 0$ and require that $u(r = 0) = 0$. This requires that $C_2 = 0$. For a traction-free surface, require that $\sigma_r(r = r_{\max}) = 0$. Doing so, we find

$$\frac{EC_1}{1-2\nu} = \frac{2\Omega c_{\max} E}{3(1-\nu)}\frac{1}{r_{\max}^3}\int_0^{r_{\max}} X r^2 dr \tag{B.11}$$

Substituting all of this,

$$\sigma_r = -\frac{2\Omega c_{\max} E}{3(1-\nu)}\left[\frac{1}{r_{\max}^3}\int_0^{r_{\max}} Xr^2dr - \frac{1}{r^3}\int_0^r Xr^2dr\right] \tag{B.12}$$

$$\sigma_\theta = \frac{\Omega c_{\max} E}{3(1-\nu)}\left[\frac{2}{r_{\max}^3}\int_0^{r_{\max}} Xr^2dr + \frac{1}{r^3}\int_0^r Xr^2dr - X\right] \tag{B.13}$$

The average composition inside a sphere of radius r is defined as

$$X_{av}(r) = \frac{4\pi\int_0^r Xr^2dr}{{}^4\!/_3\pi r^3} \tag{B.14}$$

$$= \frac{3}{r^3}\int_0^r Xr^2dr$$

Substituting this gives the desired expressions as given in Section 2.2.2.

$$\sigma_r(r,t) = \frac{2\Omega E c_{\max}}{9(1-\nu)}\left[X_{av}(r_{\max},t) - X_{av}(r,t)\right] \tag{B.15}$$

$$\sigma_\theta(r,t) = \frac{\Omega E c_{\max}}{9(1-\nu)}\left[2X_{av}(r_{\max},t) + X_{av}(r,t) - 3X(r,t)\right] \tag{B.16}$$

These expression are equivalent to those for thermal stresses under the substitutions

$$\alpha \to \frac{\Omega c_{\max}}{3} \qquad\qquad T \to X \tag{B.17}$$

Where α is the linear coefficient of thermal expansion and T is temperature.

B.2 Detailed Derivation of Composition-Dependent Diffusivity for Non-Ideal, Elastically Coupled Intercalation Solutions

Electrochemical cycling of the particle is modeled by the diffusion equation

$$\frac{\partial X}{\partial t} = -\nabla \cdot \mathbf{J} \tag{B.18}$$

where X is composition which is scaled to take values $0 \leq X \leq 1$, and the flux $\mathbf{J}$ is given by the generalized flux equation

$$\mathbf{J} = -MX\nabla\Phi \tag{B.19}$$

where M is a mobility and the flux is proportional to the gradient of the diffusion potential Φ, which incorporates both chemical and mechanical driving forces for diffusion [76] For a vacancy-mediated diffusion mechanism, the mobility M is proportional to the vacancy fraction

$$M = M_0 (1 - X) \tag{B.20}$$

Here, M_0 is a characteristic mobility, which we assume is constant The diffusion potential is for a non-ideal, elastically coupled solution is

$$\Phi = \mu^0 + RT \ln \left(\gamma \, \frac{X}{1 - X} \right) - \Omega\sigma_h \tag{B.21}$$

In addition to the composition, X, the diffusion potential Φ contains μ^0, a reference chemical potential; γ, an activity coefficient describing the thermodynamic non-ideality of the concentrated solution; Ω, the partial molar volume of the diffusing species; and σ_h, the local hydrostatic stress. The gradient of the diffusion potential may be expressed as

$$\begin{aligned} \nabla\Phi &= RT\nabla \left(\ln\gamma + \ln X - \ln(1 - X) \right) - \Omega\nabla\sigma_h \\ &= RT \left(\frac{\partial \ln\gamma}{\partial X}\nabla X + \frac{1}{X}\nabla X + \frac{1}{1 - X}\nabla X \right) - \Omega\nabla\sigma_h \\ &= RT \left(\frac{\partial \ln\gamma}{\partial X} + \frac{1}{X} + \frac{1}{1 - X} \right) \nabla X - \Omega\nabla\sigma_h \end{aligned} \tag{B.22}$$

Substituting this yields

$$\mathbf{J} = -M_0 RT\,(1-X)\,X\left[\left(\frac{\partial \ln \gamma}{\partial X} + \frac{1}{X} + \frac{1}{1-X}\right)\nabla X - \frac{\Omega}{RT}\nabla \sigma_h\right] \tag{B.23}$$

For a spherical particle with traction-free boundaries, the term proportional to the gradient in hydrostatic stress can be recast as a term proportional to the composition gradient [77, 58]. The hydrostatic stress $\sigma_h(r,t)$ is given as

$$\begin{aligned}\sigma_h(r,t) &= \frac{1}{3}\left(\sigma_r(r,t) + 2\sigma_\theta(r,t)\right) \\ &= \frac{2\Omega E c_{\max}}{9(1-\nu)}\left[X_{av}(r_{\max},t) - X(r,t)\right]\end{aligned} \tag{B.24}$$

The gradient of the hydrostatic stress is

$$\begin{aligned}\nabla\sigma_h &= \nabla\left(\frac{2\Omega E c_{\max}}{9(1-\nu)}\left[X_{av}(r_{\max},t) - X(r,t)\right]\right) \\ &= \frac{2\Omega E c_{\max}}{9(1-\nu)}\nabla\left[X_{av}(r_{\max},t) - X(r,t)\right] \\ &= \frac{-2\Omega E c_{\max}}{9(1-\nu)}\nabla X(r,t)\end{aligned} \tag{B.25}$$

Substitution of this into Equation B.28 allows the hydrostatic-stress-gradient term in the flux equation to be expressed in terms of a composition gradient and leads to the identification of the dimensionless chemomechanical coupling parameter $\hat{\theta}$.

$$\nabla\sigma_h = -\hat{\theta}\nabla X \tag{B.26}$$

Where the dimensionless chemomechanical coupling parameter $\hat{\theta}$ is defined as

$$\hat{\theta} = \frac{2\Omega^2 E c_{\max}}{9RT(1-\nu)} \tag{B.27}$$

and c_{max} is the maximum concentration (units of mol/m^3), E is the Young's modulus, and ν is Poisson's ratio. Table 2.1 lists values of the chemomechanical coupling parameter $\hat{\theta}$ for the common cathode materials $\mathrm{Li}_X\mathrm{Mn}_2\mathrm{O}_4$, $\mathrm{Li}_X\mathrm{CoO}_2$, and $\mathrm{Li}_X\mathrm{FePO}_4$. It is important to note that $\hat{\theta}$ is strictly greater than zero for any stable material. While the partial molar volume,

Ω, may be positive or negative, $\hat{\theta}$ depends on Ω^2 which is always positive. As the Poisson's ratio must take values $-1 \leq \nu \leq 1/2$, the quantity $(1-\nu)$ is always positive; the remaining quantities comprising $\hat{\theta}$ are all strictly positive.

Note that this substitution is only possible for a traction-free spherical particle. For a constrained spherical particle, the stress-gradient depends on the local composition gradient and additional non-local terms.

With this substitution, the flux equation is now specified uniquely in terms of local composition gradients, as

$$\mathbf{J} = -M_0 RT\,(1-X)\,X\left[\frac{\partial \ln\gamma}{\partial X} + \frac{1}{X} + \frac{1}{1-X} + \hat{\theta}\right]\nabla X \tag{B.28}$$

Now, the Einstein relation, $D_0 = M_0 RT$ may be applied to formulate the flux equation in terms of a characteristic diffusivity D_0.

$$\mathbf{J} = -D_0\,(1-X)\,X\left[\frac{\partial \ln\gamma}{\partial X} + \frac{1}{X} + \frac{1}{1-X} + \hat{\theta}\right]\nabla X \tag{B.29}$$

The non-ideal solution behavior of the intercalation compound is captured in the $\frac{\partial \ln\gamma}{\partial X}$ term in Equation B.28.

For intercalation materials this thermodynamic non-ideality may be directly determined from the half-cell open circuit voltage. The open circuit voltage of a half-cell, $V(X)$, is related to the chemical potential of the intercalated ion A^{z+} in the host material μ_A by the Nernst Equation:

$$\begin{aligned} V(X) &= -\left(\frac{\mu_A - \mu_A^0}{z\mathcal{F}}\right) \\ &= -\frac{RT}{z\mathcal{F}}\ln\left(\gamma\,\frac{X}{1-X}\right) \end{aligned} \tag{B.30}$$

where μ_A^0 is the chemical potential of elemental A (the reference state), and $\mathcal{F}$ is Faraday's constant and z is the formal charge of ionic A. Manipulation of this relationship yields an expression for the non-ideal solution term

$$\frac{\partial \ln\gamma}{\partial X} = -\frac{z\mathcal{F}}{RT}\,\frac{\partial V(X)}{\partial X} - \frac{1}{X} - \frac{1}{1-X} \tag{B.31}$$

Finally, substitution of Equation B.31 into Equation B.28 gives the desired flux expression

$$\begin{aligned}\mathbf{J} &= -D_0 X\,(1-X)\left(-\frac{z\mathcal{F}}{RT}\frac{\partial V(X)}{\partial X}+\hat{\theta}\right)\nabla X \\ &= -\tilde{D}(X)\nabla X\end{aligned} \tag{B.32}$$

where the second equality defines the chemical diffusivity $\tilde{D}(X)$ by grouping all the composition dependent terms

$$\tilde{D}(X) = D_0 X\,(1-X)\left(-\frac{z\mathcal{F}}{RT}\frac{\partial V(X)}{\partial X}+\hat{\theta}\right) \tag{B.33}$$

This expression is general, and may be safely applied to any single phase intercalation material to link the observed composition-dependent open circuit voltage and the shape of the composition-dependent chemical diffusivity. It is important to note that this expression is symmetric with respect to $X \to 0$ and $X \to 1$, both with respect to the non-ideal solution term and the chemomechanical coupling factor.

Using this composition-dependent chemical diffusivity, the diffusion equation may now be written as

$$\frac{\partial X}{\partial t} = \nabla \cdot \left(\tilde{D}(X)\nabla X\right) \tag{B.34}$$

which simplifies in spherical coordinates to

$$\frac{\partial X}{\partial t} = \frac{1}{r^2}\frac{\partial}{\partial r}\left(r^2 \tilde{D}(X)\frac{\partial X}{\partial r}\right) \tag{B.35}$$

Expression for the Open Circuit Voltage of $\mathrm{Li}_X\mathrm{Mn}_2\mathrm{O}_4$ as a function of the lithium composition X as fit by Doyle, *et al.* [92]. Evaluation of this expression for $0.2 \leq X \leq 0.995$ returns the open circuit voltage in units of Volts relative to a $\mathrm{Li}^+/\mathrm{Li}$ reference electrode.

$$\begin{aligned}V(X) = 4.19829 &+ 0.0565661\ \tanh\left(-14.5546\ X + 8.60942\right) \\ &- 0.0275479\ \left[(0.998432 - X)^{-0.492465} - 1.90111\right] \\ &- 0.157123\ \exp\left(-0.04738\ X^8\right) \\ &+ 0.810239\ \exp\left(-40\ X + 5.355\right)\end{aligned} \tag{B.36}$$

And the derivative with respect to composition

$$\frac{\partial V(X)}{\partial X} = -0.823297\ \mathrm{sech}(8.60942 - 14.5546X)^2 - 0.0135664\ (0.998432 - X)^{-1.49247} + 0.0595559\ X^7\ \exp\left(-0.04738\ X^8\right) - 32.4096\ \exp\left(-40\ X + 5.355\right) \quad \text{(B.37)}$$

B.2.1 Applicability of the Model to Other Systems

The framework is general enough to be applicable to other materials systems. Figure B-1 compares the predicted composition-dependent chemical diffusivity to experimental measurements [180] in Li_XCoO_2. The predicted values are off at $X \sim 0.5$ because the model for the open-circuit voltage [181] does not accurately capture the 'knee' at around 4.15 V that corresponds to the second-order order-disorder phase transformation.

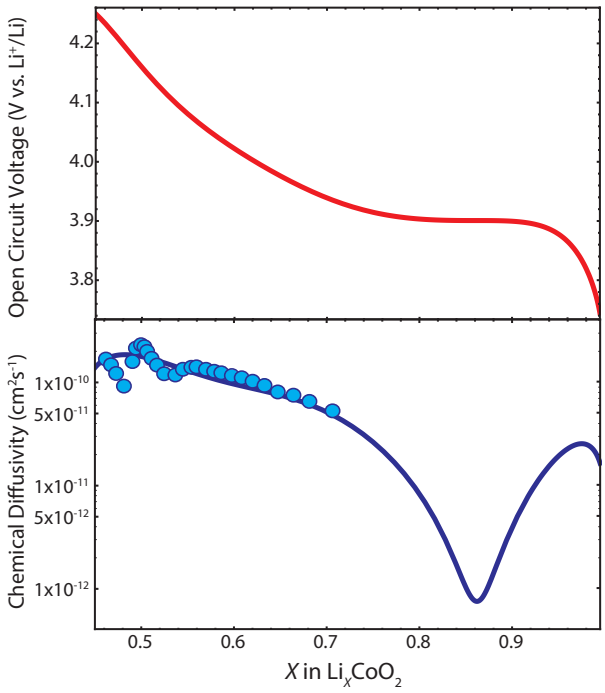

Figure B-1: (a) Open circuit potential of $\mathrm{Li}_X\mathrm{CoO}_2$ as given in Ref. [181]. (b) Blue solid curve is the thermodynamically-consistent chemical diffusivity of $\mathrm{Li}_X\mathrm{CoO}_2$ with $D_0 = 10^{-11}$ cm^2/s and $\hat{\theta} = 0.61$ plotted according to Equation B.33. Experimental data from Ref. [180] shown as points.